

UNSTEADY AERODYNAMICS OF FALLING PLATES

A Dissertation

Presented to the Faculty of the Graduate School

of Cornell University

in Partial Fulfillment of the Requirements for the Degree of

Doctor of Philosophy

by

Umberto Pesavento

January 2006

This document is in the public domain.

UNSTEADY AERODYNAMICS OF FALLING PLATES

Umberto Pesavento, Ph.D.

Cornell University 2006

We investigate the problem of falling paper by solving the two dimensional Navier-Stokes equations subject to the motion of a free falling body at Reynolds numbers around 10^3 , which is typical for a leaf or business card falling in air, and experimentally, by using a quasi two dimensional set up and high speed digital video at sufficient resolution to determine the instantaneous accelerations and thus deduce the fluid forces. We compare the measurements with the direct numerical solutions of the two-dimensional Navier-Stokes equation and, using inviscid theory as a guide, we decompose the fluid forces into contributions due to acceleration, translation, and rotation of the plate. The aerodynamic lift on a tumbling plate is found to be dominated by the product of linear and angular velocities rather than velocity squared as appropriate for an airfoil. This coupling between translation and rotation provides a mechanism for a brief elevation of center of mass near the cusp-like turning points. The Navier-Stokes solutions further provides the missing quantity in the classical theory of lift: the instantaneous circulation, and suggests a revised ODE model for the fluid forces. Experimentally and numerically, we get access to different dynamics by exploring the phase diagram spanned by the Reynolds number, the dimensionless moment of inertia, and the thickness to width ratio. In agreement with previous experiments, we find fluttering (side to side oscillations), tumbling (end over end rotation), and apparently chaotic motion. We explore further the transition region between fluttering and tumbling using both direct numerical solutions and the ODE model. In particular, by increasing the

non-dimensional moment of inertia in the direct numerical simulations, we observe a wide transition region in which the cards flutter periodically but tumble once between consecutive turning points. In this region, we also observe a divergence of the period of oscillation, with the cards falling vertically for distances of up to 50 times the card width. We analyze the transition between fluttering and tumbling in the ODE model and find a heteroclinic bifurcation which leads to a logarithmic divergence of the period of oscillation at the bifurcation point.

BIOGRAPHICAL SKETCH

Umberto Pesavento was born in Padova, Italy, in 1978. After receiving his bachelor degree in Physics from Princeton University in the August of 2000, he moved to Cornell University where he was a graduate student in the Physics Department until August of 2005.

To my parents

ACKNOWLEDGEMENTS

I am debited to my adviser Prof. Z. Jane Wang for her guidance and support during my doctorate. I would like to thank Anders Andersen with whom I collaborated for most of the work described in this thesis. I would like to thanks Steve Keast for his technical assistance in the construction of the experiment. I also would like to acknowledge John Guckenheimer, Sovan Lal Das, Lakshminarayan Mahadevan and Richard Rand for suggestions on the analysis of the ODE equations. Finally, I would like to thank David Russel and Sheng Xu for many discussions and suggestions.

TABLE OF CONTENTS

1	Introduction	1
2	Numerical Method	7
2.1	Solution on a Cartesian grid	7
2.2	Conformal Mapping	9
2.3	Integration of forces and torques	10
2.3.1	Pressure force	12
2.3.2	Viscous Force	14
2.3.3	Pressure torque	14
2.3.4	Viscous torque	16
2.4	Force summary	17
3	Experimental Method	20
4	Trajectories and flows	24
4.1	Non-dimensional parameters and phase diagram	24
4.2	Trajectories	25
4.2.1	Fluttering	28
4.2.2	Tumbling	30
4.2.3	Apparently chaotic motion	30
4.3	Comparison between experiment and direct numerical simulations .	34
4.4	Sensitivity to initial conditions	37
4.5	Vortex shedding and wake structure	40
4.5.1	Tumbling	40
4.5.2	Fluttering	41
4.6	The Strouhal number for a freely falling plate	41
5	Fluid forces: measurements and quasi-steady model	45
5.1	Experiment and direct numerical simulations	45
5.2	Quasi-steady force model	47
5.2.1	Circulation and Lift	51
5.2.2	Drag and dissipative torque	52
5.3	Circulation and Center of Mass Elevation	53
5.4	Measured and quasi-steady fluid forces	56
5.5	Measured and quasi-steady fluid torque	59
5.6	Validity of the quasi-steady approximation	60
6	ODE Model Analysis and bifurcations	69
6.1	Solutions in transition range between fluttering and tumbling	71
6.2	Direct numerical solutions versus previous experiments	75
6.3	Phenomenological model of a falling card	76
6.4	Non-dimensional equations	76

6.5	Numerical solutions with small thickness to width ratio	78
6.5.1	Small thickness to width ratio	78
6.5.2	Numerical solutions of the ODE model	78
6.6	Fixed points and bifurcations	82
6.6.1	Transition between steady descent and oscillatory motion . .	82
6.6.2	Transition between fluttering and tumbling	84
7	Conclusions	90
	Bibliography	94

LIST OF TABLES

4.1	The thickness h , the non-dimensional parameters β , I^* , and Re , and the measured average horizontal velocity $\langle v_x \rangle$, vertical velocity $\langle v_y \rangle$, and angular velocity $\langle \omega \rangle$. The Reynolds number defined in equation (4.3) is obtained using $\langle v_y \rangle$ and the kinematic viscosity of water at 25° C, i.e., $\nu = 0.0089 \text{ cm}^2 \text{ s}^{-1}$. The averages for $\beta = 1/5$ are based on 10 trajectories with 8 periods each, the averages for $\beta = 1/8$ are based on 20 trajectories with 3 periods each, and the averages for $\beta = 1/14$ are based on 10 trajectories with 5 periods each. For the plates with $\beta = 1/6$ and $\beta = 1/14$ we report the averages of the absolute values of v_x and ω	27
4.2	Initial conditions for the plates in the direct numerical simulations. I – V: $\beta = 1/8$, $h = 0.081 \text{ cm}$, $\rho_f = 1.0 \text{ g cm}^{-3}$, $\rho_s = 2.7 \text{ g cm}^{-3}$, and $\nu = 0.0089 \text{ cm}^2 \text{ s}^{-1}$; VI – VII: $\beta = 1/4$, $h = 0.05 \text{ cm}$, $\rho_f = 1.0 \text{ g cm}^{-3}$, $\rho_s = 2.0 \text{ g cm}^{-3}$, and $\nu = 0.0089 \text{ cm}^2 \text{ s}^{-1}$	36
4.3	Average velocities $\langle v_x \rangle$ and $\langle v_y \rangle$, angular velocity $\langle \omega \rangle$, and angle of descent for the tumbling plate with $\beta = 1/8$ in the experiment (rectangular cross-section) and in the direct numerical simulations (elliptical cross-section) with initial conditions (I – V) in table 4.2.	37
5.1	Lift and drag coefficients in the quasi-steady model.	58

LIST OF FIGURES

1.1	Rise of a falling journal cover under windless conditions, selected frames from a footage filmed at 300 fps.	4
2.1	(a) the grid around an ellipse of $\beta = 1/8$ obtained by the analytic conformal of equation (2.13). (b) conformal grid around a rectangle with the same width to thickness ratio obtained numerically	11
2.2	Trajectory of a tumbling ellipse with $\beta = 1/8$ and $\text{Re} = 10^3$ computed with resolution 512×1024 (solid line) and 256×512 (dashed line). The details of the solution differ but the qualitative features are the same. .	19
3.1	The experimental apparatus. (a) the transparent glass container, the release mechanism, the falling plate, and the high speed digital video camera shown schematically. (b) the release mechanism mounted on top of the container. The aluminum plate (1) is held at its midpoint by the clamp (2) below the water surface and it is aligned horizontally using the two bars (3). The plate is released when the clamp is opened using the small electromagnet (4). . . .	21
3.2	(a) A frame from the high speed video of the tumbling trajectory shown in figure 4.1. (b) The same frame converted to the black and white image used to determine the center of mass and orientation of the plate.	22
3.3	Horizontal and vertical components of the velocity v_x and v_y and angular velocity ω of the plate shown in figure 4.1 (c). The solid lines show velocities obtained by filtering the noise with a Fourier filter. The dots show velocities obtained with a single stencil derivative of the center of mass position.	23
4.1	Measured plate trajectories. (a) the fluttering plate with $h = 0.081$ cm and $\beta = 1/14$, (b) two apparently chaotic trajectories for the $h = 0.162$ cm and $\beta = 1/6$ plate, and (c) the tumbling plate with $h = 0.162$ cm and $\beta = 1/5$. For clarity the two trajectories in (b) are displaced from each other 0.5 cm horizontally and 1.5 cm vertically. The thick line segments show the plate cross-sections with time-intervals of 0.04 s in (a) and 0.025 s in (b) and (c).	26
4.2	The measured velocities (solid lines) for fluttering with $h = 0.081$ cm and $\beta = 1/14$, and the best fits (dotted lines) of the velocity expressions derived from equations (4.5) and (4.6). (a) the horizontal velocity component v_x , (b) the vertical velocity component v_y , and (c) the angular velocity ω . Both v_x and v_y are well-described by a single harmonics, whereas 3 harmonics are needed to capture the main features of ω with three local extrema for each half-period. .	29

4.3	The simple analytical curve (4.5) and (4.6) describes the fluttering trajectory for the plate with $\beta = 1/14$ shown in figure 4.1(a). The curve parameters are obtained by fitting the translational velocity components as shown by the two dotted lines in figure 4.2.	31
4.4	Measured velocities as functions of time for the tumbling plate with $h = 0.162$ cm and $\beta = 1/5$. (a) the horizontal velocity component, (b) the vertical velocity component, and (c) the angular velocity. The plate elevates (v_y is positive) after the long gliding segments whereas it does not elevate after the short gliding segments. The local maxima for v_y and ω almost coincide, and we note that v_x is large and ω is small during the long gliding segments.	32
4.5	Measured velocities as functions of time for the plate with $h = 0.162$ cm and $\beta = 1/6$ displaying irregular motion, see trajectory (1) in figure 4.1(b). (a) the horizontal velocity component, (b) the vertical velocity component, and (c) the angular velocity. The irregular motion involves long gliding segments at low angle of attack with descent velocities up to $v_y = -50$ cm s ⁻¹ followed by center of mass elevation with upward velocities up to $v_y = 20$ cm s ⁻¹	35
4.6	Tumbling dynamics with $\beta = 1/8$ from the experiment (blue) and the direct numerical simulation (red) with initial condition I in table 4.2. (a) trajectories and (b) v_x versus v_y . The trajectories are qualitatively similar, and we ascribe the quantitative differences to the difference in geometry between the rectangular and the elliptical cross-section.	38
4.7	Dependence on initial conditions of periodic solutions. (a) trajectory and (b) v_x versus v_y for a tumbling plate with $\beta = 1/8$, $Re = 1025$, and $I^* = 0.17$ with initial condition I (blue) and II (red) from table 4.2; (c) trajectory and (d) v_x versus v_y for a tumbling plate with $\beta = 1/4$, $Re = 10^2$, and $I^* = 0.36$ with initial condition VI (blue) and VII (red) from table 4.2.	39
4.8	The vorticity around the tumbling plate with $\beta = 1/8$, $I^* = 0.17$, and $Re = 1025$. The grid resolution was 512×1024 . Positive vorticity in red and negative vorticity in blue. (a) onset of the wake instability; (b) the instability is fully developed, and the plate has initiated its first turn; (c)–(d) a vortex pair is formed as the plate completes its turn; (e) the plate glides for a short distance; (f)–(h) the plate makes a second 180° turn; and (i) the plate resumes gliding.	42

4.9	The vorticity around the fluttering plate with $\beta = 1/18$, $I^* = 0.057$, and $\text{Re} = 412$. The grid resolution was 512×1024 . Positive vorticity in red and negative vorticity in blue. (a) the plate glides at small angle of attack; (b) the plate pitches up and its center of mass elevates; (c) the plate slows down; (d)–(f) the plate rotates and starts to shed its old leading edge vortex (red); (g)–(h) the old trailing edge vortex (blue) is shed; (i) the plate resumes gliding. . .	43
4.10	Vorticity fields with positive vorticity in red and negative vorticity in blue. The grid resolution was 512×1024 , and the time between consecutive fields was 0.0193 s. (a)–(f) tumbling plate with $\beta = 1/2$, $I^* = 0.84$, and $\text{Re} = 832$; (g)–(i) plate with $\beta = 1/2$ translating with velocity equal to the average translational velocity of the tumbling plate. In (a)–(f) a vortex pair is shed during every 180° rotation and in (g)–(i) a von Kármán vortex street is formed.	44
5.1	The fluid force components and the fluid torque as functions of the angle θ for the tumbling plates with $\beta = 1/8$. (a) – (c) experiment and (d) – (f) direct numerical simulation with initial condition I. In both cases we use units where $m' = (\rho_s - \rho_f) h l$. The measured and the computed force and torque are qualitatively similar and we ascribe the quantitative differences between measurements and computations to the differences in geometry.	46
5.2	The computed lift and fluid torque on steadily translating plates with $\beta = 1/8$ and fixed angle of attack, α , as functions of the distance traveled. The plates were impulsively started and the Reynolds numbers based on the width and the translational speed were 10^3 . (a) – (b) low angle of attack $\alpha = 10^\circ$ and (c) – (d) high angle of attack $\alpha = 40^\circ$. The torques are one to two orders of magnitude larger than the torques on the freely falling plates in figure 5.1.	48
5.3	The velocity components $v_{x'}$ and $v_{y'}$ in the laboratory reference frame are defined with respect to the coordinate system following the rotation of the body, whereas v_x and v_y are the horizontal and the vertical velocity component in the laboratory reference frame, respectively. The angle of attack, α , satisfies $\alpha \in [-\pi/2, \pi/2]$ and it is negative in the example sketched.	49

5.4	Navier-Stokes solution of a tumbling ellipse at $Re = 1100$, $I^* = 0.17$ and $e = 0.125$. (a) Body-fixed coordinate system and kinematic variables. (b) Trajectory and orientation of the chord (major axis of the ellipse) over five periods of motion. (c) the history of the chord (in red) and the force vector (in black), equally spaced in time for the first period of the trajectory in (b). The chords numbered from 1 to 4 correspond to the frames shown in (d) and to the times marked with dots on the force history of Fig. 5.5. (d) Vorticity field at four instants during a full rotation. The frames display an area of 5×2.5 chords and they are $4 a/u_t$ time units apart. The vorticity field is color coded on a logarithmic scale.	61
5.5	The fluid force and torque on the tumbling ellipse shown in Fig. 5.4. Solid lines are computed forces, with total force in red and the pressure force in blue. The corresponding dashed lines are the best fits of the data based on the quasi-steady model of equations (5.1-5.3). The added mass tensor $m_{11} = 0.53m$ and $m_{12} = 3.1m$, $m_{22} = 1.5m$, $m_{21} = 0.56m$ and the circulation around the ellipse $\Gamma = 2.6a^2\Omega + 0.49a \mathbf{v} \sin(2\alpha)$ are obtained from the pressure force. These m_{ij} differ from those predicted by inviscid theory ($m_{11}^{inv} = m_{21}^{inv} = 0.0491m$ and $m_{22}^{inv} = m_{12}^{inv} = 3.14m$) The viscous corrections are modeled with the expansions $F_x^\nu = -\nu_{11}u - \nu_{12}u^2$, $F_y^\nu = -\nu_{21}v - \nu_{22}v^2$ and $\tau^\nu = \nu_{31}uv - \nu_{32}\Omega - \nu_{33}\Omega \Omega $, with $\nu_{11} = 0.18$, $\nu_{12} = 0.0075$, $\nu_{21} = 0.070$, $\nu_{22} = 0.054$, $\nu_{31} = -0.31$, $\nu_{32} = -0.05$, and $\nu_{33} = 0.16$	62
5.6	Circulation as a function of time for the falling ellipse of Fig. 5.4. In blue, the value of the circulation found integrating the vorticity field up to a radius of $3/2$ chords from the center of the ellipse. The dashed line corresponds to the circulation obtained from fitting the pressure forces, the red dashed line to the contribution of the rotational term of equation (5.5) alone. The peaks of negative circulation not captured by the fit correspond to the vortices shed by the ellipse at the turning points of its trajectory.	63
5.7	Trajectories obtained from ordinary differential equations (5.1-5.3) for different values of the translational and rotational lift coefficients c_L and c_R : a) $c_R = 2.6$, $c_L = 0.49$, from the fit of Fig. 5.5; b) $c_R = 0$, $c_L = 1.5$, as in classical translational lift. Center of mass elevation occurs in (a), but is absent in (b).	64
5.8	Measured fluid force (black), total quasi-steady force (green), translational lift (blue), and rotational lift (red). (a) tumbling plate with $\beta = 1/5$ and (b) fluttering plate with $\beta = 1/14$. In (a) the translational lift points down at (1) and (4) and up at (2), (3), and (5), and the quasi-steady model underestimates the fluid forces at (1) after the short gliding segments.	65

5.9	Lift and drag components of fluid forces. Measured forces (black), total quasi-steady forces (green), and quasi-steady forces without added mass (blue). (a) – (b) tumbling with $\beta = 1/5$, (c) – (d) apparently chaotic motion with $\beta = 1/6$, (e) – (f) tumbling with $\beta = 1/8$, and (g) – (h) fluttering with $\beta = 1/14$. Added mass effects give negligible contributions to the lift. The relative contributions to the drag are larger, but the resulting thrust peaks (negative drag) are not always observed experimentally as with $\beta = 1/8$. In (g) the sign of the lift defined in equation (5.12) depends on whether the plate moves left or right.	66
5.10	Measured (black), translational (blue), and rotational lift (red). (a) tumbling with $\beta = 1/5$ and (b) fluttering with $\beta = 1/14$. In (a) the average value of the translational lift is small and its functional form is markedly different from the measured lift, whereas the rotational lift captures the main features of the measurements. In (b) both the translational and the rotational lift have significant contributions to the total lift and the functional forms are similar.	67
5.11	Measured torque and quasi-steady torque contributions. Measured torque (black), the term $(m_{11} - m_{22}) v_{x'} v_{y'}$ from ideal fluid theory (magenta), the term $-I_a \ddot{\theta}$ related to the added moment of inertia (cyan), the torque from translational lift (blue), the dissipative torque (red), and the sum of the torque from translational lift and dissipative effects (green). (a) – (b) tumbling with $\beta = 1/5$, (c) – (d) apparently chaotic motion with $\beta = 1/6$, (e) – (f) tumbling with $\beta = 1/8$, and (g) – (h) fluttering with $\beta = 1/14$	68
6.1	Trajectories obtained from direct numerical simulations of the two-dimensional Navier-Stokes equation around freely falling plates in the transition range between fluttering and tumbling. (a) periodic fluttering with the non-dimensional period of oscillation $T = 8.1$, (b) fluttering close to the transition between fluttering and tumbling with $T = 17.3$, (c) mixture of fluttering and tumbling with $T = 34.1$ for $\beta = 1/11$ and $T = 43.4$ for $\beta = 1/12$, and (d) periodic tumbling with $T = 12.1$. The semi-major axes of the plates have unit length in the four plots, and the periods of oscillation are made non-dimensional as described in § 6.4.	72
6.2	Dependence on initial conditions of falling ellipses in the transition between fluttering and tumbling ($\beta = 1/12.75$). The initial conditions for the trajectories in black, blue and red are respectively $(\theta, v_x, v_y, \omega)$: $(0.2, 0, 0, 0)$, $(0.2, 6.76, 3.38, 0)$ and $(0.2, 0, 0, 0.68)$	73
6.3	Vorticity field around an ellipse in the transition region ($\beta = 1/12$).	74

6.4	Numerical solutions of the non-dimensional equations (6.10) – (6.12) showing the card trajectories. (a) periodic fluttering for $I^* = 1.1$, (b) period-one tumbling for $I^* = 1.4$, (c) period-two tumbling for $I^* = 1.45$, (d) periodic mixture of fluttering and tumbling for $I^* = 1.6$, (e) chaotic dynamics for $I^* = 2.2$, and (f) small amplitude broadside on fluttering for $I^* = 3.0$	80
6.5	Amplitude of oscillation for $I^* = 3$ as a function of $\mu_T - \mu$, where $\mu = \mu_1 = \mu_2$ and mu_T is the critical value of μ , obtained by solving the ODE system 5.1-5.3 numerically. The size of the oscillation grows continuously from zero, indicating that the Hopf bifurcation between steady descent and oscillatory motion is supercritical. . . .	81
6.6	(a) fixed points and descent velocities and (b) phase diagram in the I^* versus μ_1 plane with the inset showing a magnification of the transition region between periodic fluttering and periodic tumbling. Numerical solutions of equations (6.10) – (6.12) and stability boundary for the broadside on fixed point (solid curve). Periodic fluttering (circles), steady broadside on descent (plus signs), periodic broadside on fluttering (crosses), periodic tumbling (stars), periodic mixture of fluttering and tumbling (diamonds), and chaos (triangles).	85
6.7	Transition between fluttering and tumbling. The card flutters in the region of the phase space on the left of the line and tumbles in the region on the right.	87
6.8	The transition between fluttering and tumbling. (a) Numerical solutions of equations (6.10) – (6.12) below and above the bifurcation point $I_C^* \approx 1.2191$, (b) and (c) the phase space trajectory for $I^* = 1.2190$ projected onto the space spanned by $v_{y'}$, θ , and ω (with $\omega \equiv \dot{\theta}$), and (d) the logarithmic divergence of the period of oscillation, T , in the neighborhood of I_C^*	89

Chapter 1

Introduction

Leaves, tree seeds, and paper cards which flutter (oscillate from side to side) or tumble (rotate and drift sideways) are beautiful everyday examples of solid objects moving in a fluid. To predict their complex trajectories requires the knowledge of the instantaneous fluid forces. Although determining the forces on a moving geometry in a fluid is a classical problem, only few analytical results exist and they are in special limits such as Stokes flow and inviscid irrotational flow around a steadily translating airfoil. In these steady flows, the fluid forces on a given object depend purely on the kinematic variables, e.g., the translational velocity and the angle of attack in the case of a simple glider. In contrast, most objects moving in a fluid encounter unsteady flows for which it is not clear to what degree quasi-steady models based on inviscid theory apply.

We choose to study freely falling plates for three reasons. First, it is a natural towing tank experiment with gravity being the driving force. Because the plates fall freely, the net force is directly related to the plate acceleration, which can be determined by tracking the motion with high speed digital video. This gives us a method for quantifying simultaneously the instantaneous kinematics and the fluid forces, thus providing a ground to test models of fluid forces. In addition, it is straightforward to generate a wide range of complex motions by changing the properties of the plates such as the thickness to width ratio of the plate cross-section. Second, the unconstrained dynamics of freely falling plates driven by gravity is interesting in its own right, and it is analogous to problems such as seed dispersal by wind [25, 5] and air bubbles rising freely in a liquid [21]. Improved force

models have important applications for these complex problems, e.g., to elucidate instability mechanisms and transitions related to change in bubble geometry and boundary conditions. Third, our study is in part motivated by our interest in flapping flight. There has been much recent progress in studies of the unsteady forces on flapping wings with wing kinematics similar to those of flying insects in flapping flight [40, 12, 8, 29, 38]. From this perspective, studies of freely falling plates give us access to a different family of periodic solutions, where the external driving force is prescribed instead of the wing kinematics.

Studies of freely falling plates have a long history starting with [24] who described tumbling qualitatively before the development of classical aerodynamics. However, most experiments have focused on qualitative and average properties and not on deducing the instantaneous fluid forces [10, 41, 33, 13, 7, 23]. Dupleich measured the angle of descent and the average tumbling frequency as functions of wing loading and ratio between plate length and width [10]. Willmarth, Hawk & Harvey measured a phase diagram for falling disks with steady descent, fluttering, and tumbling, and in the limit of small thickness to width ratio, they found that the final state depends only on the Reynolds number and the dimensionless moment of inertia [41]. Smith measured a phase diagram for falling plates qualitatively similar to the one for falling disks [33], Field, Klaus, Moore & Nori made further experiments on freely falling disks with apparently chaotic motion [13], Belmonte, Eisenberg & Moses quantified the transition from fluttering to tumbling in a quasi two-dimensional experiment [7], and Mahadevan, Ryu & Samuel observed a scaling law for the dependence of the rotational speed on the width of a tumbling card [23]. Jones & Shelley proposed a falling card model based on inviscid theory and the unsteady Kutta condition, but the method has so far not been implemented

numerically to model periodic fluttering and tumbling [17].

Tumbling has also been studied in the context of free and fixed axis auto-rotation as reviewed by [19]. Wind-tunnel experiments on fixed axis auto-rotation of plates [33, 31] and polygonal objects [32] were carried out at Reynolds numbers in the range $10^4 - 10^5$. Fixed axis auto-rotation and tumbling of a freely falling plate have some similarities, but there are significant differences between the two phenomena. The most important difference is that fixed axis auto-rotation involves only the rotational degree of freedom of the plate, and thus the coupling between translation and rotation is absent. Therefore it is not clear a priori how results on the two different types of auto-rotation are related.

What appears to be lacking is a model of the fluid force and torque that is constructed and tested against experiments or computations. The force predicted by inviscid theory includes added mass and a lift proportional to the product of velocity and circulation[18]. An unresolved issue is the choice of the circulation around the falling object, which cannot be determined from inviscid theory. Previous models either assumed the circulation to be a constant [22] or to be linearly proportional to the translational velocity[3, 34, 7]. The latter is appropriate for a steady translating airfoil at small angle of attack, as given by the celebrated Kutta-Joukowski condition which requires flow velocity to be finite at the singular trailing edge[6]. The resulting lift is quadratic in velocity. While the Kutta-Joukowski condition works remarkably well in this special case, there is no direct evidence that it holds for an object fluttering or tumbling in a fluid.

Theoretical progress is in part hindered by the lack of simultaneous measurements of instantaneous forces and flows around a falling object. Here we solve the Navier-Stokes equations for the fluid subject to the dynamics of a falling body

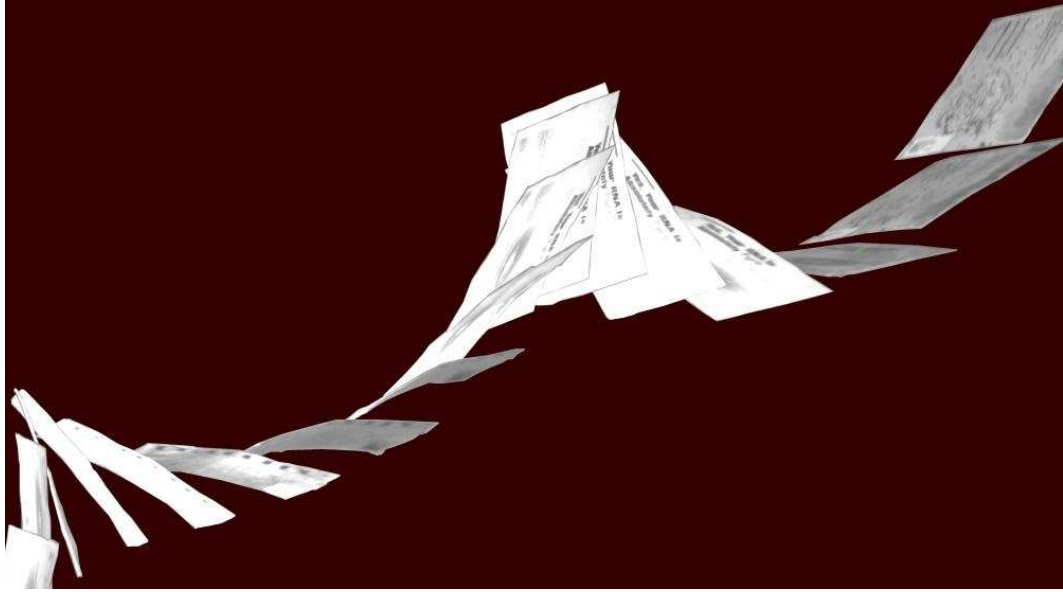


Figure 1.1: Rise of a falling journal cover under windless conditions, selected frames from a footage filmed at 300 fps.

in two dimensions. Solving the falling paper problem in the most general case, i.e., free fall of a three dimensional flexible sheet, is daunting and unrealistic at Reynolds numbers of the order of 10^3 . To simplify the problem, we note that bodies of relatively large span-to-chord ratios fall essentially along a two dimensional plane[19]. In the case of a business card, the span-to-chord ratio is about 1.8, and the chord remains in a vertical plane as it falls, i.e., the motion in the span-wise direction is negligible. Taking advantage of these observations we focus on a falling rigid plate in a two dimensional fluid governed by the incompressible Navier-Stokes equations. The choice of a rigid plate is convenient for numerics and for comparison against existing theories. Obtaining accurate numerical solutions in this regime turns out to be non-trivial due to the thin tip of the geometry, the moving boundary coupled to the fluid forces, and the small fluid torque. Our numerical method is based on a vorticity-stream function formulation in a conformal

grid fitted to the plate [37, 39]. The conformal grid concentrates points at the edges of the plate and can be mapped onto a Cartesian grid in which we discretize and solve the Navier-Stokes equations efficiently via FFT [11].

In addition, we investigate the aerodynamics of freely falling plates experimentally at Reynolds number of 10^3 in quasi two-dimensional setup. Chapter 4 describes the motion of freely falling rigid plates based on detailed measurement of the plate trajectories and from this to learn about the instantaneous fluid forces. We record the trajectories using high speed digital video, which gives us sufficient temporal and spatial resolution to obtain instantaneous translational and rotational velocities and to extract the instantaneous fluid forces and torques on the plates. The experiment is essentially two-dimensional, and it allows us to compare the measurements with direct numerical simulations of the Navier-Stokes equation for a rigid body falling in a two-dimensional flow. In this way we supplement the experiment with numerical flow visualizations. We describe the computed wake structure and compare the measured and the computed fluid forces.

The measured and the computed forces allow for a direct test of the force models proposed in the literature [34, 22, 7, 27]. Our force model is based on Kirchhoff's equations governing the motion of a solid in an inviscid fluid [18]. By comparing the model predictions with the measured forces, we find that the fluid circulation is dominated by a rotational term proportional to the angular velocity of the plate, rather than to the translational velocity as appropriate for a glider with fixed angle of attack. We use the ODE model to analyze the transition between fluttering and tumbling and show that the transition is a heteroclinic bifurcation which leads to a logarithmic divergence of the period of oscillation at the bifurcation point.

The work described in this thesis has been published in [27], where the numeri-

cal simulations and the ODE model were developed, in [1], where the experimental studies and their comparison with the numerical results have been performed, and in [2] where the transition between fluttering and tumbling was analyzed.

Chapter 2

Numerical Method

In order to compute the trajectory and the flow around a free falling body in two dimensions one has to solve Navier-Stokes equations for an incompressible fluid.

$$\frac{\partial \mathbf{u}}{\partial t} + \mathbf{u} \cdot \nabla \mathbf{u} = -\frac{\nabla P}{\rho} + \nu \nabla^2 \mathbf{u} \quad (2.1)$$

$$\nabla^2 \mathbf{u} = 0 \quad (2.2)$$

where \mathbf{u} is the fluid velocity, P is the pressure, ρ the density of the fluid and t is time.

In the two dimensions, it is computationally efficient to rewrite the Navier-Stokes equations as a function of the stream function ψ and of the vorticity ω , defined such that $\mathbf{u} = (u, v) = (-\partial\psi/\partial y, \partial\psi/\partial x)$ and $\omega = -\partial u/\partial y + \partial v/\partial x$. This change of variables eliminates the pressure from the governing equations and reduces the number of fields to be considered from P, u and v to just ψ and ω . The Navier-Stokes equations in the vorticity stream function formulation are [6]

$$\frac{\partial \omega}{\partial t} + (\mathbf{u} \cdot \nabla) \omega = \nu \nabla^2 \omega \quad (2.3)$$

$$\nabla^2 \psi = \omega \quad (2.4)$$

2.1 Solution on a Cartesian grid

The motion of a body falling freely in an incompressible fluid is governed by a coupled system of the Navier-Stokes equations and Newton equation. In the case of a symmetric free-falling plate the fluid force acts near the center of mass (see chapter 5), and the resulting torque relative to the center of mass is small. The accuracy of the solution of the coupled system is therefore determined by the

error in the pressure torque. To obtain sufficient accuracy we use a 4th order finite difference scheme introduced by [11] and a body fitted computational grid generated by a conformal mapping. To avoid singularities at the corners of the two-dimensional plates we use an elliptical cross-section and the method applied by [37] for the two-dimensional flow around a flapping wing with prescribed kinematics.

The first step in this procedure is to solve equations 2.3 and 2.4 on a Cartesian grid. Here we used the method described in [11] where equations 2.1 and 2.2 are discretized respectively as

$$\begin{aligned} \left(1 + \frac{h^2}{12} \nabla_h^2\right) \frac{\partial \omega}{\partial t} &= \nu \left(\nabla_h^2 + \frac{h^2}{6} D_x^2 D_y^2 \right) \omega - \left(1 + \frac{h^2}{6} D_x^2 D_y^2\right) \omega \\ &\quad - \left(1 + \frac{h^2}{12} \nabla_h^2\right) \left(\frac{\partial u \omega}{\partial x} + \frac{\partial v \omega}{\partial y} \right) \end{aligned} \quad (2.5)$$

$$\left(\nabla_h^2 + \frac{\partial h^2}{\partial 6} D_x^2 D_y^2 \right) \psi = \left(1 + \frac{h^2}{12} \nabla_h^2\right) \omega \quad (2.6)$$

where ∇_h^2 is the 5-point discrete Laplacian and D_x^2 and D_y^2 are the 3 point discrete second derivatives on a grid of spacing h .

$$(D_x^2 f)(x, y) = \frac{f(x+h, y) - 2f(x, y) + f(x-h, y)}{h^2} \quad (2.7)$$

$$(D_y^2 f)(x, y) = \frac{f(x, y+h) - 2f(x, y) + f(x, y-h)}{h^2} \quad (2.8)$$

$$(\nabla_h^2 f)(x, y) = \frac{f(x+h, y) + f(x-h, y) + f(x, y+h) + f(x, y-h) - 4f(x, y)}{h^2} \quad (2.9)$$

On a Cartesian grid equations 2.5 and 2.6 can be solved successively by FFT. The boundary condition on ψ and ω are given by the no-slip and no penetration conditions at the boundaries of the body. In particular, the no slip condition $\partial \psi / \partial \mathbf{n} = 0$ is converted into a boundary condition on ω by using Briley's formula

$$\omega_{0,j} = \frac{108\psi_{1,j} - 27\psi_{2,j} + 4\psi_{3,j}}{18h^2} - \frac{3}{11} \left(\frac{\partial \psi}{\partial x} \right) \quad (2.10)$$

where the boundary is at $(1, j)$ and the points at $(0, j)$ are an extension of the computational domain, known as ghost points, used in order to implement the boundary

condition on the vorticity for the Poisson solver. At infinity, the boundary conditions are prescribed by using the stream function ψ for the inviscid solution of the flow around an ellipse [6] and by using $\omega = -2\Omega$ for the vorticity, where Ω is the angular velocity of the body. With the boundary conditions described above, the calculation sequence of the method is the following:

1. calculate ψ^{n+1} by solving equation 2.6 by FFT;
2. calculate \mathbf{u}^{n+1} from ψ^{n+1} ;
3. calculate ω^{n+1} from ω^n by using equation 2.5.

The procedure described above is explicit and is integrated forward in time using a 4th order Runge-Kutta scheme.

2.2 Conformal Mapping

The numerical method described above solves Navier-Stokes equations for an incompressible fluid in a rectangular domain where arbitrary velocity profiles or periodic conditions can be imposed at the boundaries. In order to compute the flow around a fixed object it is necessary to establish a conformal mapping from the exterior of the object to such a rectangular domain. Navier-Stokes equations are invariant under conformal mapping up to a scaling factor, so that one can equivalently solve the following equations on the Cartesian grid discussed in the previous section. In body-fixed elliptical coordinates (μ, ϕ) we have

$$\frac{\partial (S\omega)}{\partial t} + (\sqrt{S} \mathbf{u} \cdot \nabla) \omega = \nu \nabla^2 \omega , \quad (2.11)$$

$$\nabla \cdot (\sqrt{S} \mathbf{u}) = 0 , \quad (2.12)$$

where \mathbf{u} is the velocity field, ω the vorticity field, and ν the kinematic viscosity of the fluid. In the case of the computations presented here, the conformal mapping from the exterior of the ellipse with major axis $l = 2c \cosh \mu_0$ to a semi-infinite strip, where $\mu = \mu_0$ at the boundary of the ellipse is given by

$$x + iy = c \cosh(\mu + i\phi) \quad (2.13)$$

and the scaling factor associated with the map is

$$S(\mu, \phi) = c^2 (\cosh^2 \mu - \cos^2 \phi) \quad (2.14)$$

The mapping concentrates grid points at the edges of the plate (see figure 2.1) and casts Navier-Stokes equation onto a Cartesian grid, allowing for an efficient solver. We use body-fixed coordinates to eliminate spatial interpolation as the plate moves with respect to the fluid. This turns out to be crucial for obtaining long free fall trajectories. Although the absence of sharp corners makes ellipses good choices of geometry for studying free-falling bodies the method described above can be generalized to any shape. For example a conformal grid around any closed polygon can be generated numerically using standard packages [35]. An example of such grid is shown in Fig. 2.1.

2.3 Integration of forces and torques

In the following we derive the force and torque on an ellipse moving in a fluid. In the numerical computations presented here, these quantities are evaluated in the reference frame moving with the falling object. The Navier-Stokes equations for the fluid around the ellipse in the non inertial frame co-moving with the ellipse with velocity \mathbf{u} acceleration \mathbf{a} , angular velocity $\mathbf{\Omega}$ and angular acceleration $\dot{\mathbf{\Omega}}$ are

$$\frac{\partial \mathbf{u}}{\partial t} + \mathbf{u} \cdot \nabla \mathbf{u} = -\frac{\nabla P}{\rho} + \nu \nabla^2 \mathbf{u} - \mathbf{\Omega} \times (\mathbf{\Omega} \times \mathbf{r}) - 2\mathbf{\Omega} \times \mathbf{u} - \dot{\mathbf{\Omega}} \times \mathbf{r} - \dot{\mathbf{a}} \quad (2.15)$$

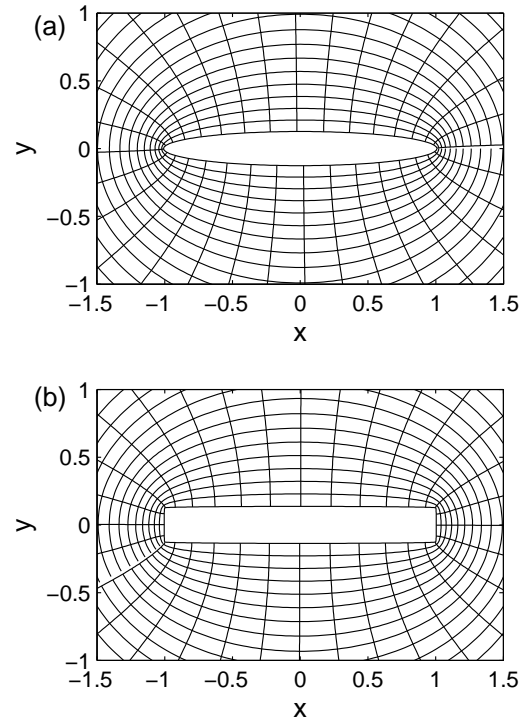


Figure 2.1: (a) the grid around an ellipse of $\beta = 1/8$ obtained by the analytic conformal of equation (2.13). (b) conformal grid around a rectangle with the same width to thickness ratio obtained numerically

The pressure and viscous force and torque on a stationary plate can be calculated by integrating the stress tensor along the surface [20]. We parametrize the boundary of the ellipse as

$$\mathbf{r} = (x, y) = a(\cosh \mu_0 \cos \theta, \sinh \mu_0 \sin \theta) \quad (2.16)$$

the tangent and the normal vector can then be expressed by derivatives of \mathbf{r} with respect to the arc length s along the boundary of the ellipse

$$\hat{\mathbf{t}} = \frac{\partial \mathbf{r} / \partial s}{|\partial \mathbf{r} / \partial s|} = \frac{(-\cosh \mu_0 \sin \theta, \sinh \mu_0 \cos \theta)}{\sqrt{\cosh^2 \mu_0 - \cos^2 \theta}} \quad (2.17)$$

$$\hat{\mathbf{n}} = \frac{\partial^2 \mathbf{r} / \partial s^2}{|\partial^2 \mathbf{r} / \partial s^2|} = \frac{(-\sinh \mu_0 \cos \theta, -\cosh \mu_0 \sin \theta)}{\sqrt{\cosh^2 \mu_0 - \cos^2 \theta}} \quad (2.18)$$

Since

$$\frac{\partial \mathbf{r}}{\partial s} = \frac{1}{\sqrt{S}} \frac{\partial \mathbf{r}}{\partial \theta} \quad (2.19)$$

where the scaling factor is defined as equation (2.14) for an ellipse, we can rewrite $\hat{\mathbf{n}}$ as a function of $\mathbf{r} = (x, y)$ as

$$\hat{\mathbf{n}} = \left(\frac{\partial y}{\partial s}, \frac{-\partial x}{\partial s} \right) \quad (2.20)$$

2.3.1 Pressure force

The pressure force can be written as an integral of the pressure over the boundary Γ of the body

$$F_p = - \int_{\Gamma} P \hat{\mathbf{n}} ds = - \int_{\Gamma} P \left(-\frac{\partial y}{\partial s}, \frac{\partial x}{\partial s} \right) ds = - \int_{\Gamma} (-y, x) \frac{\partial P}{\partial s} ds \quad (2.21)$$

in other cases it is also convenient to formally express it as an integral over the area A of the interior of the body

$$\mathbf{F}_p = - \int_{\Gamma} P \hat{\mathbf{n}} ds = \int_A \nabla P dx dy \quad (2.22)$$

In the non-inertial frame co-moving with the ellipse the left hand side of equation (2.15) vanishes so that we can solve for the pressure gradient

$$\frac{\nabla P}{\rho} = \nu \nabla^2 \mathbf{u} - \boldsymbol{\Omega} \times (\boldsymbol{\Omega} \times \mathbf{r}) - 2\boldsymbol{\Omega} \times \mathbf{u} - \dot{\boldsymbol{\Omega}} \times \mathbf{r} - \mathbf{a} \quad (2.23)$$

In the following we evaluate the contributions of the terms in the right end side of equation (2.23) to the integral (2.22). The contributions of the term $\nu \nabla^2 \mathbf{u}$ in equation (2.23) corresponds to the pressure force and a stationary ellipse. The other four terms give the non-inertial contributions to the pressure force. The contribution of the first term is evaluated more conveniently integrating along the boundary according to equation (2.21), where its contribution to $\frac{\partial P}{\partial s}$ is evaluated by projecting $\nu \nabla^2 \mathbf{u}$ onto $\hat{\mathbf{s}}$.

$$\frac{\partial P^{(\nu \nabla^2 \mathbf{u})}}{\partial s} = -\hat{\mathbf{s}} \cdot \nu \nabla^2 \mathbf{u} = -\nu \hat{\mathbf{s}} \cdot \nabla \times \boldsymbol{\omega} = -\nu \hat{\mathbf{s}} \cdot \left(\hat{\mathbf{n}} \frac{\partial \omega}{\partial s} - \hat{\mathbf{s}} \frac{\partial \omega}{\partial n} \right) = \nu \frac{\partial \omega}{\partial n} \quad (2.24)$$

so that

$$\mathbf{F}_p^{(\nu \nabla^2 \mathbf{u})} = -\nu \int_{\Gamma} (-y, x) \frac{\partial \omega}{\partial n} ds \quad (2.25)$$

The contributions of the non-inertial terms can be conveniently evaluated by using equation (2.22) and integrating formally over the area of the body. The only non-inertial correction that contributes to the force is associated with the plate acceleration \mathbf{a}

$$\mathbf{F}_p^{(-\mathbf{a})} = - \int \int_A \rho (-\mathbf{a}) dx dy = \rho A \mathbf{a} \quad (2.26)$$

The contributions of $-\boldsymbol{\Omega} \times (\boldsymbol{\Omega} \times \mathbf{r})$ and $-\dot{\boldsymbol{\Omega}} \times \mathbf{r}$ vanish for a symmetric body

$$\begin{aligned} \mathbf{F}_p^{(-\boldsymbol{\Omega} \times (\boldsymbol{\Omega} \times \mathbf{r}))} &= -\rho \int \int_A -\boldsymbol{\Omega} \times (\boldsymbol{\Omega} \times \mathbf{r}) dx dy \\ &= \rho \int \int_A ((\boldsymbol{\Omega} \cdot \mathbf{r}) \boldsymbol{\Omega} - \boldsymbol{\Omega}^2 \mathbf{r}) dx dy = \rho \boldsymbol{\Omega}^2 \int \int_A \mathbf{r} dx dy = 0 \end{aligned} \quad (2.27)$$

$$\mathbf{F}_p^{-\dot{\boldsymbol{\Omega}} \times \mathbf{r}} dx dy = - \int \int_A \rho (-\dot{\boldsymbol{\Omega}} \times \mathbf{r}) = \rho \dot{\boldsymbol{\Omega}} \int \int_A \mathbf{r} dx dy = 0 \quad (2.28)$$

The contribution due to Coriolis force $\mathbf{F}_p^{-2\boldsymbol{\Omega} \times \mathbf{u}}$ also vanishes, since $\mathbf{u} = 0$ at the boundary. The total pressure force is then

$$\mathbf{F}_p = -\nu \int_{\Gamma} (-y, x) \frac{\partial \omega}{\partial n} ds + \rho A \mathbf{a} \quad (2.29)$$

2.3.2 Viscous Force

The viscous force is obtained by integrating the stress tensor $\sigma_{ij} = \nu(\frac{\partial u_i}{\partial x_j} + \frac{\partial u_j}{\partial x_i})$ along the boundary of the ellipse

$$F_i^\nu = \nu \int_{\Gamma} \sigma_{ij} \hat{n}_j ds = \nu \left(\frac{\partial u_i}{\partial x_j} + \frac{\partial u_j}{\partial x_i} \right) \hat{n}_j ds \quad (2.30)$$

$$= \nu \int_{\Gamma} \left(\frac{\partial u_i}{\partial x_j} - \frac{\partial u_j}{\partial x_i} \right) \hat{n}_j ds + 2\nu \int_{\Gamma} \frac{\partial u_j}{\partial x_i} \hat{n}_j ds \quad (2.31)$$

$$= \nu \int_{\Gamma} w \hat{s} ds + 2\nu \int_A (\nabla \cdot \mathbf{u}) dA = \nu \int_{\Gamma} w \hat{s} ds \quad (2.32)$$

2.3.3 Pressure torque

The pressure torque is also obtained by integrating along the boundary of the ellipse

$$\tau_p = \int_{\Gamma} P(\mathbf{r} \times (-\hat{\mathbf{n}})) ds \quad (2.33)$$

using equation (2.16) and equation (2.20) we rewrite $\mathbf{r} \times \hat{\mathbf{n}}$ as

$$-\mathbf{r} \times \hat{\mathbf{n}} = x \frac{\partial x}{\partial s} + y \frac{\partial y}{\partial s} = \frac{1}{2} \frac{\partial R^2(s)}{\partial s} \quad (2.34)$$

by using the identity above and integrating by parts we have

$$\tau_P = \int_{\Gamma} P((\hat{\mathbf{r}}) \times (-\hat{\mathbf{n}})) ds = \frac{1}{2} \int_{\Gamma} P \frac{\partial R^2(s)}{\partial s} ds = -\frac{1}{2} \int_{\Gamma} R^2(s) \frac{\partial P}{\partial s} ds \quad (2.35)$$

Again $\frac{\partial P}{\partial s}$ can be obtained projecting both sides of equation (2.23) onto $\hat{\mathbf{s}}$. The first term of the on the right hand side corresponds to the pressure torque on a

body at rest and by using equation (2.24) we have

$$\tau_p^{(\nu \nabla^2 \mathbf{u})} = -\frac{\nu}{2} \int_{\Gamma} R^2(s) \frac{d\omega}{dn} ds \quad (2.36)$$

this integral can be simplified further for an ellipse where the radius is given by

$$R^2 = (\cosh^2 \mu_0 \cos^2 \theta + \sinh^2 \mu_0 \sin^2 \theta) a^2 = ((\sinh^2 \mu_0 - \cosh^2 \mu_0) \sin^2 \theta + \cosh^2 \mu_0) a^2$$

so that

$$\tau_p^{(\nu \nabla^2 \mathbf{u})} = \frac{\nu a^2}{2} \int_{\Gamma} \frac{\partial \omega}{\partial \mu} \sin^2 \theta ds - \frac{\nu a^2}{2} \cosh^2 \mu_0 \int_{\Gamma} \frac{\partial \omega}{\partial \mu} ds = \frac{\nu a^2}{2} \int_{\Gamma} \frac{\partial \omega}{\partial \mu} \sin^2 \theta d\theta$$

where the integral $\int \frac{\partial \omega}{\partial \mu} ds$ vanishes by equation (2.24) since the pressure along the body is a one-valued function. Because of the sensitivity of the trajectories of free-falling bodies on the value of the aerodynamic torque, being able to calculate the second integral in the expression above analytically is crucial for the stability of the numerical scheme. This is not possible, for example, for a conformal mapping obtained numerically, as in the case of the rectangular shape shown in figure 2.1, where equation (2.36) has to be used instead.

As in the force calculation, the other terms on the right end side of equation 2.23 give the non inertial corrections to the pressure torque.

$$\begin{aligned} \tau_p^{(-\dot{\mathbf{\Omega}} \times \mathbf{r})} &= -\frac{\rho}{2} \int_{\Gamma} R^2(s) \left(-\hat{\mathbf{s}} \cdot (\dot{\mathbf{\Omega}} \times \mathbf{r}) \right) ds \\ &= \frac{\rho}{2} \int_{\Gamma} R^2(s) \dot{\mathbf{\Omega}} \cdot (\mathbf{r} \times \hat{\mathbf{s}}) ds = \frac{\rho \dot{\mathbf{\Omega}}}{2} \int_0^{2\pi} R^2(\theta) (a \cosh \mu_0 \cos \theta, a \sinh \mu_0 \sin \theta) \\ &\quad \times (-a \cosh \mu_0 \sin \theta / \sqrt{S}, a \sinh \mu_0 \cos \theta / \sqrt{S}) \sqrt{S} d\theta = 2I_f \dot{\mathbf{\Omega}} \end{aligned}$$

where I_f is the moment of inertial of the displaced fluid. All the remaining terms vanish for an ellipse.

$$\tau_p^{-\dot{\mathbf{a}}} = \frac{\rho}{2} \int_{\Gamma} R^2(s) (\hat{\mathbf{s}} \cdot \dot{\mathbf{a}}) = \frac{\dot{\mathbf{a}}}{2} \int_{\Gamma} R^2(s) \hat{\mathbf{s}} ds = 0 \quad (2.37)$$

$$\begin{aligned}
\tau_p^{-\mathbf{\Omega} \times (\mathbf{\Omega} \times \mathbf{r})} &= \frac{-\rho\Omega^2}{2} \int_{\Gamma} R^2(s) \hat{s} \left((\mathbf{\Omega} \cdot \mathbf{r}) \mathbf{\Omega} - \Omega^2 \mathbf{r} \right) ds = -\frac{\rho\Omega^2}{2} \int_{\Gamma} \hat{s} \cdot \mathbf{r} dr \\
&= -\frac{\rho\Omega^2}{2} \int_0^{2\pi} R^2(\theta) (\cosh \mu_0 \cos \theta, \sinh \mu_0 \sin \theta) \cdot \\
&\quad (-\cosh \mu_0 \sin \theta / \sqrt{S}, \sinh \mu_0 \cos \theta / \sqrt{S}) \sqrt{S} d\theta = 0
\end{aligned}$$

Again the Coriolis contribution vanishes, $\tau_p^{-2\mathbf{\Omega} \times \mathbf{u}} = 0$, since $\mathbf{u} = 0$ at the boundary.

Thus the pressure torque is given by

$$\tau_p = \frac{\nu a^2}{2} \int_0^{2\pi} \frac{\partial \omega}{\partial \mu} \sin^2 \theta d\theta + 2I_f \dot{\mathbf{\Omega}} \quad (2.38)$$

2.3.4 Viscous torque

The viscous torque is also obtained by integrating the stress tensor $\sigma_{ij} = \nu \left(\frac{\partial u_i}{\partial x_j} + \frac{\partial u_j}{\partial x_i} \right)$ along the boundary of the ellipse

$$\tau^\nu = \int_{\Gamma} \epsilon_{li} r_l \sigma_{ij} \hat{n}_j = \nu \int_{\Gamma} \epsilon_{li} r_l \left(\frac{\partial u_i}{\partial x_j} + \frac{\partial u_j}{\partial x_i} \right) \hat{n}_j ds \quad (2.39)$$

$$= \nu \int_{\Gamma} \epsilon_{li} r_l \left(\frac{\partial u_i}{\partial x_j} - \frac{\partial u_j}{\partial x_i} \right) \hat{n}_j + 2\nu \int_{\Gamma} \epsilon_{li} r_l \frac{\partial u_j}{\partial x_i} \hat{n}_j ds \quad (2.40)$$

$$= \nu \int_{\Gamma} \epsilon_{li} r_l \epsilon_{ij} \omega \hat{n}_j ds + 2\nu \int_{\Gamma} \epsilon_{li} r_l \frac{\partial u_j}{\partial x_i} \hat{n}_j ds \quad (2.41)$$

$$= -\nu \int_{\Gamma} r_j \omega \hat{n}_j ds + 2\nu \int_{\Gamma} \epsilon_{li} r_l \frac{\partial u_j}{\partial x_i} \hat{n}_j ds \quad (2.42)$$

where the identity $\epsilon_{li} \epsilon_{ij} = -\delta_{lj}$ has been used to contract the first integral above.

We evaluate the first term of equation (2.42) for an ellipse

$$-\nu \int_{\Gamma} r_j \omega \hat{n}_j ds = \quad (2.43)$$

$$= -\nu \int_{\Gamma} \omega \left(-x \frac{\partial dy}{\partial ds} + y \frac{\partial dx}{\partial ds} \right) ds = -\nu \int_0^{2\pi} \omega \left(-x \frac{\partial dy}{\partial d\theta} + y \frac{\partial dx}{\partial d\theta} \right) d\theta \quad (2.44)$$

$$= -\nu \int_0^{2\pi} \omega a^2 (-\cosh \mu_0 \sinh \mu_0 \cos \theta^2 - \cosh \mu_0 \sinh \mu_0 \sin^2 \theta) d\theta \quad (2.45)$$

$$= \nu a^2 \cosh \mu_0 \sinh \mu_0 \int_0^{2\pi} \omega d\theta \quad (2.46)$$

The second term vanishes

$$2\nu \int_{\Gamma} \epsilon_{li} r_l \partial_i u_j \hat{n}_j ds = 2\nu \int \int_A \partial_j (\epsilon_{li} r_l \partial_i u_j) dA \quad (2.47)$$

$$= 2\nu \int \int_A \epsilon_{li} (\partial_j r_l) (\partial_i u_j) dA + 2\nu \int \int_A \epsilon_{li} r_l \partial_i (\partial_j u_j) dA \quad (2.48)$$

$$= 2\nu \int \int_A \epsilon_{li} \delta_{jl} (\partial_i u_j) dA = 2\nu \int \int_A \epsilon_{ji} \partial_i u_j dA \quad (2.49)$$

$$= -2\nu \int \int_A \nabla \times \mathbf{u} dA = -2\nu \int_{\Gamma} \mathbf{u} \cdot d\mathbf{s} = 0 \quad (2.50)$$

So that the viscous torque is given by

$$\tau_{\nu} = \nu a^2 \cosh \mu_0 \sinh \mu_0 \int_0^{2\pi} \omega d\theta \quad (2.51)$$

2.4 Force summary

The contributions from the plate acceleration to the pressure force, \mathbf{F}_p , and the pressure torque, τ_p , are given by the \mathbf{a} and $\dot{\Omega}$ terms in equations (2.52) and (2.53). The viscous force, \mathbf{F}_{ν} , and torque, τ_{ν} , have the same form as for a stationary ellipse. The integral equations for the aerodynamic force and torque on an moving ellipse in a two-dimensional incompressible fluid as a function of its kinematic variable and the vorticity at its boundary are

$$\mathbf{F}_p = \nu \rho_f c \int_0^{2\pi} (\sinh \mu_0 \sin \theta, -\cosh \mu_0 \cos \theta) \frac{\partial \omega}{\partial \mu} d\theta + \frac{1}{4} \pi \rho_f l h \mathbf{a}, \quad (2.52)$$

$$\tau_p = \frac{1}{2} \nu \rho_f c^2 \int_0^{2\pi} \frac{\partial \omega}{\partial \mu} \sin^2 \theta d\theta + \frac{1}{32} \pi \rho_f l h (l^2 + h^2) \dot{\Omega}, \quad (2.53)$$

$$\mathbf{F}_{\nu} = \nu \rho_f c \int_0^{2\pi} \omega (-\cosh \mu_0 \sin \theta, \sinh \mu_0 \cos \theta) d\theta, \quad (2.54)$$

$$\tau_{\nu} = \nu \rho_f c^2 \cosh \mu_0 \sinh \mu_0 \int_0^{2\pi} \omega d\theta, \quad (2.55)$$

where ρ_f is the density of the fluid, h is the minor axis of the ellipse, and \mathbf{a} and $\dot{\Omega}$ are the translational and the angular acceleration of the plate, respectively. The

plate dynamics follows Newton's 2nd law, and the updated plate velocity is fed back to the Navier-Stokes solver through the boundary conditions. The terms depending on the accelerations \mathbf{a} and $\dot{\Omega}$ in equations 2.52 and 2.53 can be moved to the left end side of Newton's equation. However, in order to improve the numerical stability of the method, it is convenient to leave them on the right end side and use the accelerations calculated in the previous time step.

With this computational method it typically takes 10 to 20 times longer to resolve the free fall of a plate than to compute the flow past the same plate undergoing a similar but prescribed motion in which the feed back step is not needed. The simulations of freely falling plates discussed in the following are obtained using a 512×1024 grid and were repeated using a 256×512 grid to check the computational accuracy. The results presented here hold for both resolutions, although details in the trajectories might differ (see figure 2.2).

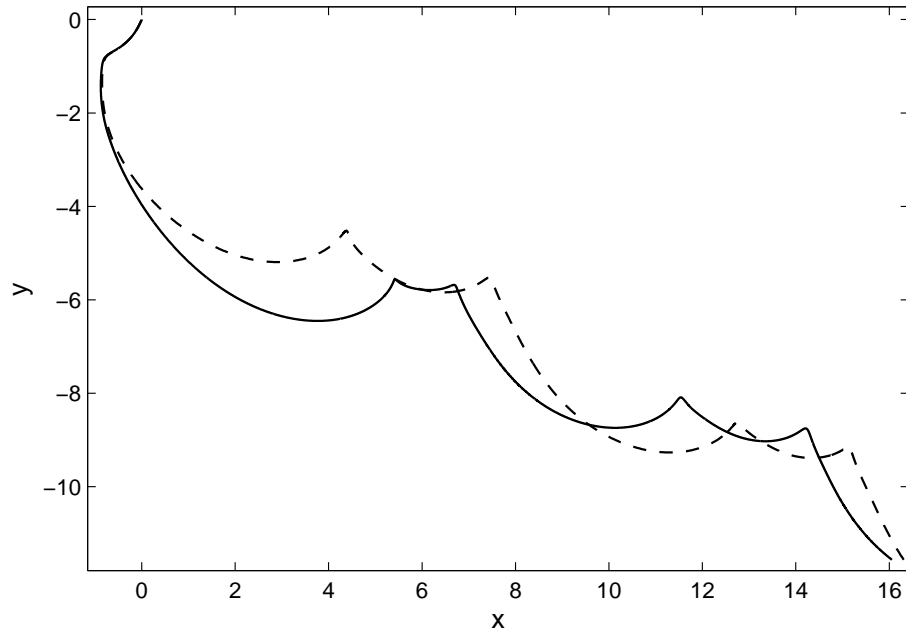


Figure 2.2: Trajectory of a tumbling ellipse with $\beta = 1/8$ and $\text{Re} = 10^3$ computed with resolution 512×1024 (solid line) and 256×512 (dashed line). The details of the solution differ but the qualitative features are the same.

Chapter 3

Experimental Method

We measure the trajectories of small aluminum plates which fall in a water tank in an essentially two-dimensional experiment. The experiment is conducted using a rectangular glass container which is 30 cm wide, 45 cm high, and 75 cm long, see figure 3.1(a). The container is filled with water, and a release mechanism on top of the container allows us to drop the plates below the water surface with well-controlled initial conditions. The release mechanism consists of a metal clamp which holds the plates at their midpoint and opens using a small electromagnet as shown in figure 3.1(b). The plates are 19 cm long and between 0.6 cm and 1.1 cm wide. The large length to width ratios between 15 and 30 make the influence of three-dimensional effects at the ends negligible.

We record the trajectories using high speed digital video at 400 to 500 frames per second. The frame-rate is sufficient to resolve both the translational and the rotational motion during all parts of the descent, including the turning points which are dominated by fast rotational motion. The camera is positioned on one side of the transparent glass container, see figure 3.1(a), and illuminate a white background homogeneously on the opposite side of the container. In each frame we observe the dark plate cross-section on the white background and identify the center and the orientation of the plate cross-section (see figure 3.2). The measured trajectories are smooth, and we are able to obtain instantaneous velocities using a finite difference scheme (see figure 3.3). However, we have to filter out high frequency noise using the Fourier transform to obtain instantaneous accelerations. In the following we present velocities and forces where high frequency noise is

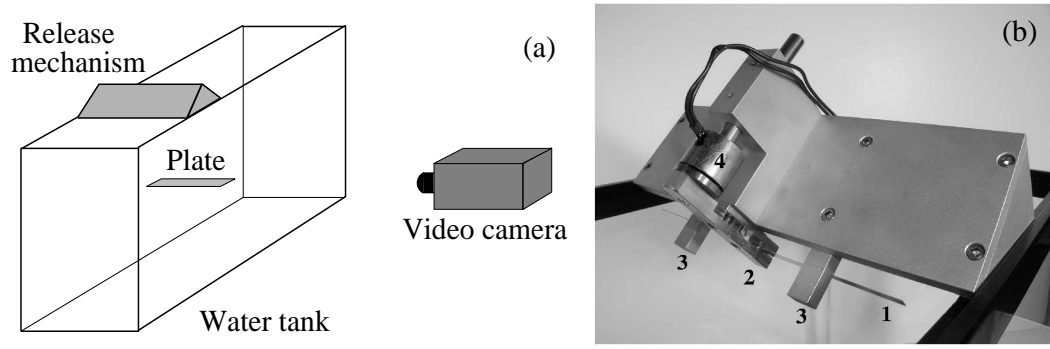


Figure 3.1: The experimental apparatus. (a) the transparent glass container, the release mechanism, the falling plate, and the high speed digital video camera shown schematically. (b) the release mechanism mounted on top of the container. The aluminum plate (1) is held at its midpoint by the clamp (2) below the water surface and it is aligned horizontally using the two bars (3). The plate is released when the clamp is opened using the small electromagnet (4).

filtered out.

This setup is different from those used in previous experimental works on free-falling bodies. In [7] the container is narrow and the plates touch the sides of the container to constrain their motion to be two-dimensional. In the setup used by [33] the length to width ratio was between 3 and 4, and tip plates were used to reduce three-dimensional effects. In the present experiment the plates are released so that they rotate about their axis of symmetry in the length direction and fall with two-dimensional trajectories in the plane normal to the length direction. The plates thus fall through the water without any constraints on their motion and without touching the walls of the container. Since the plate motion depends sensitively on the drag and the dissipative fluid torque, any additional damping from friction between the plate and the container walls could affect the behavior at the turning

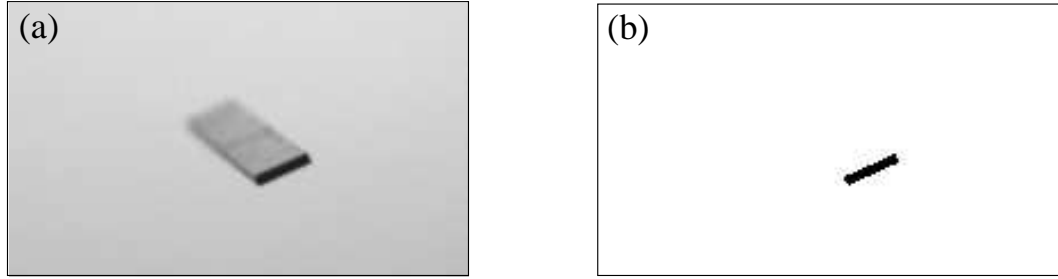


Figure 3.2: (a) A frame from the high speed video of the tumbling trajectory shown in figure 4.1. (b) The same frame converted to the black and white image used to determine the center of mass and orientation of the plate.

points in particular. Here such additional damping is absent since there are 5 cm between the plate tips and the container walls. The results of this experiment are compared with two dimensional numerical simulations in section 4.3. This comparison shows that the experiment described above produces trajectories that are qualitatively the same as those displayed by a system that is strictly two-dimensional. The difference in the setups might explain the discrepancies between the findings in the transition region between fluttering and tumbling presented in [7] and those discussed in chapter 4.

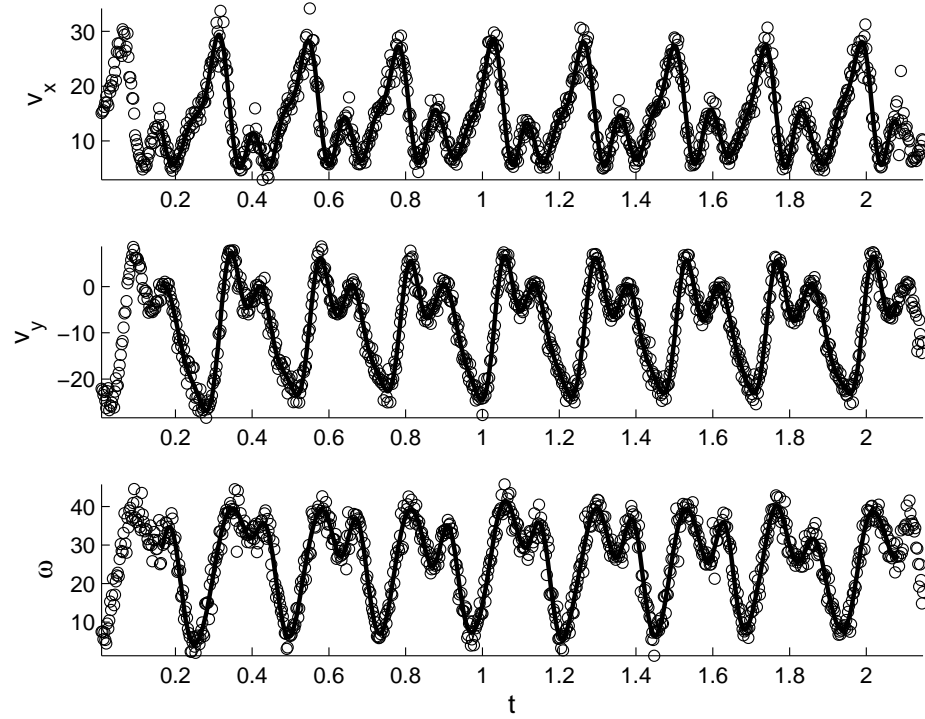


Figure 3.3: Horizontal and vertical components of the velocity v_x and v_y and angular velocity ω of the plate shown in figure 4.1 (c). The solid lines show velocities obtained by filtering the noise with a Fourier filter. The dots show velocities obtained with a single stencil derivative of the center of mass position.

Chapter 4

Trajectories and flows

4.1 Non-dimensional parameters and phase diagram

A freely falling plate is characterized by six dimensional parameters, i.e., the width of the plate, l , the thickness of the plate, h , the density of the plate, ρ_s , the density of the fluid, ρ_f , the kinematic viscosity of the fluid, ν , and the acceleration due to gravity, g . From the six dimensional numbers we form three non-dimensional numbers, i.e., the thickness to width ratio, β , the dimensionless moment of inertia, I^* , and the Reynolds number, Re . Specifically we define the thickness to width ratio of the plate cross-section

$$\beta = \frac{h}{l}, \quad (4.1)$$

and the dimensionless moment of inertia [33]:

$$I^* = \frac{32 I}{\pi \rho_f l^4}, \quad (4.2)$$

where $\pi \rho_f l^4/32$ is the moment of inertia per length about the axis of symmetry of a cylinder of density ρ_f and diameter l . With rectangular cross-section we have $I^* = 8 \rho_s h (l^2 + h^2) / (3 \pi \rho_f l^3)$ and with elliptical cross-section $I^* = \rho_s h (l^2 + h^2) / (2 \rho_f l^3)$. We define the Reynolds number using the width of the plate and the descent speed

$$\text{Re} = \frac{l V}{\nu}. \quad (4.3)$$

A simple estimate of the average descent speed, V , at intermediate Re gives:

$$V \approx \sqrt{2 (\rho_s/\rho_f - 1) h g} . \quad (4.4)$$

The estimate is obtained by balancing the buoyancy corrected gravity, $(\rho_s - \rho_f) h l g$, with the quadratic drag, $\rho_f l V^2/2$. However, [41] and [33] used the measured value of the average descent speed in the definition of the Reynolds number and we shall follow their convention.

[33] found a phase diagram for rectangular plates qualitatively similar to the phase diagram for circular disks measured by [41]. The plates descend steadily when Re is below 100, and a transition from fluttering to tumbling takes place with increasing I^* at larger values of Re . [33] measured the transition value of I^* to be $0.2 - 0.3$, whereas [7] found a transition value of 0.4 in their quasi two-dimensional experiment.

4.2 Trajectories

The measured trajectories of aluminum plates with different thickness to width ratio show a number of interesting characteristics. We use plates with rectangular cross-section and thickness to width ratio between $\beta = 1/14$ and $\beta = 1/5$. Figure 4.1 shows the trajectories of three of the four experimental plates, and table 4.1 summarizes the experiment, a fluttering plate with $\beta = 1/14$, two tumbling plates with $\beta = 1/5$ and $\beta = 1/8$, respectively, and a plate with $\beta = 1/6$ showing apparently chaotic motion. The nature of the transition between these qualitatively different behaviors is studied in chapter 6 by direct numerical simulations and by analyzing a reduced model of ordinary differential equations.

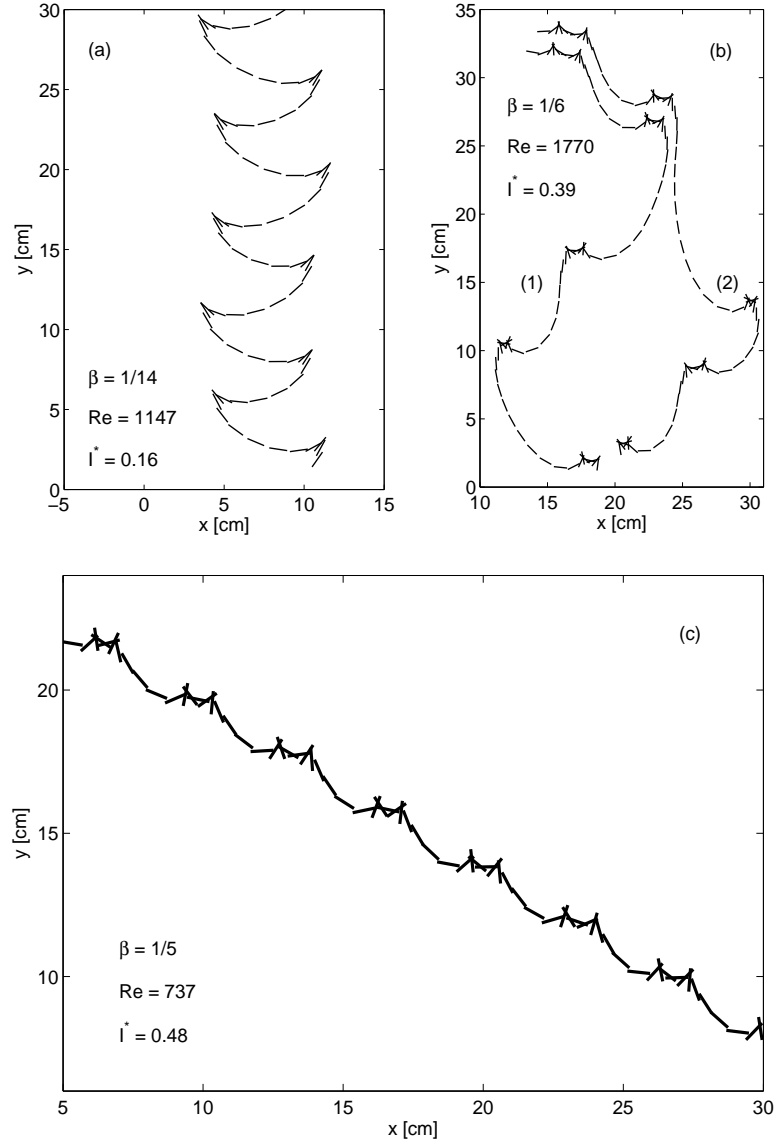


Figure 4.1: Measured plate trajectories. (a) the fluttering plate with $h = 0.081$ cm and $\beta = 1/14$, (b) two apparently chaotic trajectories for the $h = 0.162$ cm and $\beta = 1/6$ plate, and (c) the tumbling plate with $h = 0.162$ cm and $\beta = 1/5$. For clarity the two trajectories in (b) are displaced from each other 0.5 cm horizontally and 1.5 cm vertically. The thick line segments show the plate cross-sections with time-intervals of 0.04 s in (a) and 0.025 s in (b) and (c).

Table 4.1: The thickness h , the non-dimensional parameters β , I^* , and Re , and the measured average horizontal velocity $\langle v_x \rangle$, vertical velocity $\langle v_y \rangle$, and angular velocity $\langle \omega \rangle$. The Reynolds number defined in equation (4.3) is obtained using $\langle v_y \rangle$ and the kinematic viscosity of water at 25° C, i.e., $\nu = 0.0089 \text{ cm}^2 \text{ s}^{-1}$. The averages for $\beta = 1/5$ are based on 10 trajectories with 8 periods each, the averages for $\beta = 1/8$ are based on 20 trajectories with 3 periods each, and the averages for $\beta = 1/14$ are based on 10 trajectories with 5 periods each. For the plates with $\beta = 1/6$ and $\beta = 1/14$ we report the averages of the absolute values of v_x and ω .

h [cm]	β	I^*	Re	$\langle v_x \rangle$ [cm s ⁻¹]	$\langle v_y \rangle$ [cm s ⁻¹]	$\langle \omega \rangle$ [rad s ⁻¹]
0.162	1/5	0.48	737	14.2 ± 0.1	-8.1 ± 0.3	25.5 ± 0.3
0.162	1/6	0.39	1770	15.2 ± 0.7	-16.2 ± 2.9	16.1 ± 1.1
0.081	1/8	0.29	837	15.9 ± 0.3	-11.5 ± 0.5	14.5 ± 0.3
0.081	1/14	0.16	1147	19.8 ± 0.3	-9.0 ± 0.2	6.8 ± 0.1

4.2.1 Fluttering

Figure 4.1(a) shows the trajectory and the solid lines in figure 4.2 show the velocity components for the fluttering plate with $h = 0.081$ cm and $\beta = 1/14$. The plate oscillates from side to side as it descends with alternating gliding at low angle of attack and fast rotational motion at the turning points. The center of mass elevates at the turning points, and the turning points are cusp-like since the translational motion almost ceases. This is a signature of the dependence of the aerodynamic lift on the rotation of the plate (see section 5.3).

The periodic motion of a fluttering plate is in general complex and not easy to describe by simple functions. However, it is evident from the measured translational velocity components shown in figure 4.2 that the fluttering of the plate with $\beta = 1/14$ is dominated by the lowest harmonics. The trajectory is well-described by the simple curve

$$x(t) = \frac{V_1}{\Omega} \sin(\Omega t) , \quad (4.5)$$

$$y(t) = -V_2 t - \frac{V_3}{2\Omega} \cos(2\Omega t) , \quad (4.6)$$

where Ω , V_1 , V_2 , and V_3 are constants. The constant Ω is the angular frequency of the periodic motion, V_2 is the average descent speed, and V_1 and V_3 describe the amplitudes of the oscillations in v_x and v_y , respectively. Figure 4.3 shows the curve (4.5) and (4.6) with the parameters $\Omega = 9.8 \text{ rad s}^{-1}$, $V_1 = 32.6 \text{ cm s}^{-1}$, $V_2 = 9.1 \text{ cm s}^{-1}$, and $V_3 = 14.5 \text{ cm s}^{-1}$ obtained from the fits shown by the two dotted lines in figure 4.2.

The frequency of the oscillatory component of the vertical velocity is twice the frequency of the oscillatory horizontal velocity component because of the symme-

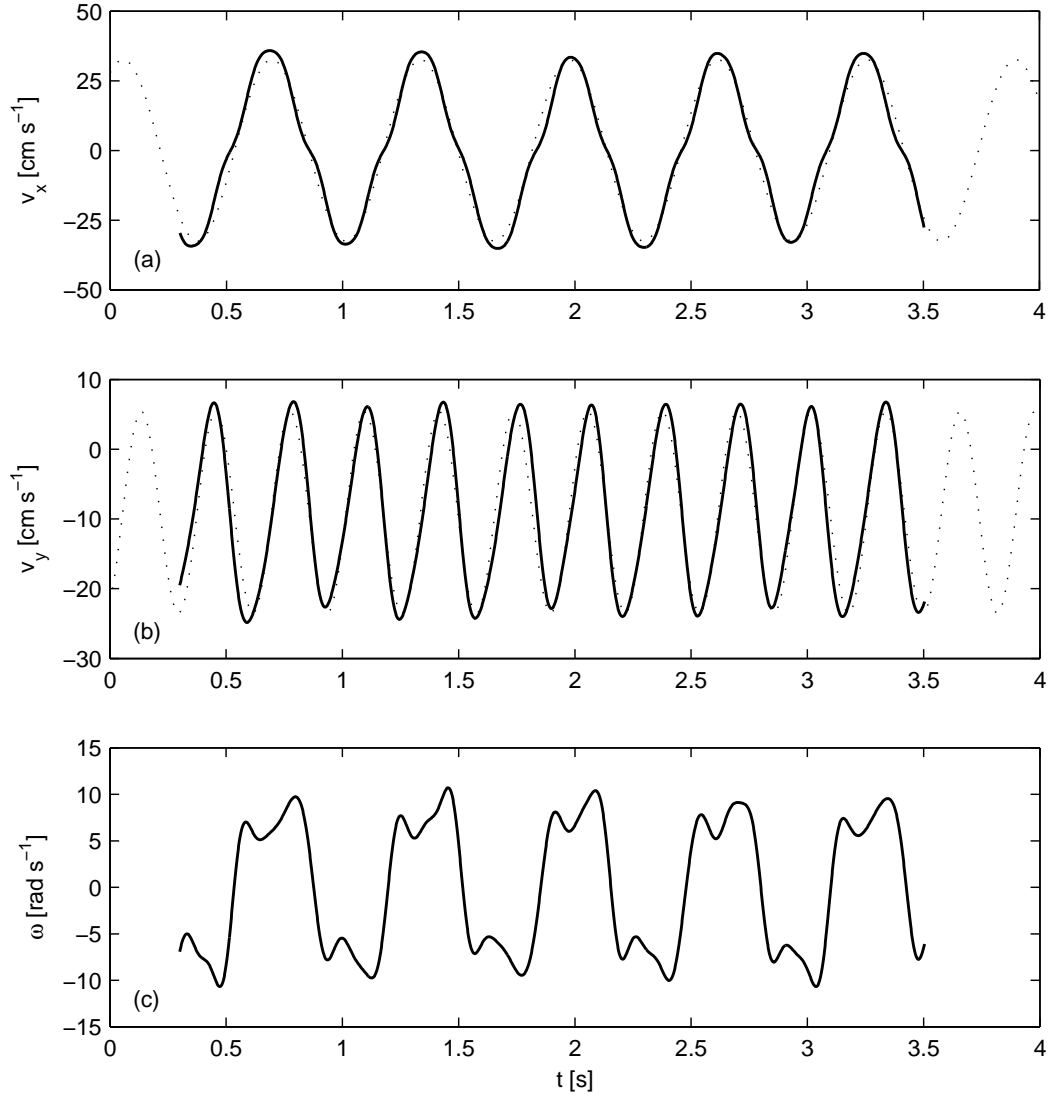


Figure 4.2: The measured velocities (solid lines) for fluttering with $h = 0.081$ cm and $\beta = 1/14$, and the best fits (dotted lines) of the velocity expressions derived from equations (4.5) and (4.6). (a) the horizontal velocity component v_x , (b) the vertical velocity component v_y , and (c) the angular velocity ω . Both v_x and v_y are well-described by a single harmonics, whereas 3 harmonics are needed to capture the main features of ω with three local extrema for each half-period.

try of the fluttering motion. Any solution with periodic and symmetric side to side oscillations and constant average descent speed will therefore in general contain terms like (4.5) and (4.6). A special example of such motion is that of a rigid object with elliptical cross-section in a two-dimensional inviscid flow without gravity and circulation [18]. The problem is described by Kirchhoff's equations, and the small amplitude analytical solution consists of symmetric side to side oscillations. However, the phase difference between the two oscillatory components and the rotational motion in the ideal fluid problem are different from the fluttering trajectory of a thin plate falling in a viscous fluid.

4.2.2 Tumbling

Figure 4.1(c) shows the trajectory and figure 4.4 the velocity components as functions of time for the tumbling plate with $h = 0.162$ cm and $\beta = 1/5$. The plate is released at an angle of 60° with the horizontal, and it settles into periodic motion after one to two complete rotations. The periodic motion alternates between short and long gliding segments, and tumbling motion has the pronounced period-two structure also observed in the direct numerical simulations presented in chapter 6. The plate rotates fast at the turning points with angular velocities up to $\omega = 40$ rad s $^{-1}$ as shown in figure 4.4(c). The center of mass elevates following the long gliding segments whereas it does not elevate following the short gliding segments as shown in figure 4.4(b).

4.2.3 Apparently chaotic motion

Figure 4.1(b) shows two typical trajectories for the $h = 0.162$ cm and $\beta = 1/6$ plate with apparently chaotic motion, and figure 4.5 shows the velocity components

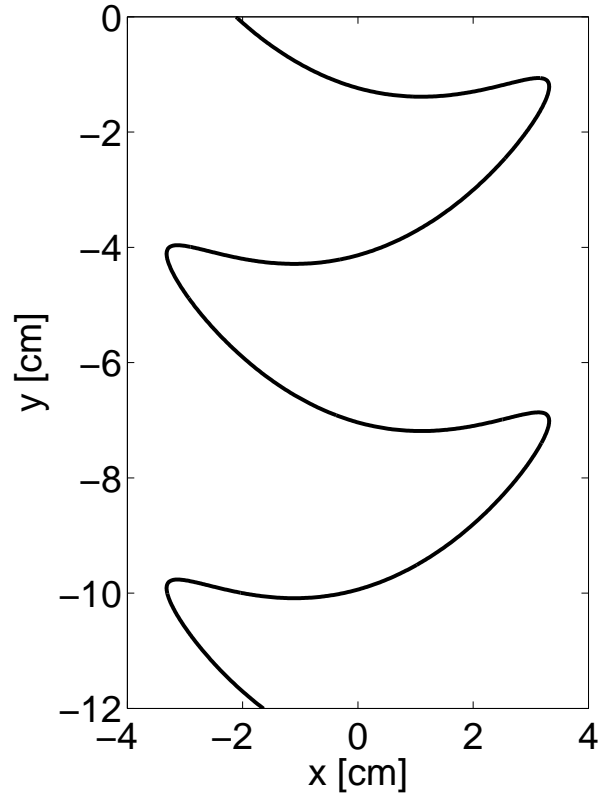


Figure 4.3: The simple analytical curve (4.5) and (4.6) describes the fluttering trajectory for the plate with $\beta = 1/14$ shown in figure 4.1(a). The curve parameters are obtained by fitting the translational velocity components as shown by the two dotted lines in figure 4.2.

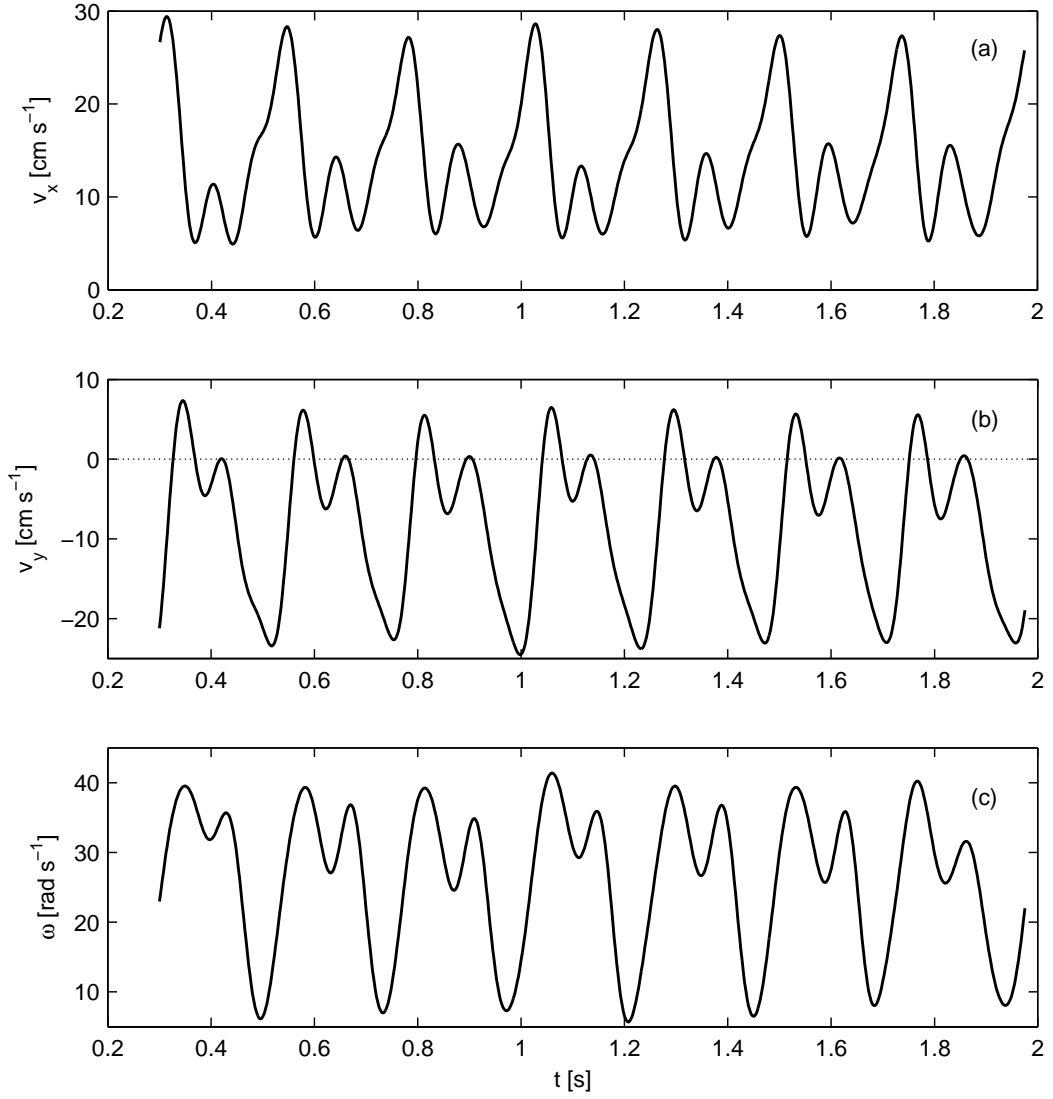


Figure 4.4: Measured velocities as functions of time for the tumbling plate with $h = 0.162$ cm and $\beta = 1/5$. (a) the horizontal velocity component, (b) the vertical velocity component, and (c) the angular velocity. The plate elevates (v_y is positive) after the long gliding segments whereas it does not elevate after the short gliding segments. The local maxima for v_y and ω almost coincide, and we note that v_x is large and ω is small during the long gliding segments.

as functions of time for plate (1) in figure 4.1(b). The motion in the transition region between fluttering and tumbling alternates between fast complete rotations and segments where the plate glides at low angle of attack for distances up to 15 times the plate width. The two trajectories start out with similar initial conditions, but the dynamics is very sensitive to the initial conditions of the plate and the water. Both plates end up almost at rest and oriented vertically after a few complete rotations, and in this state it is undetermined whether the plates will flutter or tumble. Plate (1) therefore glides to the left whereas plate (2) glides to the right. The apparently chaotic motion is radically different from the periodic fluttering and tumbling with short transients, and when the plates are almost at rest and oriented vertically the dynamics is much more sensitive to experimental noise than in the periodic regions. We note that [13] observed similar apparently chaotic motion for freely falling disks, whereas apparently chaotic motion was not found in the experiment by [7].

In chapter 6 we have present direct numerical simulations at somewhat lower Reynolds number showing a wide transition region between fluttering and tumbling in which the plates flutter periodically but tumble once between consecutive turning points [2]. Within the framework of a quasi-steady model we analyze the transition between fluttering and tumbling for plates with small thickness to width ratio for which the dimensionless moment of inertia is the relevant control parameter. We identify the transition in the quasi-steady model as a heteroclinic bifurcation, and using the direct numerical simulations we found that the transition between fluttering and tumbling does not always take place via a sequence of chaotic solutions. These results could suggest that the apparently chaotic trajectories are observed in the present experiment because the system is very sensitive

to noise in the transition region and that the trajectories only appear to be chaotic due to experimental noise.

4.3 Comparison between experiment and direct numerical simulations

To validate and check the measurements and the direct numerical simulations we compare measured and computed trajectories for the tumbling plate with $\beta = 1/8$. We keep the width and the thickness the same in the experiment and the simulations, but the plate in the experiment has rectangular cross-section whereas the plate in the simulations has elliptical cross-section to take advantage of a conformal mapping with a simple analytic form and no singular corners. Both the mass and the moment of inertia are therefore smaller in the simulations in comparison with the experiment. With the rectangular cross-section we have $I^* = 0.29$ and $\text{Re} = 837$ and with the elliptical cross-section $I^* = 0.17$ and $\text{Re} = 1025$. The measurements were repeated 20 times with initial conditions set by releasing the plate at an angle of 45° with the horizontal, and the simulations were carried out with the 5 different sets of initial conditions (I – V) specified in table 4.2.

Figure 4.6(a) shows the plate trajectories and figure 4.6(b) shows v_x versus v_y for two representative trajectories, one measured and one computed. The trajectories are qualitatively similar, but the period-two structure is more pronounced in the simulations as shown in figure 4.6(b). We ascribe the differences between the trajectories to the differences between the rectangular and the elliptical cross-section. The average velocity components, angular velocity, and angle of descent are reported in table 4.3. The average tumbling frequency in the simulations is

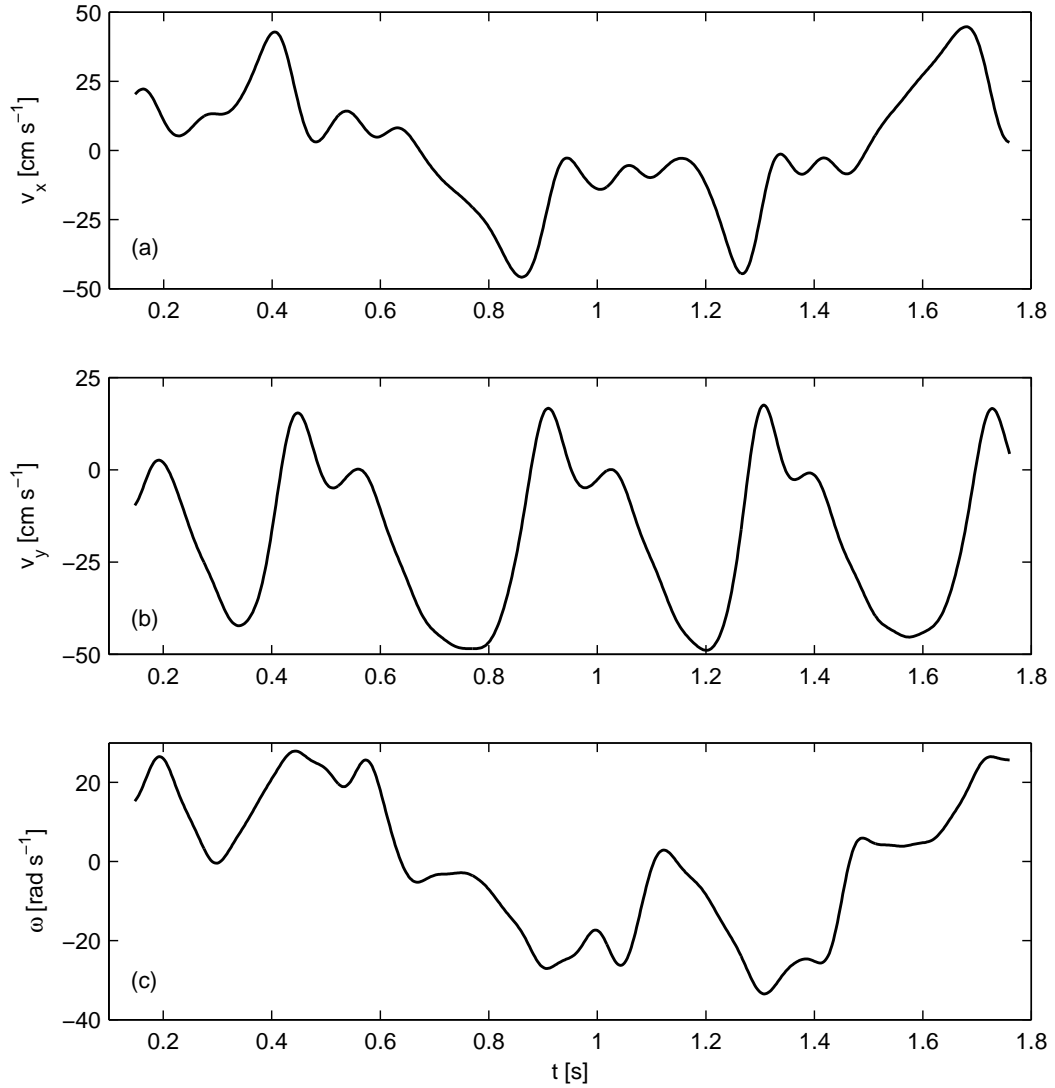


Figure 4.5: Measured velocities as functions of time for the plate with $h = 0.162$ cm and $\beta = 1/6$ displaying irregular motion, see trajectory (1) in figure 4.1(b). (a) the horizontal velocity component, (b) the vertical velocity component, and (c) the angular velocity. The irregular motion involves long gliding segments at low angle of attack with descent velocities up to $v_y = -50 \text{ cm s}^{-1}$ followed by center of mass elevation with upward velocities up to $v_y = 20 \text{ cm s}^{-1}$.

Table 4.2: Initial conditions for the plates in the direct numerical simulations.

I – V: $\beta = 1/8$, $h = 0.081 \text{ cm}$, $\rho_f = 1.0 \text{ g cm}^{-3}$, $\rho_s = 2.7 \text{ g cm}^{-3}$, and $\nu = 0.0089 \text{ cm}^2 \text{ s}^{-1}$; VI – VII: $\beta = 1/4$, $h = 0.05 \text{ cm}$, $\rho_f = 1.0 \text{ g cm}^{-3}$, $\rho_s = 2.0 \text{ g cm}^{-3}$, and $\nu = 0.0089 \text{ cm}^2 \text{ s}^{-1}$.

β	Run	$v_x[\text{cm s}^{-1}]$	$v_y[\text{cm s}^{-1}]$	$\omega[\text{rad s}^{-1}]$	$\theta[\text{deg}]$
1/8	I	0.00	0.00	0.00	11.5
-	II	0.00	0.00	-16.50	-11.5
-	III	-8.92	-8.92	0.00	45.3
-	IV	-17.90	-17.90	0.00	45.3
-	V	-35.70	53.40	0.00	45.3
1/4	VI	0.00	0.00	0.00	11.5
-	VII	0.00	0.00	-2.90	-11.5

Table 4.3: Average velocities $\langle v_x \rangle$ and $\langle v_y \rangle$, angular velocity $\langle \omega \rangle$, and angle of descent for the tumbling plate with $\beta = 1/8$ in the experiment (rectangular cross-section) and in the direct numerical simulations (elliptical cross-section) with initial conditions (I – V) in table 4.2.

	$\langle v_x \rangle$ [cm s ⁻¹]	$\langle v_y \rangle$ [cm s ⁻¹]	$\langle \omega \rangle$ [rad s ⁻¹]	Descent angle [deg]
Experiment:	15.9 ± 0.3	-11.5 ± 0.5	14.5 ± 0.3	35.8 ± 1.3
Simulation:	15.6 ± 0.2	-7.4 ± 0.3	18.0 ± 0.3	25.3 ± 0.9

25 % higher than the average tumbling frequency in the experiment. The average angle of descent relative to the horizontal is 25.3° in the simulations and 35.8° in the experiments, and the average descent velocity is about 50 % larger in the experiments than in the simulations. The standard deviations are comparable in the experiments and in the simulations as reported in table 4.3.

4.4 Sensitivity to initial conditions

In order to average different experimental runs, it is important to know how the trajectories obtained depend on the initial conditions. We investigate numerically the dependence on initial conditions by specifying different initial conditions of the plate as summarized in table 4.2. Figure 4.7(a) shows the trajectories of the plate with $\beta = 1/8$ in two simulations with 10 complete periods and initial conditions I and II from table 4.2. The initial transients of the two runs are very different, as expected, but after two complete rotations the two trajectories span the same region in the v_x versus v_y plot and exhibit similar period-two dynamics as shown in figure 4.7(b). However, the initial conditions have significant importance in some

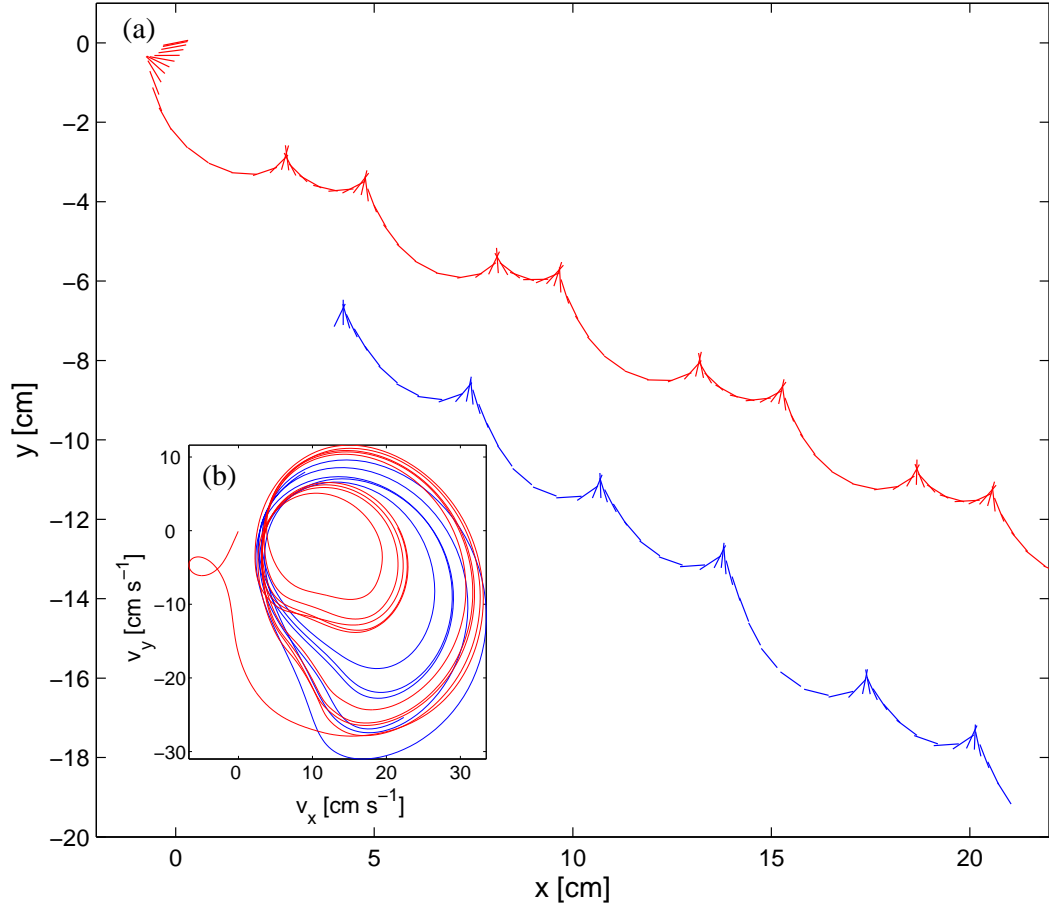


Figure 4.6: Tumbling dynamics with $\beta = 1/8$ from the experiment (blue) and the direct numerical simulation (red) with initial condition I in table 4.2. (a) trajectories and (b) v_x versus v_y . The trajectories are qualitatively similar, and we ascribe the quantitative differences to the difference in geometry between the rectangular and the elliptical cross-section.

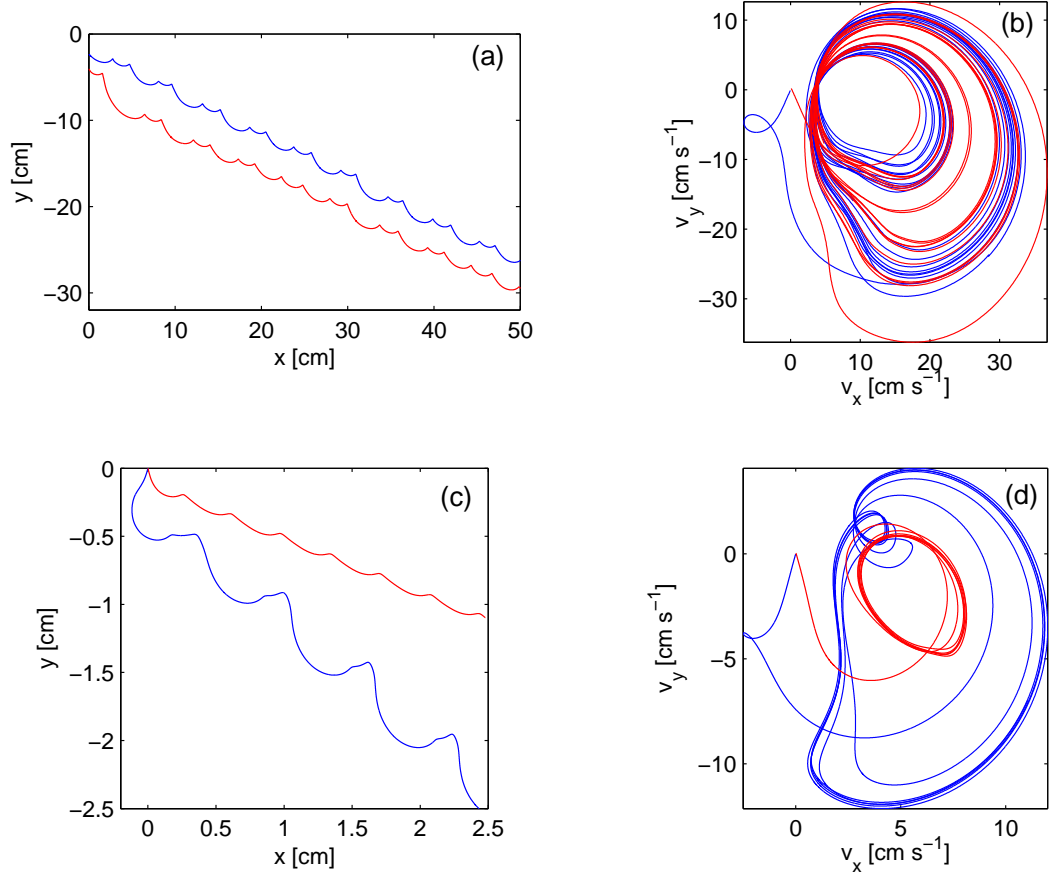


Figure 4.7: Dependence on initial conditions of periodic solutions. (a) trajectory and (b) v_x versus v_y for a tumbling plate with $\beta = 1/8$, $\text{Re} = 1025$, and $I^* = 0.17$ with initial condition I (blue) and II (red) from table 4.2; (c) trajectory and (d) v_x versus v_y for a tumbling plate with $\beta = 1/4$, $\text{Re} = 10^2$, and $I^* = 0.36$ with initial condition VI (blue) and VII (red) from table 4.2.

cases. The apparently chaotic trajectories shown in figure 4.1(b) depend sensitively on the initial conditions, and periodic solutions can also depend sensitively on the initial conditions as shown in figures 4.7(c) and 4.7(d). One trajectory (blue) displays a pronounced period-two structure whereas the other trajectory (red) displays a simple period-one structure. Dependence on initial conditions is also observed in the band of periodic states observed numerically in the transition from fluttering to tumbling (see chapter 6).

4.5 Vortex shedding and wake structure

Measuring the wake of a free falling body experimentally is a very difficult task. On the other hand direct numerical simulations can provide very high resolution vorticity fields in both time and space. Two representative cases of tumbling and fluttering ellipses are shown in the following.

4.5.1 Tumbling

The wake of the tumbling plate with $\beta = 1/8$ consists of vortices shed at the turning points plus vortex pairs formed by the breakup of the extended wake formed during gliding. Figure 4.8 shows snapshots of the vorticity field around the plate. The vortex pair in the top left corner of each frame was shed after the initial fluttering transient. The plate starts gliding after the transient, and the trajectory alternates between short and long gliding segments separated by 180° rotations. As the plate initiates a turn, the wake developed during the previous gliding segment becomes unstable and breaks up into vortices with a characteristic size of half the plate width. In addition, two vortices are shed when the plate undergoes a 180° rotation and resumes gliding. The short gliding segments are

similar to the long gliding segments except that the wake of the plate has less time to develop and generates fewer vortices as it breaks up.

4.5.2 Fluttering

Figure 4.9 shows the vorticity field around a fluttering plate with elliptical cross-section, $\beta = 1/18$, $I^* = 0.057$, and $\text{Re} = 412$. Numerically we have not resolved the $\beta = 1/14$ fluttering, and to illustrate the wake structure in fluttering we consider an example at somewhat lower Reynolds number. The vortex dipole shed during the initial transient is visible at the top left corner in figure 4.9(a). A similar dipole is shed during the transient of the tumbling plate shown in figure 4.8. In both cases the plate glides at small angle of attack after the transient until it starts to pitch up and approach the turning point. As the plate pitches up it decelerates, its wake becomes unstable, and its center of mass elevates. The old leading and trailing edge vortices are shed as the plate resumes gliding.

4.6 The Strouhal number for a freely falling plate

Figure 4.10(a) shows the vorticity field for a tumbling plate with elliptical cross-section and $\beta = 1/2$, $I^* = 0.84$, and $\text{Re} = 832$. The freely falling plate rotates continuously and an extended wake is therefore not formed. Two vortices of similar magnitude but opposite sign are shed during each half period as the plate rotates, and the wake therefore consists of a sequence of vortex dipoles. For comparison figure 4.9(b) shows a numerical simulation of the flow around a plate with $\beta = 1/2$, which is translating with fixed angle of attack equal to 45° and velocity equal to the average translational velocity of the tumbling plate. The vortex shedding frequency, f , the vortex strengths, and the distances between vortices of the same

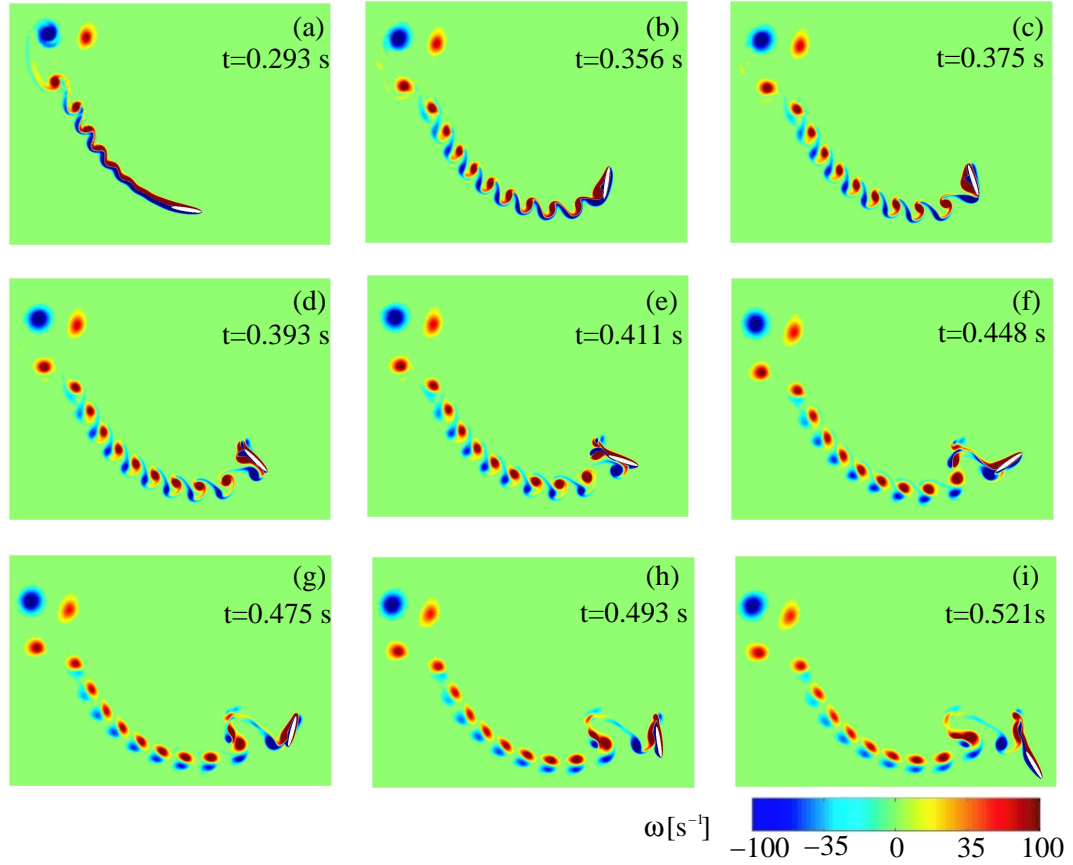


Figure 4.8: The vorticity around the tumbling plate with $\beta = 1/8$, $I^* = 0.17$, and $\text{Re} = 1025$. The grid resolution was 512×1024 . Positive vorticity in red and negative vorticity in blue. (a) onset of the wake instability; (b) the instability is fully developed, and the plate has initiated its first turn; (c)–(d) a vortex pair is formed as the plate completes its turn; (e) the plate glides for a short distance; (f)–(h) the plate makes a second 180° turn; and (i) the plate resumes gliding.

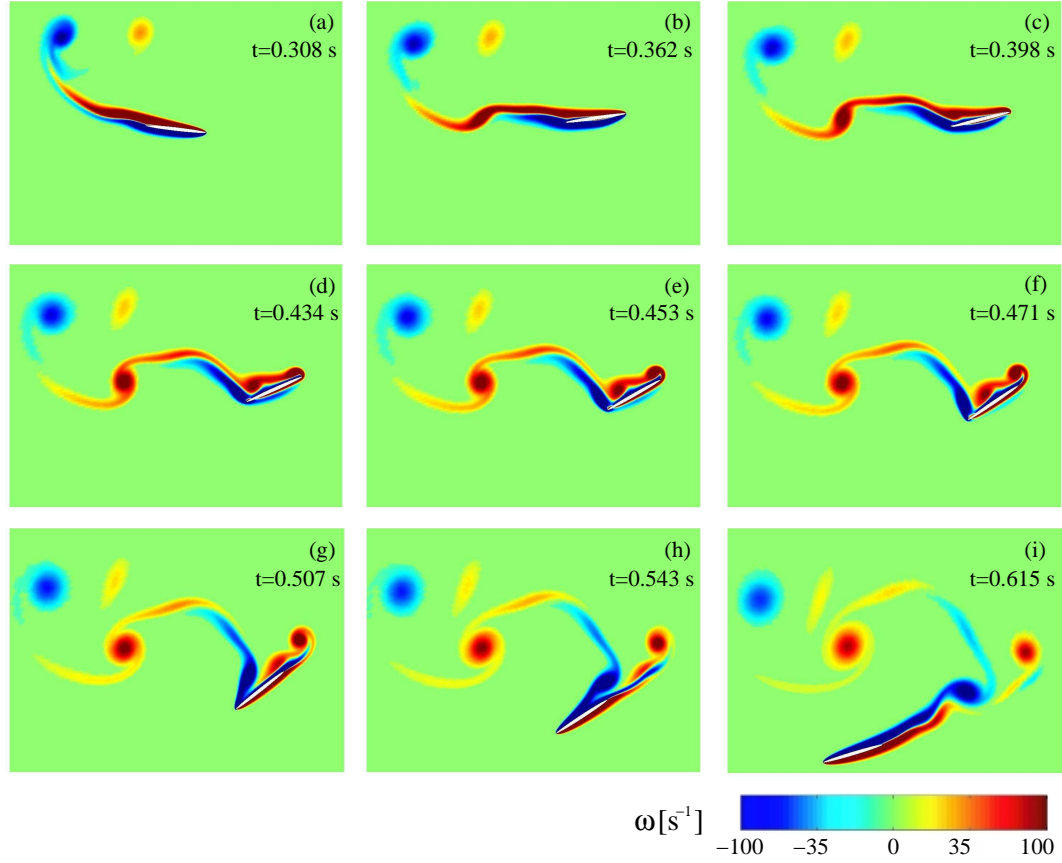


Figure 4.9: The vorticity around the fluttering plate with $\beta = 1/18$, $I^* = 0.057$, and $\text{Re} = 412$. The grid resolution was 512×1024 . Positive vorticity in red and negative vorticity in blue. (a) the plate glides at small angle of attack; (b) the plate pitches up and its center of mass elevates; (c) the plate slows down; (d)–(f) the plate rotates and starts to shed its old leading edge vortex (red); (g)–(h) the old trailing edge vortex (blue) is shed; (i) the plate resumes gliding.

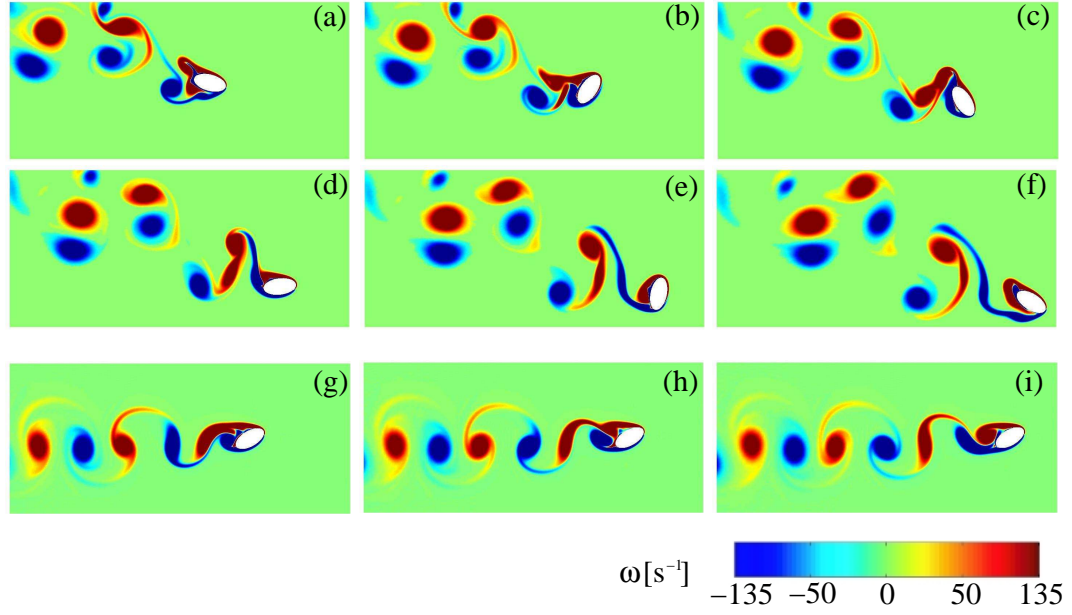


Figure 4.10: Vorticity fields with positive vorticity in red and negative vorticity in blue. The grid resolution was 512×1024 , and the time between consecutive fields was 0.0193 s. (a)–(f) tumbling plate with $\beta = 1/2$, $I^* = 0.84$, and $\text{Re} = 832$; (g)–(i) plate with $\beta = 1/2$ translating with velocity equal to the average translational velocity of the tumbling plate. In (a)–(f) a vortex pair is shed during every 180° rotation and in (g)–(i) a von Kármán vortex street is formed.

sign for the tumbling plate in figure 4.10(a) are comparable to those of the von Kármán vortex street of the translating plate in figure 4.10(b). The Strouhal number, $\text{St} = lf/V$, for the freely falling plate is $\text{St} = 0.24$. For plates in a fixed oncoming flow we find $0.23 < \text{St} < 0.43$ as the angle of attack is decreased from 90° to 0° , and with angle of attack equal to 45° as in figure 4.9(b) we have $\text{St} = 0.32$.

Chapter 5

Fluid forces: measurements and quasi-steady model

5.1 Experiment and direct numerical simulations

In the quasi two-dimensional experiment described in chapter 3, we extract the fluid force, \mathbf{F} , and the fluid torque, τ , per unit length on the plate directly from the measured accelerations, i.e., $F_x = m \dot{v}_x$, $F_y = m \dot{v}_y + m' g$, and $\tau = I \ddot{\theta}$, where $m = \rho_s h l$, $m' = (\rho_s - \rho_f) h l$, and $I = \rho_s h l (l^2 + h^2)/12$. Figure 5.1 shows F_x , F_y , and τ as functions of the angle θ . In the following we compare the forces measured experimentally with those obtained numerically for $\beta = 1/8$. For numerical reasons the numerical forces are obtained with an elliptical cross-section, while the experiments were conducted with a rectangular cross-section. The period of oscillation of the plate with elliptical cross-section is shorter than the period of oscillation of the rectangular plate, and for comparison we show the force components and the torque as functions of θ and not as functions of time directly. The measured and the computed forces have qualitatively similar angular dependence and the peak values are comparable.

The buoyancy corrected gravity is $(\rho_s - \rho_f) l h g = 88 \text{ g s}^{-2}$ for the rectangular plate and $\pi (\rho_s - \rho_f) l h g / 4 = 69 \text{ g s}^{-2}$ for the plate with elliptical cross-section. The measured torque is approximately twice as large as the computed torque. However the moment of inertia of the rectangular plate is also approximately twice as large as the moment of inertia of the plate with elliptical cross-section. The computed and the measured torque normalized by the moment of inertia are therefore

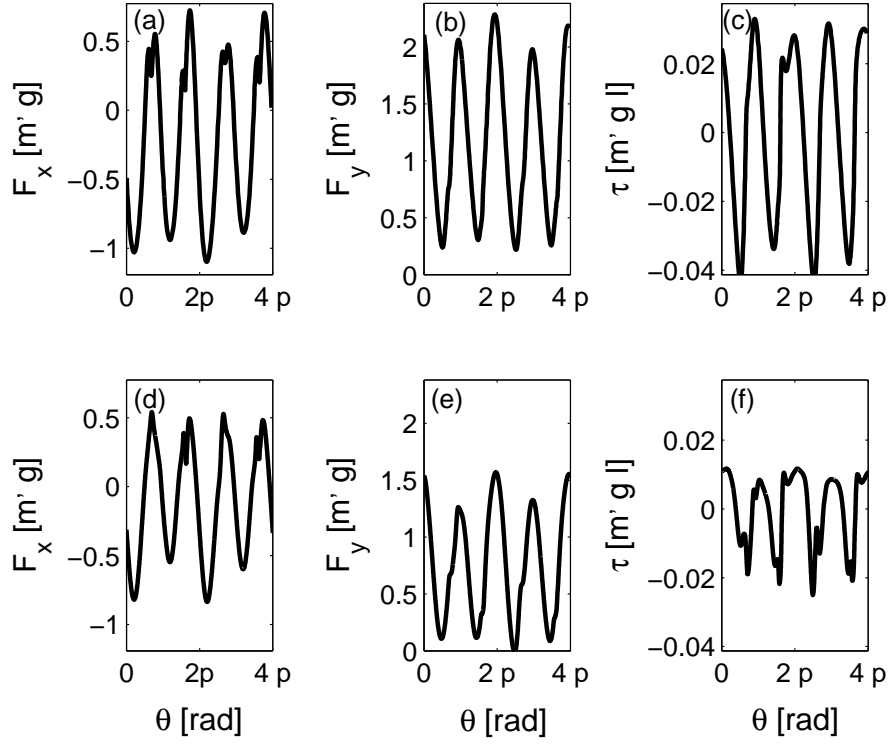


Figure 5.1: The fluid force components and the fluid torque as functions of the angle θ for the tumbling plates with $\beta = 1/8$. (a) – (c) experiment and (d) – (f) direct numerical simulation with initial condition I. In both cases we use units where $m' = (\rho_s - \rho_f) h l$. The measured and the computed force and torque are qualitatively similar and we ascribe the quantitative differences between measurements and computations to the differences in geometry.

comparable. The net fluid force acts close to the center and the arm of the fluid force is only about 1/100 of the width of the plate. The fluid torque is very small in comparison with the fluid torque on a glider with fixed angle of attack as shown in figure 5.2 for both small and large angle of attack.

5.2 Quasi-steady force model

In order to quantify the main contributions to the fluid forces we consider a phenomenological model based on ordinary differential equations. We model the two-dimensional dynamics of a rigid card falling in a fluid by ordinary differential equations with fluid force contributions from lift, drag and added mass. We apply a quasi-steady approximation in which the fluid forces are expressed in terms of the kinematic variables of the card alone. The Reynolds number based on the semi-major axis and the average descent velocity of a paper card falling in air is of the order of 10^3 . The quadratic lift and drag terms in the model are designed to describe the aerodynamics at such intermediate Reynolds numbers between 10^2 and 10^3 . We assume that the card has elliptical cross-section with half-major axis, a , and half-minor axis, b . We write the equations in the coordinate system co-rotating with the plate, and we define $v_{x'}$, $v_{y'}$, and θ as shown in figure 5.3. The velocity components $v_{x'}$ and $v_{y'}$ are related to the horizontal velocity component, v_x , and the vertical velocity component, v_y , by the transformation: $v_x = v_{x'} \cos \theta - v_{y'} \sin \theta$ and $v_y = v_{x'} \sin \theta + v_{y'} \cos \theta$.

Our model consists of the following set of coupled ordinary differential equations

$$(m + m_{11}) \dot{v}_{x'} = (m + m_{22}) \dot{\theta} v_{y'} - \rho_f \Gamma v_{y'} - m' g \sin \theta - F_{x'}^\nu, \quad (5.1)$$

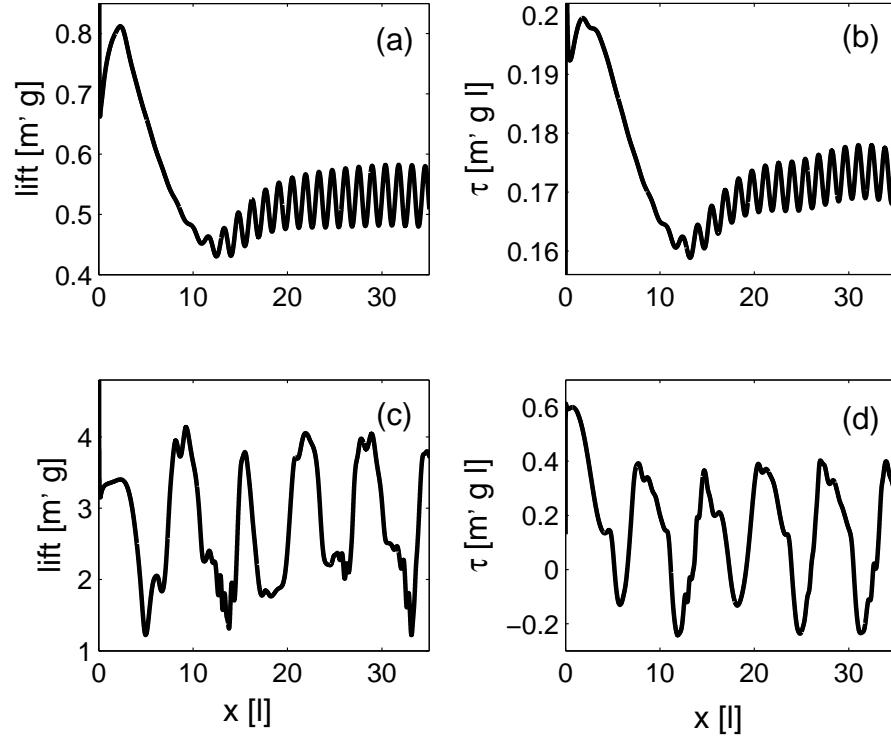


Figure 5.2: The computed lift and fluid torque on steadily translating plates with $\beta = 1/8$ and fixed angle of attack, α , as functions of the distance traveled. The plates were impulsively started and the Reynolds numbers based on the width and the translational speed were 10^3 . (a) – (b) low angle of attack $\alpha = 10^\circ$ and (c) – (d) high angle of attack $\alpha = 40^\circ$. The torques are one to two orders of magnitude larger than the torques on the freely falling plates in figure 5.1.

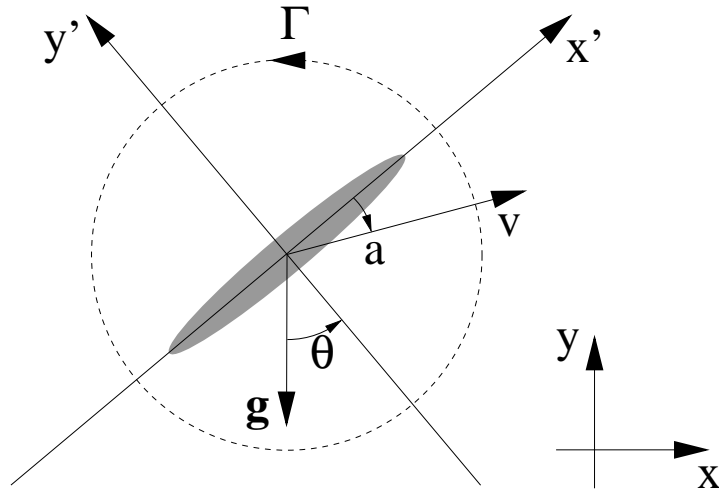


Figure 5.3: The velocity components $v_{x'}$ and $v_{y'}$ in the laboratory reference frame are defined with respect to the coordinate system following the rotation of the body, whereas v_x and v_y are the horizontal and the vertical velocity component in the laboratory reference frame, respectively. The angle of attack, α , satisfies $\alpha \in [-\pi/2, \pi/2]$ and it is negative in the example sketched.

$$(m + m_{22}) \dot{v}_{y'} = -(m + m_{11}) \dot{\theta} v_{x'} + \rho_f \Gamma v_{x'} - m' g \cos \theta - F_{y'}^\nu, \quad (5.2)$$

$$(I + I_a) \ddot{\theta} = (m_{11} - m_{22}) v_{x'} v_{y'} + l_\tau \rho_f \Gamma \sqrt{v_{x'}^2 + v_{y'}^2} - \tau^\nu. \quad (5.3)$$

The terms $m \dot{\theta} v_{y'}$ and $-m \dot{\theta} v_{x'}$ arise due to the co-rotating coordinate system, and the terms involving m_{11} , m_{22} , and I_a are due to added mass effects. The added mass coefficients m_{11} and m_{22} , and the added moment of inertia, I_a , are given by inviscid theory [30]. We use the coefficients for a plate with elliptical cross-section:

$$m_{11} = \frac{\pi}{4} \rho_f h^2, \quad m_{22} = \frac{\pi}{4} \rho_f l^2, \quad I_a = \frac{\pi}{128} \rho_f (l^2 - h^2)^2. \quad (5.4)$$

In the absence of viscous effects the model reduces to Kirchhoff's differential equations for a solid body in an inviscid and irrotational flow. In Kirchhoff's equations the fluid circulation has an arbitrary constant value. For discussion and analysis of the solutions of Kirchhoff's equations see [18], [16], and [4].

We decompose fluid forces into lift and drag. The lift is orthogonal to the direction of motion and proportional to the circulation, $\Gamma = \Gamma(v_{x'}, v_{y'}, \dot{\theta})$. The drag, $\mathbf{F}^\nu = \mathbf{F}^\nu(v_{x'}, v_{y'}, \dot{\theta})$, and the dissipative fluid torque, $\tau^\nu = \tau^\nu(v_{x'}, v_{y'}, \dot{\theta})$, are opposite to the direction of translation and rotation, respectively. In classical aerodynamics for wings with fixed angle of attack the fluid forces are conveniently decomposed into lift and drag. The situation is more complicated in fluttering and tumbling, since the center of mass velocity can point in any direction and almost vanishes at the turning points, where the angle of attack is large and the magnitudes of lift and drag are comparable. However, it is nevertheless convenient to use lift and drag terms to model the fluid forces in a quasi-steady model.

5.2.1 Circulation and Lift

The fluid circulation around the plate is not specified in Kirchhoff's equations and it must be modeled to complete equations (5.1) – (5.3). The plate dynamics is characterized by two velocity scales, i.e., the translational velocity and the rotational velocity of the plate, and we assume that the circulation depends on both velocities. We write the circulation as the sum of a term proportional to the translational speed and a term proportional to the angular velocity of the plate

$$\Gamma = -\frac{1}{2} C_T l \sqrt{v_{x'}^2 + v_{y'}^2} \sin 2\alpha + \frac{1}{2} C_R l^2 \dot{\theta} , \quad (5.5)$$

where α is the angle of attack defined in figure 5.3, and C_T and C_R are non-dimensional constants. By definition we have $\alpha \in [-\pi/2, \pi/2]$ and the sign convention described in the caption of figure 5.3. In terms of $v_{x'}$, $v_{y'}$, and $\dot{\theta}$ we write the circulation

$$\Gamma = -C_T l \frac{v_{x'} v_{y'}}{\sqrt{v_{x'}^2 + v_{y'}^2}} + \frac{1}{2} C_R l^2 \dot{\theta} . \quad (5.6)$$

At low angles of attack the translational lift term reduces to the classical Kutta-Joukowski lift for a translating wing with constant angle of attack, and at high angles of attack it takes stall into account [39]. The rotational lift term has the same form as the lift on a pitching plate at zero angle of attack for which $C_R = \pi$ as calculated by [26]. In the quasi-steady model we assume that the functional form is valid in general, but we determine C_R by fitting the measured lift. A justification for this choice based on numerical evidence is presented in section 5.3.

The present model of the circulation is different from previous models. [22] assumed a constant circulation, and [34] and [7] assumed that $\Gamma = -\pi l (v_{x'}^2 + v_{y'}^2)^{1/2} \sin \alpha$, i.e., the classical Kutta-Joukowski model. We show in the following

that neither of the previous lift models can account for the measured lift, and that the rotational lift dominates in tumbling.

The term $l_\tau \rho_f \Gamma (v_{x'}^2 + v_{y'}^2)^{1/2}$ describes the torque due to the translational and rotational lift. For a plate with elliptical cross-section in an ideal fluid with constant circulation we have $l_\tau = 0$, and for a translating wing at low angle of attack satisfying the Kutta condition we have $l_\tau = l/4$. In section 5.5 we compare the contributions to the fluid torque with the measured torque and discuss the value of l_τ further.

5.2.2 Drag and dissipative torque

We describe the drag using a standard model, which is valid for a translating wing with constant angle of attack at intermediate Reynolds number [39]. The drag model is quadratic in the translational velocity and it has the following dependence on the angle of attack

$$\mathbf{F}^\nu = \frac{1}{2} \rho_f l \left[C_D(0) \cos^2 \alpha + C_D(\pi/2) \sin^2 \alpha \right] \sqrt{v_{x'}^2 + v_{y'}^2} (v_{x'}, v_{y'}) , \quad (5.7)$$

where $C_D(0)$ and $C_D(\pi/2)$ are the drag coefficients at $\alpha = 0$ and $\alpha = \pi/2$, respectively. The model of the pressure contribution to the drag can be motivated theoretically by assuming that the local drag on the plate is proportional to the square of the local velocity component normal to the plate

$$d\mathbf{F}^\nu = \frac{1}{2} \rho_f C_D(\pi/2) |v_n| v_n (-\sin \theta, \cos \theta) dr , \quad (5.8)$$

where we write the drag components in the laboratory coordinate system and define v_n as the local velocity component normal to the face of plate, i.e., $v_n = v_{y'} + r \dot{\theta}$.

We use $-l/2 \leq r \leq l/2$ to denote the position of a plate segment relative to the center. In the absence of rotation we obtain the term used in equation (5.7) to model the pressure contribution to the drag

$$\mathbf{F}^\nu = \frac{1}{2} \rho_f C_D(\pi/2) l \sin^2 \alpha \sqrt{v_{x'}^2 + v_{y'}^2} (v_{x'}, v_{y'}) . \quad (5.9)$$

In the following we apply the local drag term (5.8) to describe the dissipative fluid torque

$$d\tau^\nu = \frac{1}{2} \rho_f C_D(\pi/2) |v_n| v_n r dr , \quad (5.10)$$

and by integration we obtain the dissipative torque model

$$\tau^\nu = \frac{1}{2} \rho_f C_D(\pi/2) \int_{-l/2}^{l/2} |v_n| v_n r dr . \quad (5.11)$$

The torque term vanishes for a purely translating plate, and in the absence of translation we can directly perform the integral: $\tau^\nu = (1/64) \rho_f C_D(\pi/2) l^4 |\dot{\theta}| \dot{\theta}$.

In section 5.5 we compare the dissipative torque with the experiment.

5.3 Circulation and Center of Mass Elevation

A falling leaf or paper, while falling downward on average, can rise momentarily as if picked up by wind. In Fig. 1.1 we verify this observation by filming a falling journal cover at high speed. The case shown in Fig. 5.4 is an example of center of mass elevation for a rigid plate without ambient wind. At sufficiently high Reynolds numbers, Joukowski's theory predicts phugoid motion which swings up periodically in the special case where the angle of attack is constant and drag is negligible [3]. The situation here is different. The Reynolds number is relatively low, about 10^3 ,

and drag is non-negligible. A straightforward modification of Joukowski's model to incorporate the lift-drag polar at Reynolds number about 10^3 predicts no center of mass elevation. Center of mass elevation can be related to the circulation around the falling plate, i.e. the quantity that, within inviscid theory, gives the lift on the plate.

In inviscid theory, the circulation Γ is unknown and needs to be modeled to complete the equations for the pressure force. Figure 5.5 shows the best fit of the pressure force from the Navier-Stokes solution of a tumbling ellipse by using equations (5.1-5.2) where the added mass coefficients are left as free parameters and Γ has two contributions, one proportional to the angular velocity of the ellipse Ω and the other given by the Kutta-Joukowski condition, as in equation 6.7.

For the falling ellipse shown in Fig. 5.4, the rotational contribution is about 10 times larger than the translational one. The lift corresponding to the circulation Γ is about 75% of the total lift, the remaining lift being generated by the added mass terms with coefficients m_{12} and m_{21} . It is worth noting that values m_{ij} from the force fit differ from those given by inviscid theory (see caption of Fig. 5.5). Skin friction gives a contribution of about 25% of the total force and can be approximated with an expansion in the kinematic variables the ellipse v_x , v_y , and $\dot{\theta}$ (see caption in Fig. 5.5).

The circulation model of equation (5.5) can be validated by integrating the velocity field outside the ellipse. Fig.5.6 shows the circulation obtained both by fitting the pressure force with equations (5.1-5.2) and by integrating the velocity field. The circulation displays a strong dependence on the motion of the ellipse and can not be modeled by a constant value as in [22] or by the classical expression for a translating airfoil as in [34, 7]. Instead, the circulation is better approximated by

equation (5.5). The negative peaks in the circulation correspond to vortices shed at the turning points of the ellipse trajectory.

In terms of the traditional decomposition of forces into lift and drag, the proportionality between the circulation around the ellipse and its rotational velocity corresponds to a lift proportional to $\Omega|\mathbf{v}|$ instead of $|\mathbf{v}|^2$ as in the case of a translating plate. In the classical context, $\Omega|\mathbf{v}|$ is the predicted lift for an airfoil translating and pitching at small amplitude [26]. This is particularly important at the turning points of the trajectory, where the translational velocity is small. There, the increased angular velocity Ω compensates for the decreasing translational velocity $|\mathbf{v}|$ and the lift generated is sufficient for the center of mass of the ellipse to elevate. This mechanism for lift augmentation has also been recently emphasized in insect hovering[9].

To further verify the connection between center of mass elevation and rotational lift, we arbitrarily vary the coefficients of the rotational and translational contributions in equation (5.5). The tumbling trajectories obtained with such a procedure are shown in Fig. 5.7. Models without rotational lift display center of mass elevation only for unphysical values of the lift coefficient ($c_L > 7$). On the other hand, models including rotational lift show center of mass elevation for the coefficients obtained from Navier-Stokes solutions ($c_L = 0.49$ and $c_R = 2.6$ in the case shown in Fig. 5.7). The comparison between the two trajectories obtained with and without rotational lift with the direct numerical simulation shown in figure 5.4 provides another qualitative validation of the circulation model of equation 5.5.

Finally the flow-induced coupling between translation and rotation can decrease the speed of descent. The tumbling ellipse shown in Fig. 5.4 has an average descent

speed of $0.4u_t$. In contrast, an identical ellipse parachuting down with its major axis perpendicular to the direction of motion would reach a terminal velocity of $0.77u_t$. It would be interesting to find out whether the slow descent and the stable direction of tumbling motion are exploited by nature, for example in seed dispersion.

5.4 Measured and quasi-steady fluid forces

Figure 5.8 shows the measured and the quasi-steady force vectors at different instances during tumbling and fluttering. The quasi-steady model describes the measured fluid forces well during most parts of the trajectories, but underestimates the fluid forces immediately after the 180° rotations following the short gliding segments at position (1) in figure 5.8(a). This is to be expected since the plate velocities are small and the wake effects are strong (see figure 4.8(h) for illustration of the wake structure).

Figure 5.9 shows the measured and the quasi-steady lift and drag as functions of time. We decompose the buoyancy corrected fluid force, \mathbf{F} , in lift and drag, $\mathbf{F} = \mathbf{L} + \mathbf{D}$, where we define the lift, \mathbf{L} , the drag, \mathbf{D} , and their magnitudes L and D as follows

$$\mathbf{L} = (\mathbf{e}_v \times \mathbf{F}) \times \mathbf{e}_v = L \mathbf{e}_z \times \mathbf{e}_v, \quad \mathbf{D} = (\mathbf{F} \cdot \mathbf{e}_v) \mathbf{e}_v = -D \mathbf{e}_v. \quad (5.12)$$

We let \mathbf{e}_v denote a unit vector in the direction of the center of mass velocity and \mathbf{e}_z a unit vector in the z -direction orthogonal to the plane of motion. Positive and negative values of D correspond to drag and thrust, respectively.

The quasi-steady model includes four lift terms, i.e., translational and rota-

tional lift as shown in equation (5.6) with coefficients C_T and C_R , respectively, and translational and rotational added mass terms. We use $C_T = 1.0$ in all four experimental cases and fit the measured lift to obtain the value of C_R . The procedure gives the lift coefficients summarized in table 5.1, and the quasi-steady lift plotted together with the measured lift in figures 5.8 and 5.9. In tumbling the translational lift alternates between pointing up and down with respect to the plate velocity as the plate pitches up at points marked (2), (3), and (5) and down at points marked (1) and (4) as shown in figure 5.8(a). The average vertical component of the translational lift is thus only 5 % of the buoyancy corrected gravity, and an unrealistically high translational lift coefficient of $C_T = 20$ would be required for the quasi-steady forces to balance the buoyancy corrected gravity if rotational lift were neglected. In tumbling the quality of the fit of the lift is therefore not very sensitive to the value of C_T , and with values of $C_T = 0.5$ and $C_T = 1.5$ we obtain similar values of C_R as with $C_T = 1.0$. For the fluttering plate shown in figure 5.8(b) the translational and rotational lift balance 30 % and 70 % of the buoyancy corrected gravity, respectively. We note that the lift contribution of added mass is small for both tumbling and fluttering in comparison with the measured lift as shown in figure 5.9.

The difference between the rotational and the translational lift is further illustrated in figure 5.10 which shows the translational and the rotational lift contributions together with the measured lift as functions of time. Figure 5.10(a) shows tumbling with $\beta = 1/5$ for which the functional form of the rotational lift resembles the functional form of the measured lift, whereas the translational lift has a markedly different functional form with approximately zero average. Figure 5.10(b) shows fluttering with $\beta = 1/14$ for which both the rotational and the

Table 5.1: Lift and drag coefficients in the quasi-steady model.

β	C_T	C_R	$C_D(0)$	$C_D(\pi/2)$
1/5	1.0	1.4	0.28	2.0
1/6	1.0	1.2	0.15	2.0
1/8	1.0	1.0	0.13	2.0
1/14	1.0	1.1	0.08	2.0

translational lift provide important contributions to the total lift and the functional forms are similar.

We model the drag using equation (5.7) with $C_D(\pi/2) = 2.0$ and $C_D(0)$ determined by the best possible fit to the measured drag. We expect that the drag model performs well during gliding at small angle of attack, see figure 5.8(b) positions (3) – (7), whereas we expect that it does not capture the wake dominated fluid forces at the turning points, see figure 5.8(b) positions (1) and (8). The values of $C_D(0)$ are in the range 0.1 – 0.3, and the value of $C_D(0)$ decreases with decreasing thickness to width ratio as expected. The quasi-steady model predicts added mass effects to overcome viscous drag and result in a net thrust at the turning points for the plates with $\beta = 1/5$, $\beta = 1/6$, and $\beta = 1/8$ as shown in figure 5.9. A net thrust is also observed experimentally with $\beta = 1/5$ and $\beta = 1/6$, but the magnitude is smaller. An estimate of the added mass coefficients based on the thrust peaks yields coefficients about 50 % smaller than the inviscid values.

5.5 Measured and quasi-steady fluid torque

Figure 5.11 shows the measured fluid torque (black) in comparison with the torque term, $(m_{11} - m_{22}) v_{x'} v_{y'}$, from ideal fluid theory (magenta), the torque term, $-I_a \ddot{\theta}$, related to the added moment of inertia (cyan), the torque from the translational lift acting halfway between the leading edge and the center of the plate (blue), the dissipative torque term (red), and the sum of the torque from translational lift and dissipation (green).

The ideal fluid torque $(m_{11} - m_{22}) v_{x'} v_{y'}$ is one to two orders of magnitude larger than the measured fluid torque, and the torque term $-I_a \ddot{\theta}$ is comparable in magnitude to the total measured fluid torque. The forces that produce the $(m_{11} - m_{22}) v_{x'} v_{y'}$ -term in ideal fluid theory do not give rise to a net fluid force on the plate, and it is therefore possible for the ideal fluid torque to be large although the forces due to added mass effects are small. In other words we observe that Kirchhoff's equations in the absence of circulation do not account for the measured lift and overestimate the fluid torque significantly.

The translational and the rotational lift give rise to fluid torque terms, but the values of l_τ are in general different for the two lift terms and theoretical values are only known in special cases, e.g., $l_\tau = 0$ for a plate with elliptical cross-section in an ideal fluid with constant circulation and $l_\tau = l/4$ for a translating wing at low angle of attack satisfying the Kutta condition. Figure 5.11 shows the torque from the translational lift with the assumption that the force acts halfway between the leading edge and the center of the plate, i.e., $l_\tau = l/4$ as in the case of a wing translating with constant and low angle of attack. The magnitude of the translational torque term is between two and four times larger than the magnitude of the measured fluid torque in the four experimental cases, and for fluttering the

translational torque term clearly overestimates the measured fluid torque. With the assumption that $l_r = l/4$ also for the rotational lift we overestimate the measured torque by one to two orders of magnitude. On the other hand the magnitude of the dissipative torque (5.11) with $C_D(\pi/2) = 2.0$ is comparable with the magnitude of the measured fluid torque in the four experimental cases, and the term provides a possible model of the dissipative part of the fluid torque.

5.6 Validity of the quasi-steady approximation

There are two main types of effects which are not accounted for in the quasi-steady approximation, i.e., unsteady corrections to specific force terms and effects due to the interaction of the plate with existing vortex structures. The first type of unsteady effects include development of lift during translational acceleration from rest at low angle of attack [36] and unsteady forces due to vortex formation at both leading and trailing edge during translational accelerating at high angle of attack [28]. An example of such unsteady effects is also shown in figure 5.2. The second type of effects can be significant when the quasi-steady approximation is applied to problems like flapping flight in which a wing is oscillated back and forth and moves into its own wake [9]. However, a freely falling plate does not interact with its own wake during gliding (see figures 4.8 and 4.9) and such effects are of little significance except at the turning points.

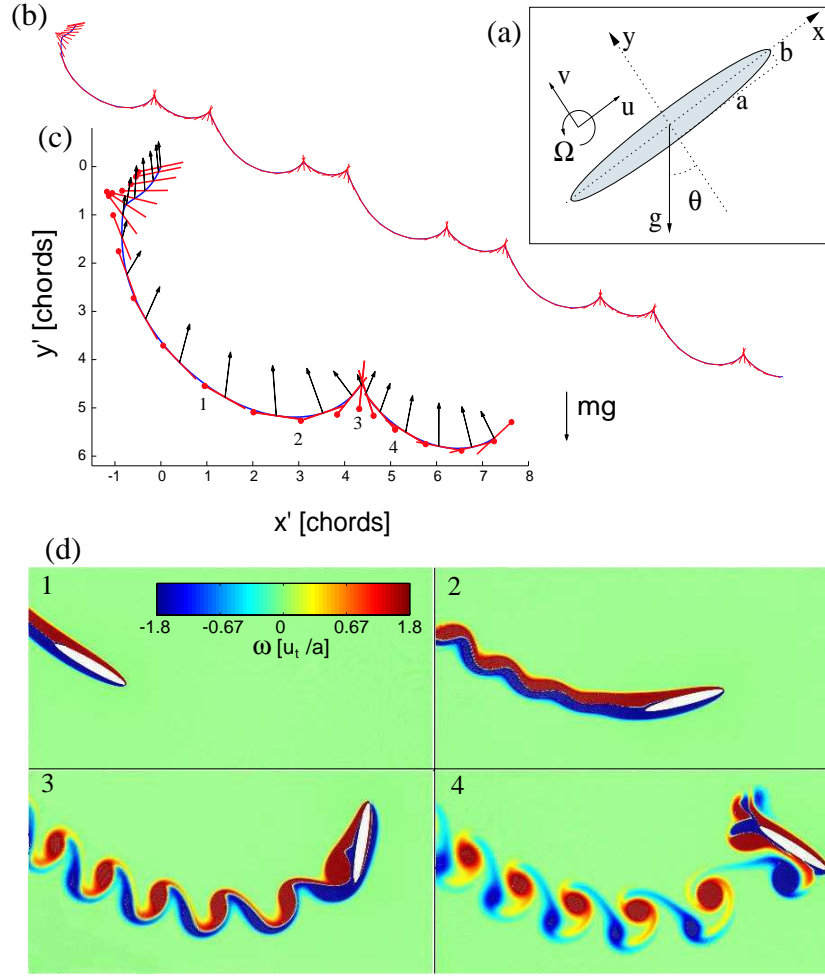


Figure 5.4: Navier-Stokes solution of a tumbling ellipse at $Re = 1100$, $I^* = 0.17$ and $e = 0.125$. (a) Body-fixed coordinate system and kinematic variables. (b) Trajectory and orientation of the chord (major axis of the ellipse) over five periods of motion. (c) the history of the chord (in red) and the force vector (in black), equally spaced in time for the first period of the trajectory in (b). The chords numbered from 1 to 4 correspond to the frames shown in (d) and to the times marked with dots on the force history of Fig. 5.5. (d) Vorticity field at four instants during a full rotation. The frames display an area of 5×2.5 chords and they are $4 a/u_t$ time units apart. The vorticity field is color coded on a logarithmic scale.

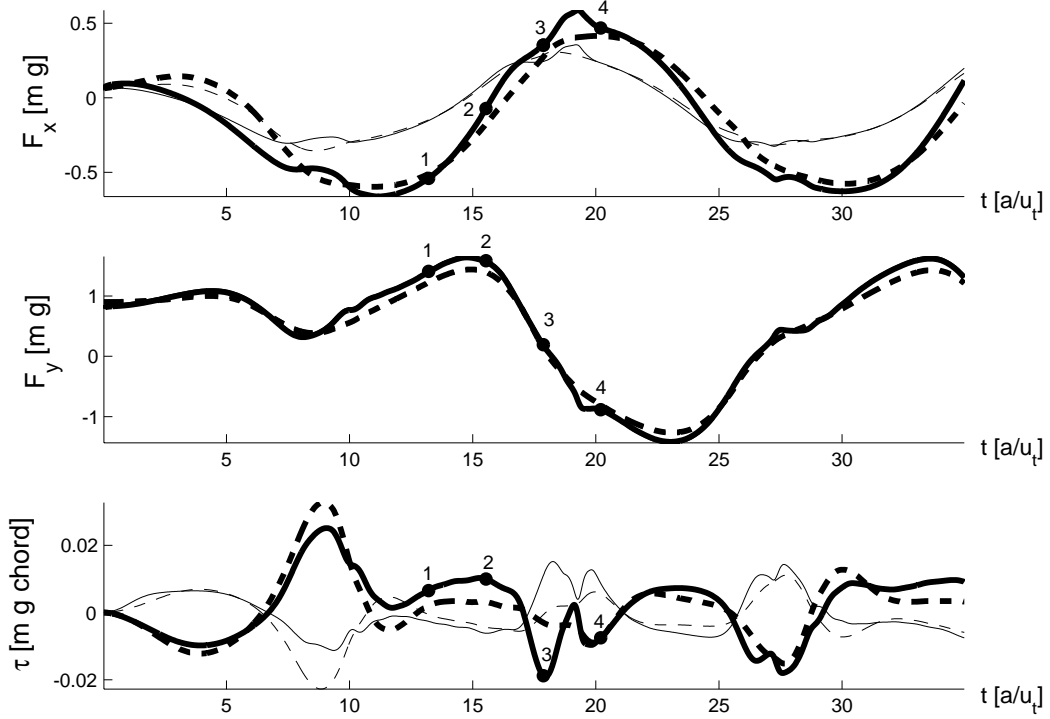


Figure 5.5: The fluid force and torque on the tumbling ellipse shown in Fig. 5.4. Solid lines are computed forces, with total force in red and the pressure force in blue. The corresponding dashed lines are the best fits of the data based on the quasi-steady model of equations (5.1-5.3). The added mass tensor $m_{11} = 0.53m$ and $m_{12} = 3.1m$, $m_{22} = 1.5m$, $m_{21} = 0.56m$ and the circulation around the ellipse $\Gamma = 2.6a^2\Omega + 0.49a|\mathbf{v}|\sin(2\alpha)$ are obtained from the pressure force. These m_{ij} differ from those predicted by inviscid theory ($m_{11}^{\text{inv}} = m_{21}^{\text{inv}} = 0.0491m$ and $m_{22}^{\text{inv}} = m_{12}^{\text{inv}} = 3.14m$) The viscous corrections are modeled with the expansions $F_x^\nu = -\nu_{11}u - \nu_{12}u^2$, $F_y^\nu = -\nu_{21}v - \nu_{22}v^2$ and $\tau^\nu = \nu_{31}uv - \nu_{32}\Omega - \nu_{33}\Omega|\Omega|$, with $\nu_{11} = 0.18$, $\nu_{12} = 0.0075$, $\nu_{21} = 0.070$, $\nu_{22} = 0.054$, $\nu_{31} = -0.31$, $\nu_{32} = -0.05$, and $\nu_{33} = 0.16$.

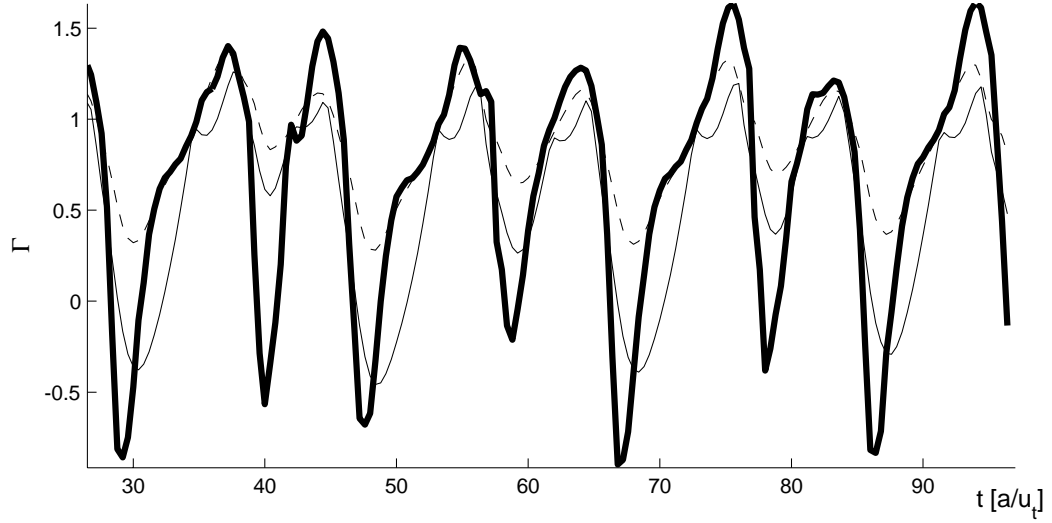


Figure 5.6: Circulation as a function of time for the falling ellipse of Fig. 5.4. In blue, the value of the circulation found integrating the vorticity field up to a radius of $3/2$ chords from the center of the ellipse. The dashed line corresponds to the circulation obtained from fitting the pressure forces, the red dashed line to the contribution of the rotational term of equation (5.5) alone. The peaks of negative circulation not captured by the fit correspond to the vortices shed by the ellipse at the turning points of its trajectory.

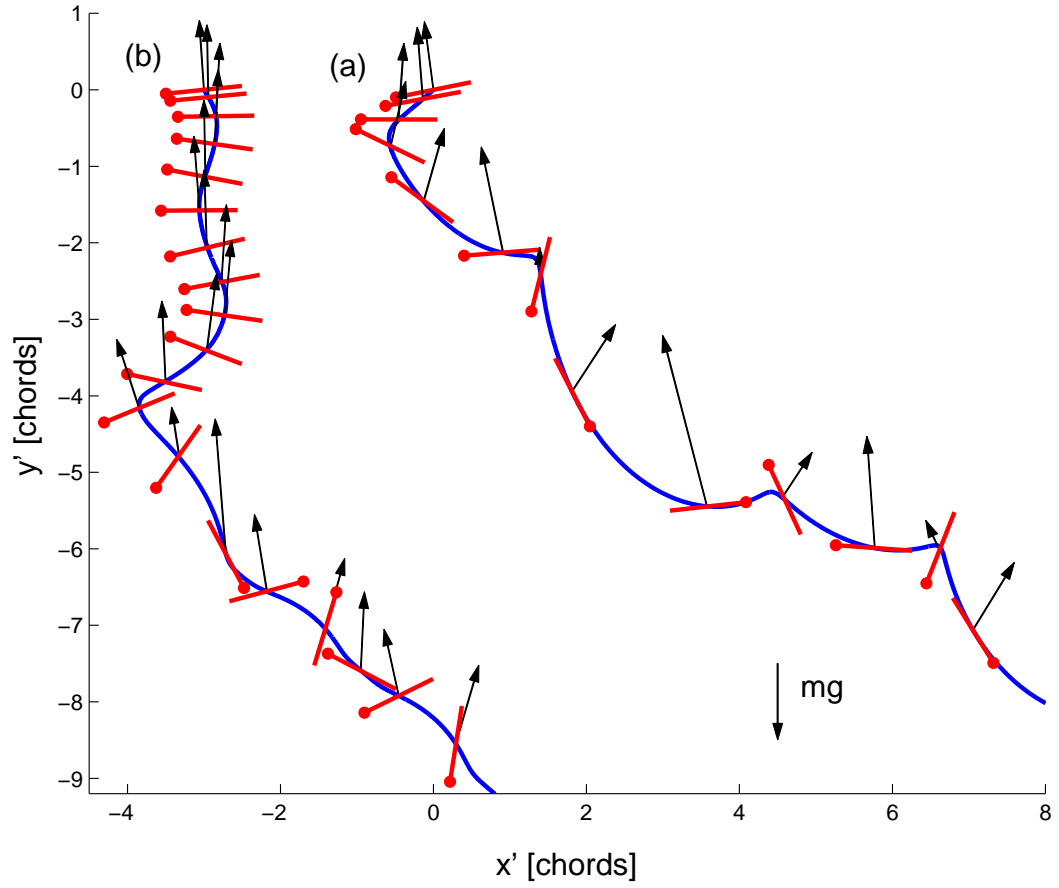


Figure 5.7: Trajectories obtained from ordinary differential equations (5.1-5.3) for different values of the translational and rotational lift coefficients c_L and c_R : a) $c_R = 2.6$, $c_L = 0.49$, from the fit of Fig. 5.5; b) $c_R = 0$, $c_L = 1.5$, as in classical translational lift. Center of mass elevation occurs in (a), but is absent in (b).

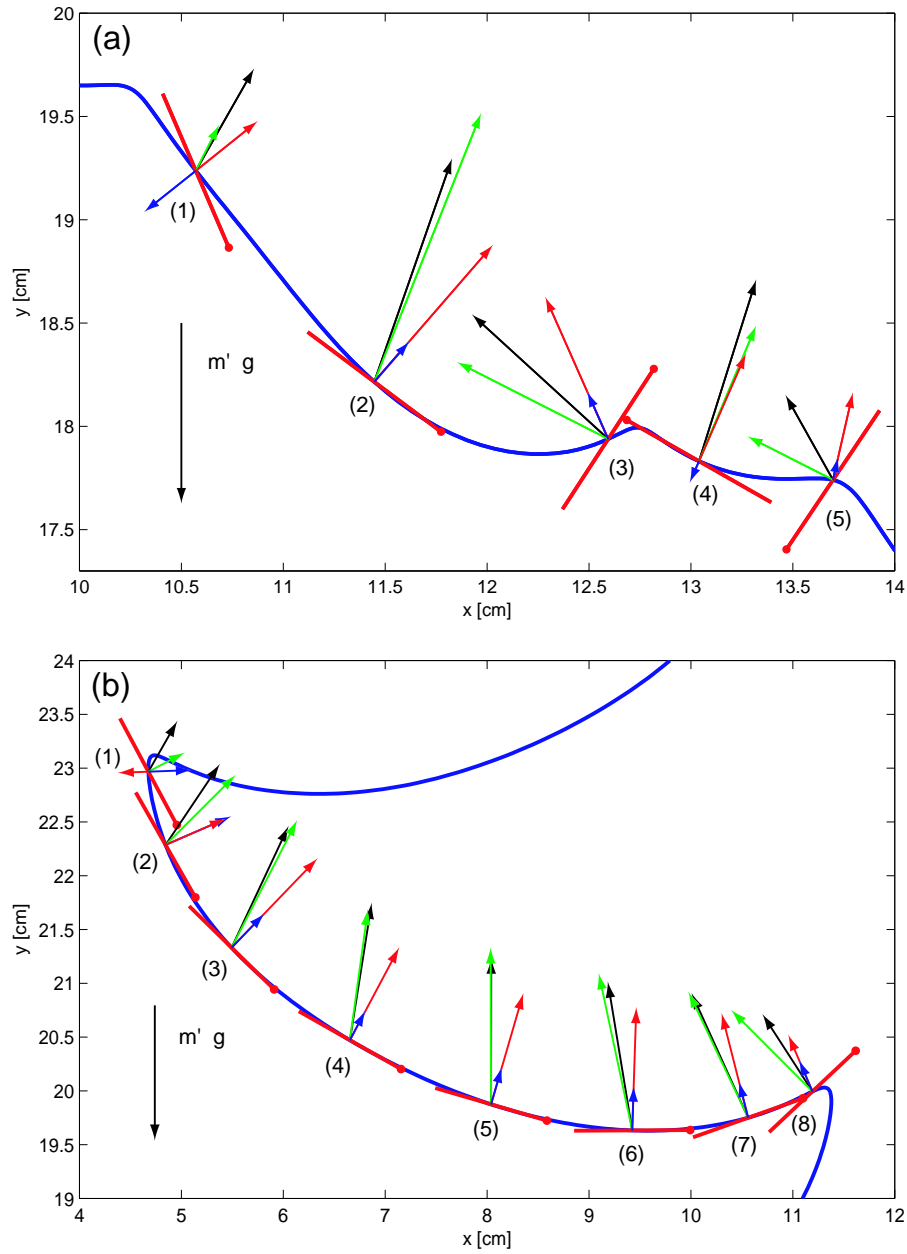


Figure 5.8: Measured fluid force (black), total quasi-steady force (green), translational lift (blue), and rotational lift (red). (a) tumbling plate with $\beta = 1/5$ and (b) fluttering plate with $\beta = 1/14$. In (a) the translational lift points down at (1) and (4) and up at (2), (3), and (5), and the quasi-steady model underestimates the fluid forces at (1) after the short gliding segments.

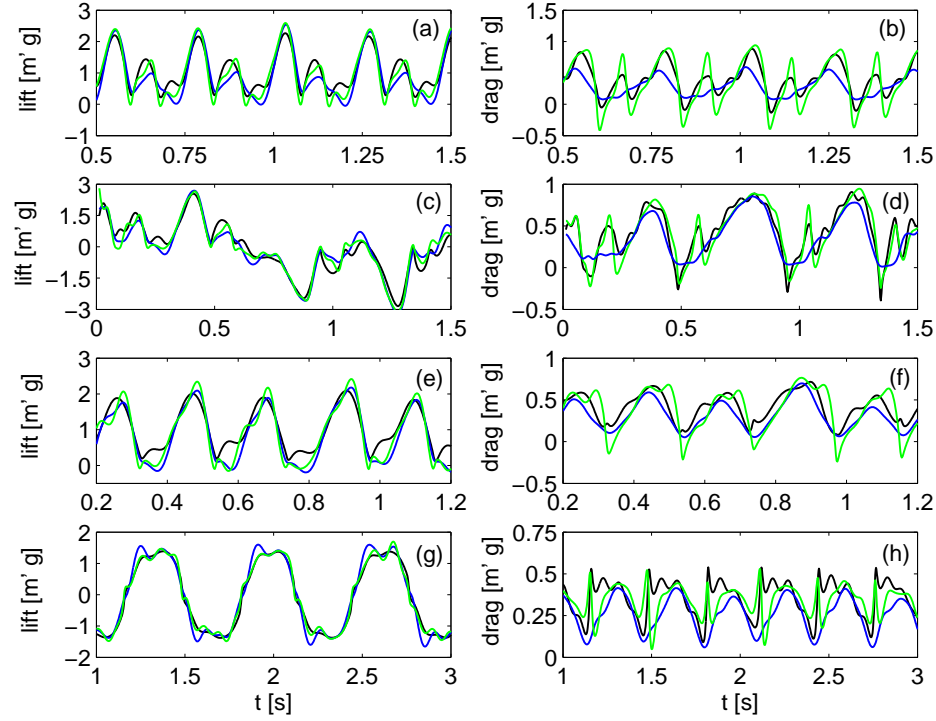


Figure 5.9: Lift and drag components of fluid forces. Measured forces (black), total quasi-steady forces (green), and quasi-steady forces without added mass (blue). (a) – (b) tumbling with $\beta = 1/5$, (c) – (d) apparently chaotic motion with $\beta = 1/6$, (e) – (f) tumbling with $\beta = 1/8$, and (g) – (h) fluttering with $\beta = 1/14$. Added mass effects give negligible contributions to the lift. The relative contributions to the drag are larger, but the resulting thrust peaks (negative drag) are not always observed experimentally as with $\beta = 1/8$. In (g) the sign of the lift defined in equation (5.12) depends on whether the plate moves left or right.

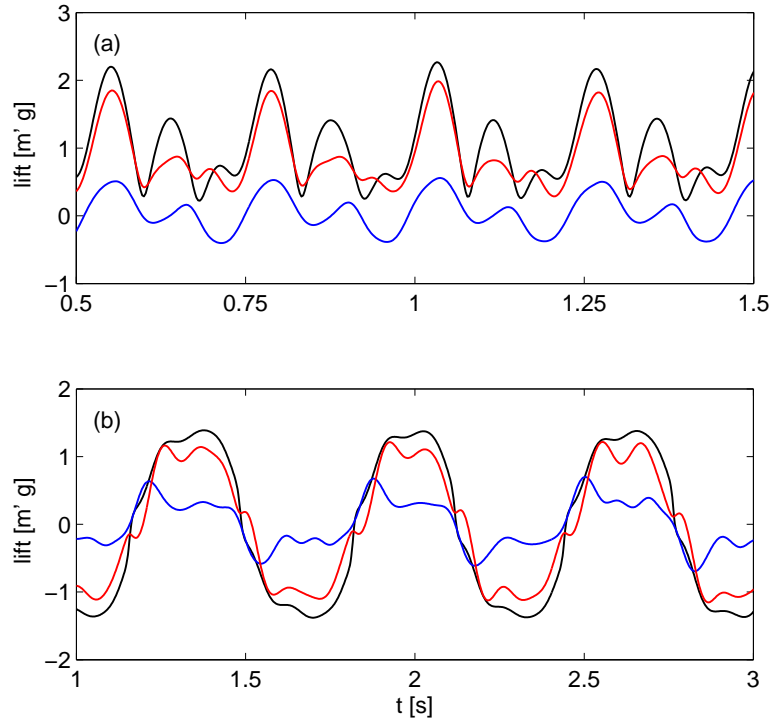


Figure 5.10: Measured (black), translational (blue), and rotational lift (red). (a) tumbling with $\beta = 1/5$ and (b) fluttering with $\beta = 1/14$. In (a) the average value of the translational lift is small and its functional form is markedly different from the measured lift, whereas the rotational lift captures the main features of the measurements. In (b) both the translational and the rotational lift have significant contributions to the total lift and the functional forms are similar.

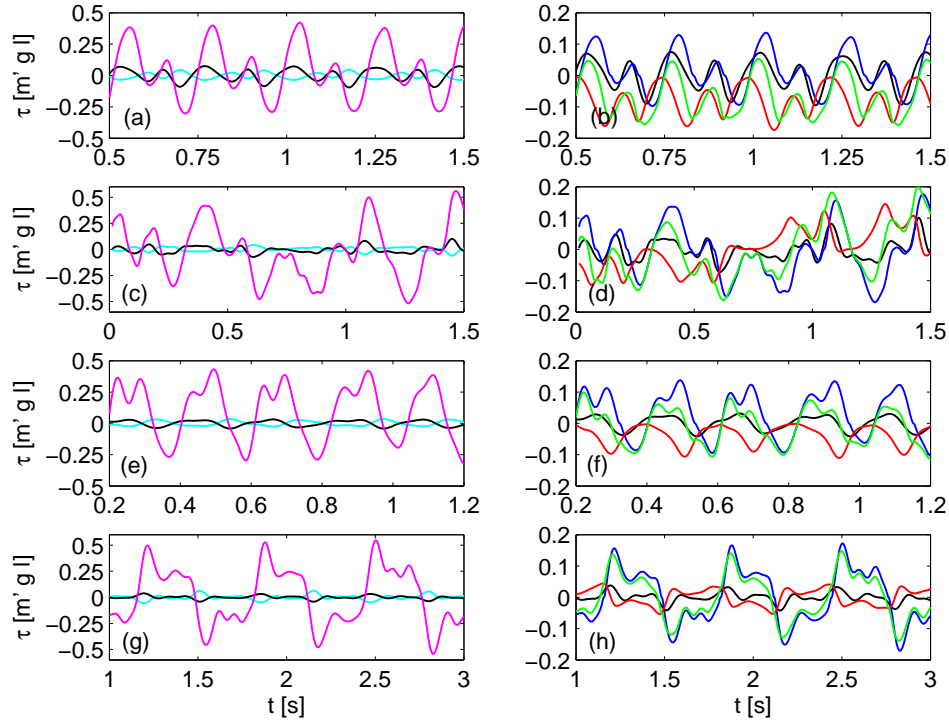


Figure 5.11: Measured torque and quasi-steady torque contributions. Measured torque (black), the term $(m_{11} - m_{22}) v_{x'} v_{y'}$ from ideal fluid theory (magenta), the term $-I_a \ddot{\theta}$ related to the added moment of inertia (cyan), the torque from translational lift (blue), the dissipative torque (red), and the sum of the torque from translational lift and dissipative effects (green). (a) – (b) tumbling with $\beta = 1/5$, (c) – (d) apparently chaotic motion with $\beta = 1/6$, (e) – (f) tumbling with $\beta = 1/8$, and (g) – (h) fluttering with $\beta = 1/14$.

Chapter 6

ODE Model Analysis and bifurcations

Despite that fluttering and tumbling bodies are common everyday phenomena that have interested scientists for centuries, see the qualitative discussion of tumbling by [24], it turns out that little is known theoretically about the nature of the transitions between fluttering, tumbling, and steady descent.

[41] measured a phase diagram for falling disks with fluttering, tumbling, and steady descent. Both the three-dimensional motion of a falling circular disk and the two-dimensional motion of a falling card depend on six dimensional quantities, i.e., the diameter or the width of the object, $2a$, the thickness of the object, $2b$, the density of the object, ρ_s , the density of the fluid, ρ_f , the kinematic viscosity of the fluid, ν , and the acceleration due to gravity, g . From the six dimensional quantities it is possible to form three non-dimensional numbers. The phase diagram was constructed using the ratio between the thickness and the diameter of the disk, β , the dimensionless moment of inertia, I^* , and the Reynolds number, Re . The experiment focused on the small β limit in which the dynamics is independent of β and the phase diagram depends on Re and I^* alone. The disks fall steadily and broadside on for Re below 100, and for larger values of Re they flutter when I^* is small and tumble when I^* is large. [13] made further experiments on falling disks and found a chaotic transition region between fluttering and tumbling, [33] measured a qualitatively similar phase diagram for falling plates, and [7] studied the transition from fluttering to tumbling with increasing I^* in a quasi two-dimensional experiment with a narrow container in which the plate motion was constrained mechanically to be two-dimensional. Here we measure the

trajectories of fluttering and tumbling plates using a quasi two-dimensional setup and obtained the instantaneous fluid forces from the measured accelerations. In the experiment the plates were released in a water tank and allowed to fall freely without any constraints on their motion. The plate length was much longer than the width and the thickness of the plates, and the plates were released so that they rotated about their long axis. Three-dimensional effects at the tips were therefore negligible in the experiment, and the motion was effectively two-dimensional.

In this chapter we describe the phase diagram and the transitions using direct numerical simulations of the two-dimensional Navier-Stokes equation and a fluid force model based on ordinary differential equations derived from the direct numerical simulations and experiments discussed in the previous chapters. By increasing the thickness to width ratio and thereby the reduced moment of inertia we find a transition between periodic fluttering and periodic tumbling. We observe a wide transition region with periodic motion in the direct numerical simulations and compare the findings with the apparently chaotic trajectories observed in the quasi two-dimensional experiment on falling plates by [1] and the chaotic transition region found in the three-dimensional experiments on falling disks by [41] and [13].

We show that the model introduced in chapter 5 depends naturally on the three non-dimensional parameters suggested by [41]. The model has two different steady solutions in which the card falls edge on and broadside on, respectively. The edge on fixed point is always unstable, whereas we find a transition between steady broadside on descent and oscillatory motion via a supercritical Hopf bifurcation in which the broadside on fixed point changes stability. We further analyze the transition between fluttering and tumbling in the fluid force model and show that the transition is a heteroclinic bifurcation which leads to a logarithmic divergence

of the period of oscillation at the bifurcation point. We conclude with a comparison of the bifurcation scenarios of the fluid force model and the direct numerical simulations.

6.1 Solutions in transition range between fluttering and tumbling

Figure 6.1 shows a family of trajectories with different thickness to width ratio, which range from periodic fluttering with $\beta = 1/18$ in figure 6.1(a) to periodic tumbling with $\beta = 1/8$ in figure 6.1(d). The density ratio was $\rho_s/\rho_f = 2.05$ in the simulations and the Reynolds number based on the semi-major axis and the average descent speed was between 400 and 600. The trajectories in figures 6.1(a) and 6.1(d) are similar to the periodic trajectories measured by [1] and alternate between gliding at low angle of attack and fast rotational motion at the turning points. In the parameter range between periodic fluttering and periodic tumbling we observe a transition region with either asymmetric fluttering, as shown in figure 6.1(b), or solutions in which the plate flutters in an apparently periodic fashion but tumbles once between consecutive turning points as shown in figure 6.1(c).

A characteristic feature of the dynamics in the transition region is that the plates fall vertically and edge on for long distances as shown for $\beta = 1/12$ in figure 6.1(c). The time spent during the vertical edge on descent is much longer than the time spent during gliding in periodic fluttering and periodic tumbling outside the transition region as shown in figures 6.1(a) and 6.1(d). The length of the vertical descent and therefore the period of oscillation diverges in the transition region. The periods of oscillation are reported in non-dimensional form in the caption

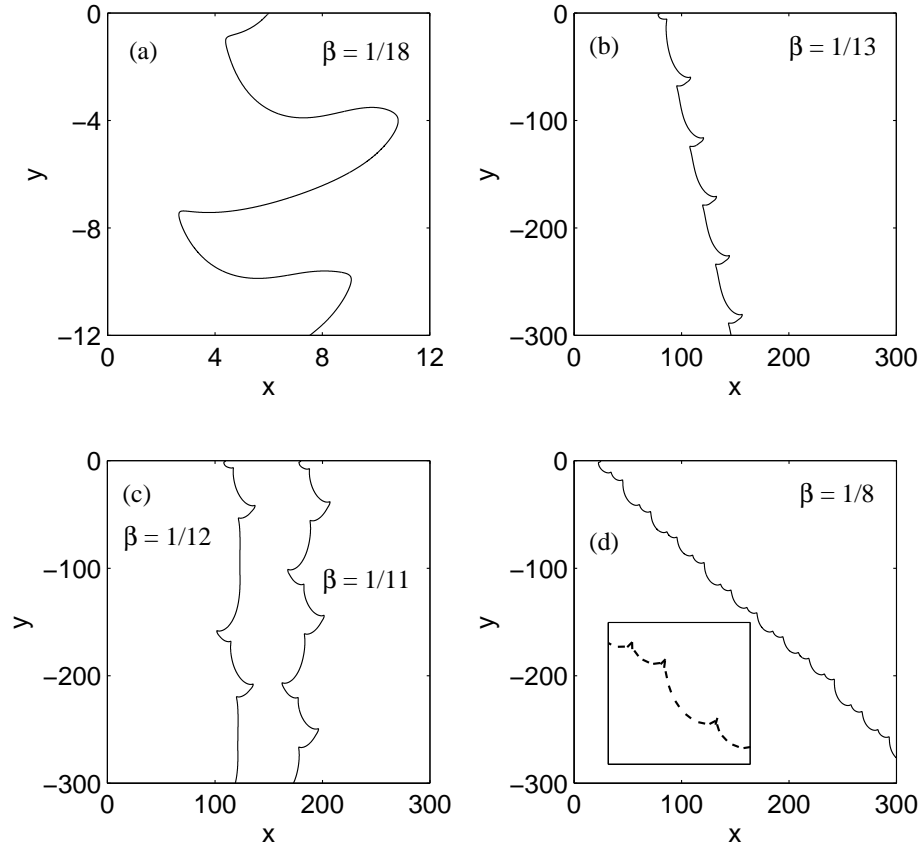


Figure 6.1: Trajectories obtained from direct numerical simulations of the two-dimensional Navier-Stokes equation around freely falling plates in the transition range between fluttering and tumbling. (a) periodic fluttering with the non-dimensional period of oscillation $T = 8.1$, (b) fluttering close to the transition between fluttering and tumbling with $T = 17.3$, (c) mixture of fluttering and tumbling with $T = 34.1$ for $\beta = 1/11$ and $T = 43.4$ for $\beta = 1/12$, and (d) periodic tumbling with $T = 12.1$. The semi-major axes of the plates have unit length in the four plots, and the periods of oscillation are made non-dimensional as described in § 6.4.

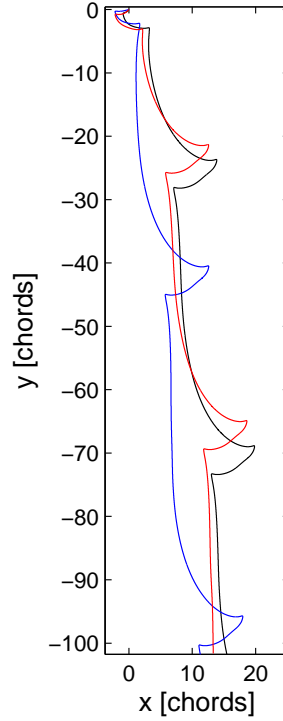


Figure 6.2: Dependence on initial conditions of falling ellipses in the transition between fluttering and tumbling ($\beta = 1/12.75$). The initial conditions for the trajectories in black, blue and red are respectively $(\theta, v_x, v_y, \omega)$: $(0.2, 0, 0, 0)$, $(0.2, 6.76, 3.38, 0)$ and $(0.2, 0, 0, 0.68)$.

of figure 6.1 for comparison with the results of the non-dimensional quasi-steady model in § 6.6.2. We find that the period of oscillation increases by a factor of 5 in the transition region relative to the period of oscillation for fluttering and tumbling outside the transition region, but due to the large computational cost in the transition region and the dependence of the trajectories on initial conditions (see figure 6) we have not been able to determine the precise functional form of the divergence based on our direct numerical simulations.

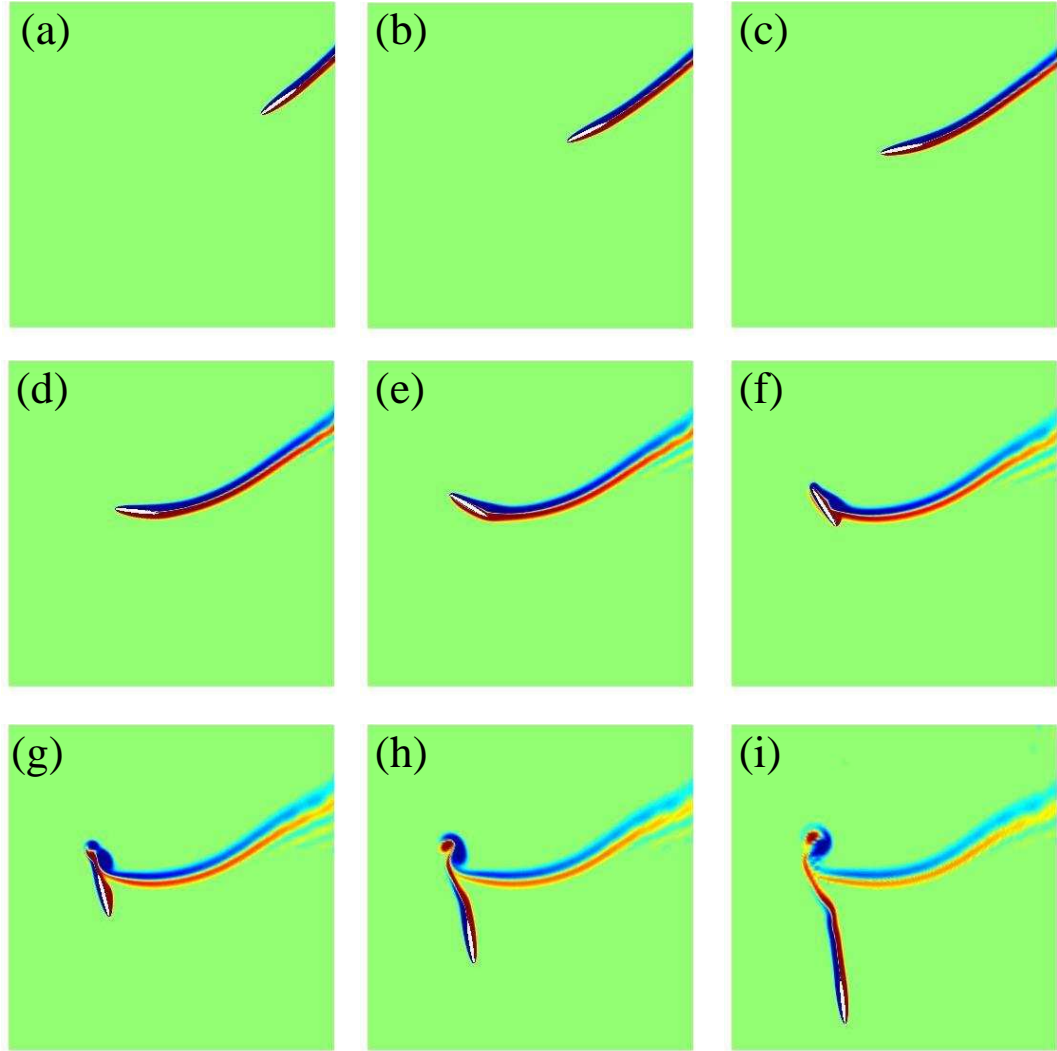


Figure 6.3: Vorticity field around an ellipse in the transition region ($\beta = 1/12$).

6.2 Direct numerical solutions versus previous experiments

The presence of a transition region between periodic fluttering and periodic tumbling is in agreement with the quasi two-dimensional experiment on falling plates by [1], but in disagreement with the quasi two-dimensional experiment by [7] in which a sharp transition is found. We speculate that the sharp transition observed by [7] arises because the quasi two-dimensional flow is established using a narrow flow tank in which the falling plates touch the container walls in order to constrain their motion to be two-dimensional. Another qualitative difference between the experiment by [7] and the experiment by [1] is related to center of mass elevation. The trajectories reported by [7] do not display center of mass elevation, whereas we find numerically [27] and experimentally [1] that the center of mass elevates at the turning points in fluttering and tumbling. The absence of center of mass elevation in the experiment by [7] could be due to friction between the plates and the container walls. In the experiment by [1] such additional damping is not present, since the plates fall without touching the container walls.

The direct numerical simulations show that the transition between periodic fluttering and periodic tumbling does not always take place through a sequence of apparently chaotic states like the trajectories observed in the quasi two-dimensional experiment by [1] and in the three-dimensional experiments on circular disks by [41] and [13]. The results of the direct numerical simulations could suggest that apparently chaotic trajectories are found experimentally because the dynamics in the transition range is very sensitive to experimental noise. However, it could also be that the transition between fluttering and tumbling in some cases, e.g., at higher values of the Reynolds number, takes place through a sequence of chaotic solutions.

6.3 Phenomenological model of a falling card

To gain further insight into the nature of the transition between fluttering and tumbling we consider the phenomenological model of the card aerodynamics based on ordinary differential equations introduced in chapter 5. We aim to identify the bifurcation between fluttering and tumbling in the ODE model and to quantify the divergence of the period of oscillation at the transition point.

The Reynolds number enters the model implicitly through the values of the non-dimensional coefficients C_T , C_R , A , B , μ_1 , and μ_2 . In the following we shall use lift and drag coefficients from the literature [39], whereas we will fix the coefficients for the dissipative torque so that the time-scale for the oscillatory motion is correct and leads to qualitatively correct solutions with periodic fluttering and periodic tumbling. We conjecture that out of the six non-dimensional coefficients the two dissipative torque coefficients depend most sensitively on the Reynolds number, and that μ_1 and μ_2 increase with decreasing Reynolds number corresponding to an increase in the damping of the oscillatory motion with decreasing Reynolds number.

6.4 Non-dimensional equations

We write the governing equations (5.1) – (5.3) in dimensionless form using the length scale, L , and the velocity scale, U , which we define by the expressions

$$L = a, \quad U = \sqrt{(\rho_s/\rho_f - 1) g b}. \quad (6.1)$$

The average terminal velocity, U , is estimated by balancing gravity with a quadratic drag. Three non-dimensional parameters can be constructed from the six dimen-

sional quantities describing a free falling card. We follow [41] and apply the thickness to width ratio, $\beta = b/a$, the dimensionless moment of inertia

$$I^* = \frac{\rho_s b}{\rho_f a} , \quad (6.2)$$

and the Reynolds number based on the semi-major axis and the terminal velocity

$$\text{Re} = \frac{a U}{\nu} . \quad (6.3)$$

Using the characteristic scales and the three non-dimensional numbers we obtain the following non-dimensional governing equations

$$(I^* + \beta^2) \dot{v}_{x'} = (I^* + 1) \dot{\theta} v_{y'} - \Gamma v_{y'} - \sin \theta - F_{x'}^\nu , \quad (6.4)$$

$$(I^* + 1) \dot{v}_{y'} = -(I^* + \beta^2) \dot{\theta} v_{x'} + \Gamma v_{x'} - \cos \theta - F_{y'}^\nu , \quad (6.5)$$

$$\frac{1}{4} \left[I^* (1 + \beta^2) + \frac{1}{2} (1 - \beta^2)^2 \right] \ddot{\theta} = (\beta^2 - 1) v_{x'} v_{y'} - \tau^\nu , \quad (6.6)$$

where we differentiate with respect to the non-dimensional time and use $v_{x'}$, $v_{y'}$, Γ , \mathbf{F}^ν , and τ^ν to denote the non-dimensional quantities. We apply the lift and the drag (5.6) – (5.11) which are valid in the intermediate to high Re range and for which the coefficients depend implicitly on Re . In non-dimensional form we have

$$\Gamma = \frac{2}{\pi} \left[-C_T \frac{v_{x'} v_{y'}}{\sqrt{v_{x'}^2 + v_{y'}^2}} + C_R \dot{\theta} \right] , \quad (6.7)$$

$$\mathbf{F}^\nu = \frac{1}{\pi} \left[A - B \frac{v_{x'}^2 - v_{y'}^2}{v_{x'}^2 + v_{y'}^2} \right] \sqrt{v_{x'}^2 + v_{y'}^2} (v_{x'}, v_{y'}) , \quad (6.8)$$

$$\tau^\nu = \left[\mu_1 + \mu_2 |\dot{\theta}| \right] \dot{\theta} . \quad (6.9)$$

In the following we investigate the dependence on the non-dimensional parameters and solve the equations numerically in the range of small thickness to width ratio.

6.5 Numerical solutions with small thickness to width ratio

6.5.1 Small thickness to width ratio

In the limit of small thickness to width ratio, $\beta \ll 1$, equations (6.4) – (6.6) reduce to

$$I^* \dot{v}_{x'} = (I^* + 1) \dot{\theta} v_{y'} - \Gamma v_{y'} - \sin \theta - F_{x'}^\nu, \quad (6.10)$$

$$(I^* + 1) \dot{v}_{y'} = -I^* \dot{\theta} v_{x'} + \Gamma v_{x'} - \cos \theta - F_{y'}^\nu, \quad (6.11)$$

$$\frac{1}{4} \left(I^* + \frac{1}{2} \right) \ddot{\theta} = -v_{x'} v_{y'} - \tau^\nu. \quad (6.12)$$

In this limit the model depends on Re and I^* alone in agreement with the phase diagrams measured by [41], [33], and [13]. The equations do not depend on the density ratio, but explicitly on the non-dimensional moment of inertia defined in equation (6.2).

6.5.2 Numerical solutions of the ODE model

Figure 6.4 shows numerical solutions of equations (6.10) – (6.12) supplemented by the terms (6.7) – (6.9) with $C_T = 1.2$, $C_R = \pi$, $A = 1.4$, and $B = 1.0$, see [39]. For the dissipative torque we set $\mu_1 = \mu_2 = 0.2$, which determines the time-scale for the oscillations relative to the time-scale characterizing the vertical descent and leads to solutions with periodic fluttering and periodic tumbling in

qualitative agreement with the direct numerical solutions shown in figure 6.1.

Figure 6.4 shows periodic fluttering for $I^* = 1.1$, period-one tumbling for $I^* = 1.4$, period-two tumbling for $I^* = 1.45$, periodic mixture of fluttering and tumbling for $I^* = 1.6$, chaotic dynamics for $I^* = 2.2$, and small amplitude broadside on fluttering for $I^* = 3.0$. As expected from the phase diagram measured by [41] and the study by [7] we observe a transition from fluttering to tumbling with increasing I^* as shown in figures 6.4(a) and 6.4(b). The periodic solutions are independent of the initial conditions and follow after short transients. The fluttering with $I^* = 1.1$ and the tumbling with $I^* = 1.4$ alternate between gliding at low angle of attack and fast rotational motion and center of mass elevation at the turning points in agreement with the direct numerical simulations and the experiment discussed in chapter 4. We find a period-doubling bifurcation between $I^* = 1.4$ and $I^* = 1.45$, and we note that the typical tumbling motion has a period-two structure as illustrated by the direct numerical solution shown in figure 6.1(d).

With $I^* = 1.6$ we find a periodic solution in which the card displays a mixture of fluttering and tumbling, and with $I^* = 2.2$ we find a chaotic solution with a maximum Lyapunov exponent of $\lambda_{max} = 0.13 \pm 0.01$. Chaotic solutions, for which the solution with $I^* = 2.2$ is a typical example, are found with $\mu_1 = \mu_2 = 0.2$ and I^* in the range between 1.8 and 2.8 as shown in figure 6.6(b). The card in figure 6.4(f) oscillates about the broadside on fixed point. The broadside on fixed point becomes stable and the oscillations are damped out if the dissipative torque is increased and the characteristic dissipative time-scale for the decay of angular momentum is decreased. In the following we describe this bifurcation and the bifurcation between fluttering and tumbling.

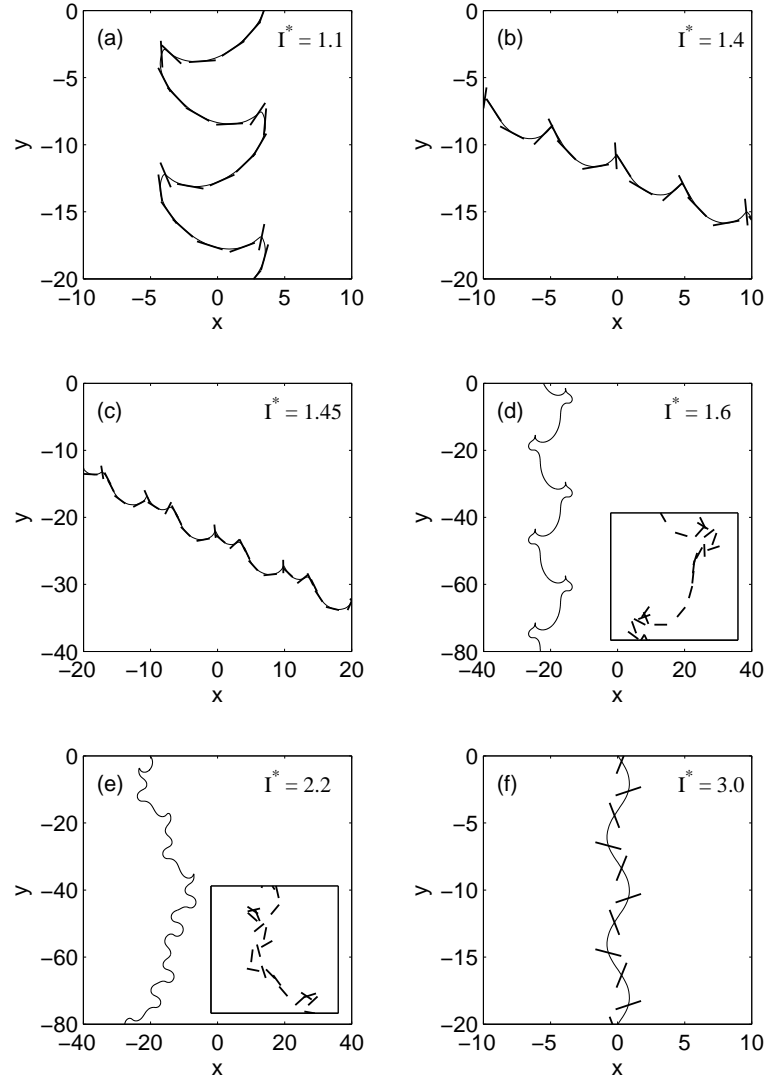


Figure 6.4: Numerical solutions of the non-dimensional equations (6.10) – (6.12) showing the card trajectories. (a) periodic fluttering for $I^* = 1.1$, (b) period-one tumbling for $I^* = 1.4$, (c) period-two tumbling for $I^* = 1.45$, (d) periodic mixture of fluttering and tumbling for $I^* = 1.6$, (e) chaotic dynamics for $I^* = 2.2$, and (f) small amplitude broadside on fluttering for $I^* = 3.0$.

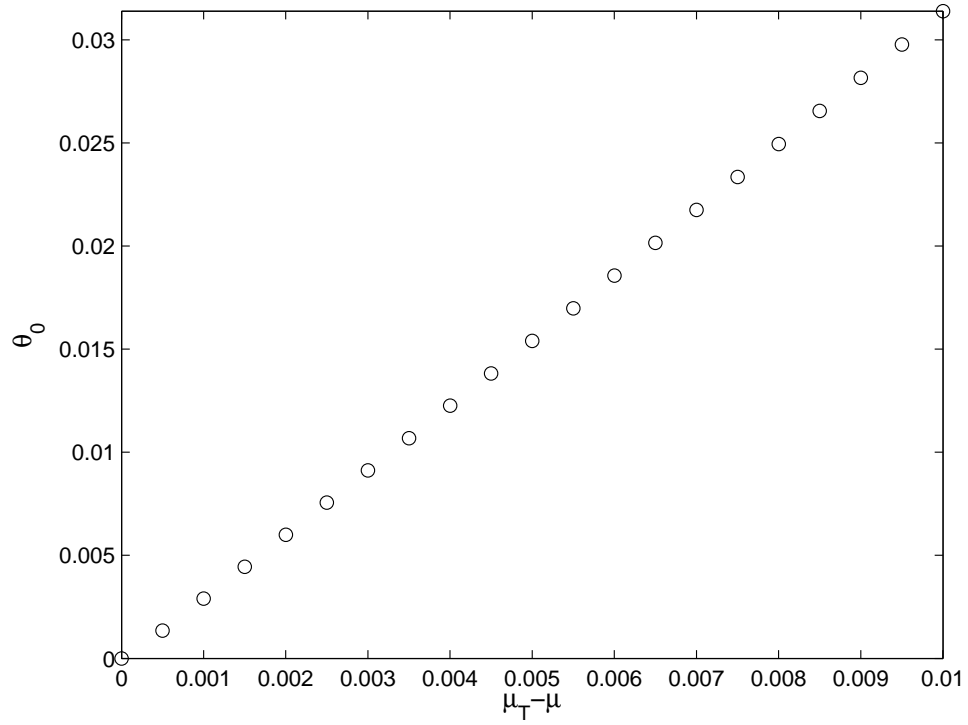


Figure 6.5: Amplitude of oscillation for $I^* = 3$ as a function of $\mu_T - \mu$, where $\mu = \mu_1 = \mu_2$ and $m\mu_T$ is the critical value of μ , obtained by solving the ODE system 5.1-5.3 numerically. The size of the oscillation grows continuously from zero, indicating that the Hopf bifurcation between steady descent and oscillatory motion is supercritical.

6.6 Fixed points and bifurcations

6.6.1 Transition between steady descent and oscillatory motion

The differential equations have four steady solutions in which the card falls vertically and gravity is balanced by drag, i.e., two fixed points for which the card falls edge on:

$$\begin{bmatrix} v_{x'} \\ v_{y'} \\ \theta \\ \dot{\theta} \end{bmatrix} = \begin{bmatrix} \mp \sqrt{\frac{\pi}{A-B}} \\ 0 \\ \frac{\pi}{2}, \frac{3\pi}{2} \\ 0 \end{bmatrix} = \begin{bmatrix} \mp V \\ 0 \\ \frac{\pi}{2}, \frac{3\pi}{2} \\ 0 \end{bmatrix} \quad (6.13)$$

and two fixed points for which the face of the card is normal to the direction of motion:

$$\begin{bmatrix} v_{x'} \\ v_{y'} \\ \theta \\ \dot{\theta} \end{bmatrix} = \begin{bmatrix} 0 \\ \mp \sqrt{\frac{\pi}{A+B}} \\ 0, \pi \\ 0 \end{bmatrix} = \begin{bmatrix} 0 \\ \mp W \\ 0, \pi \\ 0 \end{bmatrix} \quad (6.14)$$

Figure 6.6(a) illustrates the edge on and the broadside on steady solutions. We use V and W to denote the edge on descent speed and the broadside on descent speed, respectively.

The linearized equations in the neighborhood of the edge on fixed point ($\theta = \pi/2$) are

$$I^* \ddot{\tilde{v}}_{x'} = -\frac{2}{V} \tilde{v}_{x'} \quad (6.15)$$

$$(I^* + 1)\dot{\tilde{v}}_{y'} = V \left(I^* - \frac{2C_R}{\pi} \right) \tilde{\omega} + \tilde{\theta} - \left(\frac{2VC_T}{\pi} + \frac{1}{V} \right) \tilde{v}_{y'} \quad (6.16)$$

$$\dot{\tilde{\theta}} = \tilde{\omega} \quad (6.17)$$

$$\frac{1}{4} \left(I^* + \frac{1}{2} \right) \dot{\tilde{\omega}} = V \tilde{v}_{y'} - \mu_1 \tilde{\omega} \quad (6.18)$$

where we define $\omega = \dot{\theta}$ and use a tilde to denote the perturbation of the steady solution. We similarly linearize the equations in the neighborhood of the broadside on fixed point with $\theta = 0$ and write them as a system of coupled 1st order equations

$$I^* \dot{\tilde{v}}_{x'} = -W \left(I^* + 1 - \frac{2C_R}{\pi} \right) \tilde{\omega} - \tilde{\theta} + \left(\frac{2WC_T}{\pi} - \frac{1}{W} \right) \tilde{v}_{x'} \quad (6.19)$$

$$(I^* + 1)\dot{\tilde{v}}_{y'} = -\frac{2}{W} \tilde{v}_{y'} \quad (6.20)$$

$$\dot{\tilde{\theta}} = \tilde{\omega} \quad (6.21)$$

$$\frac{1}{4} \left(I^* + \frac{1}{2} \right) \dot{\tilde{\omega}} = W \tilde{v}_{x'} - \mu_1 \tilde{\omega} \quad (6.22)$$

In the following we obtain the phase diagram for the system (6.10) – (6.12) in the I^* versus μ_1 plane and show that the transition between steady descent and oscillatory motion and the transition between fluttering and tumbling are related to the fixed points. Figure 6.6(b) shows the phase diagram in the I^* versus μ_1 plane with fluttering, tumbling, and steady broadside on descent as we vary I^* , μ_1 , and μ_2 while keeping $\mu_1 = \mu_2$ and C_T , C_R , A , and B fixed. The transition between steady broadside on descent and oscillatory motion takes place as the broadside on fixed point goes from being stable to being unstable via a Hopf bifurcation. Equation 6.20 is decoupled from the three other equations and the direction is stable. The equation for the eigenvalues, λ , for the three linearly coupled modes follows from equations 6.19, 6.21, 6.22. With $C_T = 1.2$, $C_R = \pi$, $A = 1.4$, and $B = 1.0$ we find

$$3I^*(2I^* + 1)\lambda^3 + 24I^*\mu_1\lambda^2 + 10(I^* - 1)\pi\lambda + 4\sqrt{15\pi} = 0 \quad (6.23)$$

In the transition region the cubic equations has one negative real root and a pair of complex conjugate roots. The real part of the complex conjugate roots is negative in the stable region and positive in the unstable region, and the two roots are purely imaginary along the bifurcation curve:

$$\mu_1 = \frac{1}{4} \sqrt{\frac{3}{5\pi}} \frac{2I^* + 1}{I^* - 1} . \quad (6.24)$$

The solid line in figure 6.6(b) shows the bifurcation curve which separates solutions with steady broadside on descent and solutions with oscillatory motion. We find numerically that the size of the limit cycle grows continuously from zero (see figure 6.5) and that the oscillation frequency in the neighborhood of the bifurcation curve is equal to the absolute value of the imaginary parts of the complex conjugate eigenvalues along the bifurcation curve. These numerical results indicate that the Hopf bifurcation is supercritical.

The edge on fixed point is unstable for all values of I^* and μ_1 since the $v_{x'}v_{y'}$ -term in equation (6.12) acts to rotate the card in the same direction as any small perturbation away from the edge on orientation. For the broadside on fixed point the $v_{x'}v_{y'}$ -term instead acts in the opposite direction to any small perturbation away from the broadside on orientation and the fixed point is stable if I^* and μ_1 are sufficiently large.

6.6.2 Transition between fluttering and tumbling

The transition from fluttering to tumbling with increasing I^* and constant μ_1 and μ_2 shown in figures 6.4(a) and 6.4(b) is a heteroclinic bifurcation. The critical value of I^* increases when the dissipative torque is increased as shown in the inset of figure 6.6(b). Figure 6.8(a) shows numerical solutions of equations (6.10)

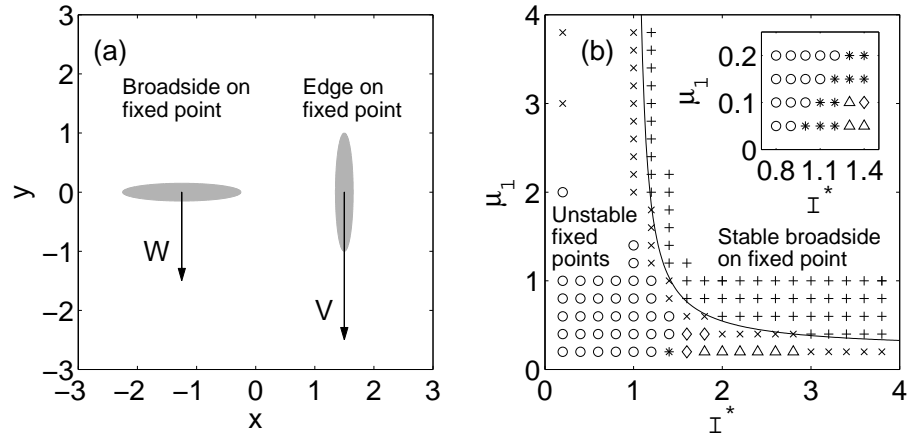


Figure 6.6: (a) fixed points and descent velocities and (b) phase diagram in the I^* versus μ_1 plane with the inset showing a magnification of the transition region between periodic fluttering and periodic tumbling. Numerical solutions of equations (6.10) – (6.12) and stability boundary for the broadside on fixed point (solid curve). Periodic fluttering (circles), steady broadside on descent (plus signs), periodic broadside on fluttering (crosses), periodic tumbling (stars), periodic mixture of fluttering and tumbling (diamonds), and chaos (triangles).

– (6.12) in the vicinity of the bifurcation point $I_C^* \approx 1.2191$. The cards fall edge on and accelerate downward for approximately 25 card widths, and when the cards reach the maximum descent speed they flutter for $I^* = 1.2190$ and tumble for $I^* = 1.2192$. Figure 6.8(b) shows the phase space trajectory for fluttering projected onto the three-dimensional space spanned by $v_{y'}$, θ , and ω , where we use the definition $\omega \equiv \dot{\theta}$. The trajectory spirals in toward one of the edge on fixed points, moves away on the unstable manifold, and follows the heteroclinic orbit to the other edge on fixed point. Figure 6.8(c) shows the phase space trajectory in the neighborhood of the edge on fixed point. The linearized equation for $v_{x'}$ in the neighborhood of the edge on fixed point is decoupled from the three other linearized equations and the direction is stable, $\lambda_s = -0.5854$. The three other linearized equations are coupled and the eigenvalue equation has one positive real root, $\lambda_u = 0.3813$, and a pair of complex conjugate roots with negative real part, $\lambda_{\pm} = -0.9861 \pm i 2.5949$. The dynamics in the three-dimensional space spanned by $v_{y'}$, θ , and ω therefore resembles Silnikov’s phenomenon [15]. In general the existence of a Silnikov bifurcation opens the possibility for chaos, but in the present case the solutions in the vicinity of the bifurcation point are not chaotic. However, the solutions close to the bifurcation are sensitive to noise, and the numerical integration must be carried out with high accuracy in the transition region.

The period of oscillation, T , diverges logarithmically at the bifurcation point

$$T = T_0 + \frac{2}{\lambda_u} \log \frac{1}{|I^* - I_C^*|}. \quad (6.25)$$

The logarithmic prefactor is inversely proportional to λ_u evaluated at the bifurcation point, and the logarithmic divergence of T is a characteristic signature of homoclinic and heteroclinic bifurcations [14]. The factor of 2 in equation (6.25) ap-

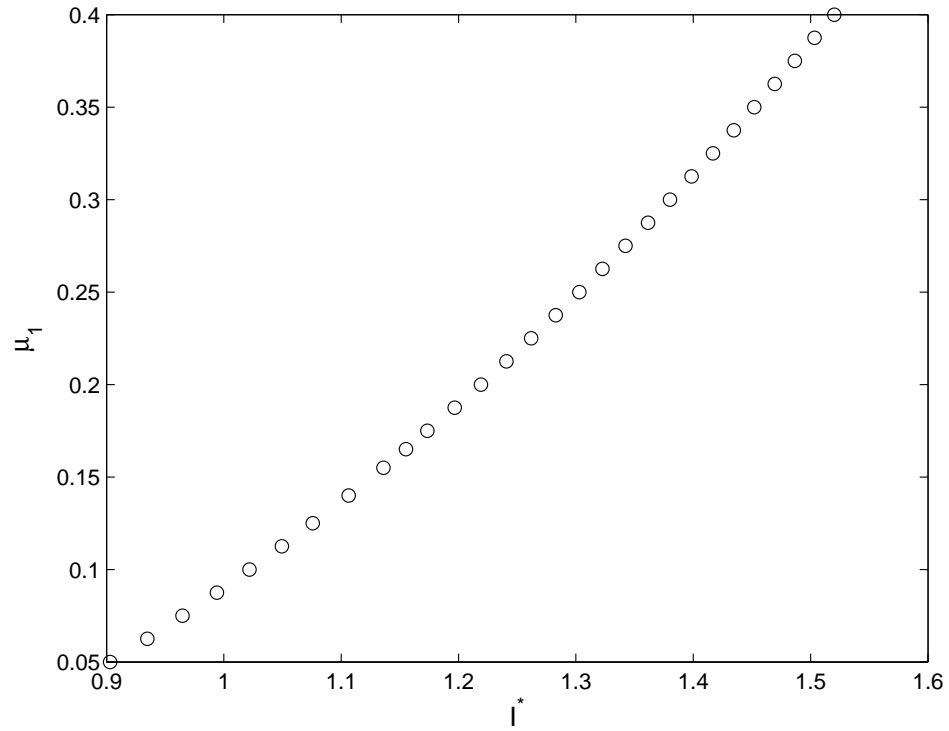


Figure 6.7: Transition between fluttering and tumbling. The card flutters in the region of the phase space on the left of the line and tumbles in the region on the right.

pears because the saddle fixed point is encountered twice during each full period of oscillation as shown in figure 6.8(b). Figure 6.8(d) shows a semi-logarithmic plot of $|I^* - I_C^*|$ versus T obtained numerically with $I^* < I_C^*$ (circles) and $I^* > I_C^*$ (stars). The numerical results are in perfect agreement with the theoretical prediction (solid line) with the eigenvalue $\lambda_u = 0.3813$ and the fit parameter $T_0 = 4.3629$.

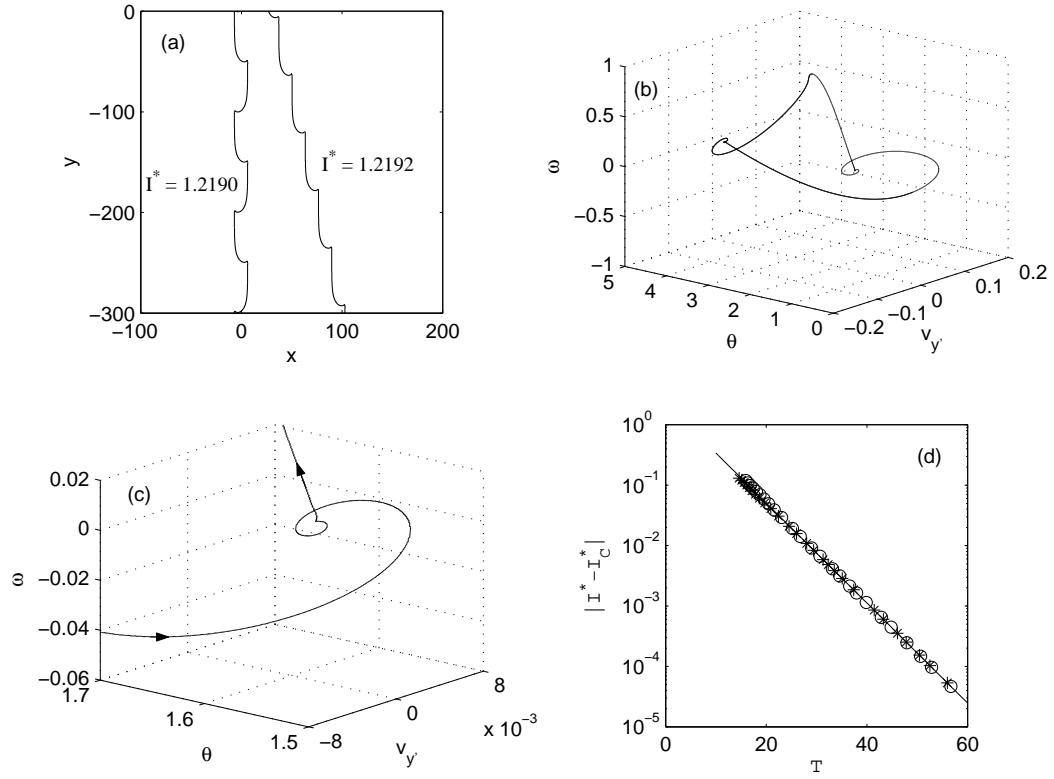


Figure 6.8: The transition between fluttering and tumbling. (a) Numerical solutions of equations (6.10) – (6.12) below and above the bifurcation point $I_C^* \approx 1.2191$, (b) and (c) the phase space trajectory for $I^* = 1.2190$ projected onto the space spanned by $v_{y'}$, θ , and ω (with $\omega \equiv \dot{\theta}$), and (d) the logarithmic divergence of the period of oscillation, T , in the neighborhood of I_C^* .

Chapter 7

Conclusions

We have presented an experimental and numerical study of the unsteady aerodynamics of freely falling plates in a quasi two-dimensional flow. We have shown that the fluid forces for both fluttering and tumbling plates are markedly different from the fluid forces on a simple gliding airfoil with constant angle of attack. In particular, the lift is dominated by the rotational velocity of the plate, so that a quasi-steady model with only translational lift is unable to explain the observed plate trajectories. With the exception of the neighborhoods of the cusp-like turning points, the fluid forces are described well by our revised quasi-steady model and dominated by rotational lift. The rotational lift provides the main mechanism of coupling between plate translation and rotation, and added mass effects play a negligible role in the plate dynamics.

The total fluid force on a freely falling plate acts close to the center of mass at about $1/100$ of the width from the center and results in a torque which is one to two orders of magnitude smaller than the torque on a plate translating at the same speed. The quasi-steady model correctly predicts the magnitude of the torque in direct numerical simulations of plates translating steadily with constant and low angle of attack, where the pressure force acts approximately halfway between the leading edge and the plate center. In contrast the fluid torque on a freely falling plate does not build up to a similarly large value, since the plate is free to rotate, and the fluid torque therefore depends sensitively on the precise locations of vortices and low pressure regions relative to the plate. For these reasons it is more difficult to apply the quasi-steady approximation to model the fluid torque

than to model the fluid forces on freely falling plates.

By varying the three non-dimensional parameters, i.e., the thickness to width ratio, the dimensionless moment of inertia, and the Reynolds number, we observed periodic fluttering, periodic tumbling, and apparently chaotic motion. Experimentally we found a transition from fluttering to tumbling with increasing thickness to width ratio, and we observed apparently chaotic motion and sensitivity to initial conditions in the transition region. We investigated the transition region numerically by changing the thickness to width ratio and thereby the non-dimensional moment of inertia. In the wide transition region we have observed periodic solutions in which the plates flutter periodically but tumble once between consecutive turning points, and we have found that the period of oscillation diverges.

To further investigate the transition between fluttering and tumbling we have analyzed a phenomenological model with both translational and rotational lift for a rigid card falling in air, and we have shown that the model depends on the thickness to width ratio, the non-dimensional moment of inertia, and the Reynolds number. We have shown that the transition between stable broadside on descent and oscillatory motion is a supercritical Hopf bifurcation. By investigating the numerical solutions of the phenomenological model we have shown that the transition between fluttering and tumbling in the model is a heteroclinic bifurcation which leads to a logarithmic divergence of the period of oscillation with a prefactor that is inversely proportional to the eigenvalue of the unstable mode at the edge on saddle fixed points.

The bifurcation scenario of the phenomenological model agrees with important features of the transition between fluttering and tumbling observed in the direct numerical simulations, including the long vertical gliding segments and the diver-

gence of the period of oscillation. However, the phenomenological model predicts a sharp transition between fluttering and tumbling, whereas the direct numerical simulations show a wide transition region with solutions that are mixtures of fluttering and tumbling. Such solutions are also found in the phenomenological model, but at larger values of the reduced moment of inertia, and they are apparently not related to the transition between fluttering and tumbling. The direct numerical simulations show that the transition between fluttering and tumbling does not have to take place through a sequence of chaotic solutions, but they do not exclude the possibility of chaos at the transition, e.g., at higher Reynolds numbers. We hope that the present work will encourage further studies of the bifurcation structure of the Navier-Stokes equation for the flow around a falling card.

Far from the transition value, the plates flutter or tumble after short transients and display periodic motion with alternating gliding at low angle of attack and fast rotation and center of mass elevation at the turning points. The periodic dynamics observed experimentally was independent of initial conditions. However, with special choices of the non-dimensional parameters we found numerically that the final periodic solution depends on the initial conditions. It will be interesting to study the dependence on initial conditions further and to clarify under what conditions periodic solutions of freely falling plates depend on initial conditions and whether or not chaotic dynamics is possible.

Understanding free-falling bodies might also have interesting applications to insect flight, an area of research that partly motivated this study. Although insects might take advantage of both active and passive mechanisms to control their flapping wings, only prescribed motions have been considered so far [29, 38]. Falling

paper is a beautiful example of a passive flight. We hope that the model presented here will be also relevant to descriptions of forces in general flapping motion.

BIBLIOGRAPHY

- [1] ANDERSEN, A., PESAVENTO, U. & WANG, Z. J. 2005 Unsteady aerodynamics of fluttering and tumbling plates. *Submitted to J. Fluid Mech.*
- [2] ANDERSEN, A., PESAVENTO, U. & WANG, Z. J. 2005 Analysis of transitions between fluttering, tumbling and steady descent of falling cards. *Accepted for publication in J. Fluid Mech.*
- [3] ANDRONOV, A. A., VITT, A. A. & KHAIKIN S. E. 1966 *Theory of Oscillators* Dover Publications, New York.
- [4] AREF, H. & JONES, S. W. 1993 Chaotic motion of a solid through ideal fluid. *Phys. Fluids A* **5**, 3026–3028.
- [5] AUGSPURGER, C. K. 1986 Morphology and Dispersal Potential of Wind-Dispersed Diaspores of Neotropical Trees. *Amer. J. Bot.* **73**, 353–363.
- [6] BATCHELOR G. K. 1967 *An Introduction to Fluid Dynamics* Cambridge University Press, Cambridge.
- [7] BELMONTE, A., EISENBERG, H. & MOSES, E. 1998 From Flutter to Tumble: Inertial Drag and Froude Similarity in Falling Paper. *Phys. Rev. Lett.* **81**, 345–348.
- [8] DICKINSON, M. H. 1996 Unsteady Mechanisms of Force Generation in Aquatic and Aerial Locomotion. *Amer. Zool.* **36**, 537–554.
- [9] DICKINSON, M. H., LEHMANN, F.-O. & SANE, S. P. 1999 Wing Rotation and the Aerodynamic Basis of Insect Flight. *Science* **284**, 1954–1960.
- [10] DUPLEICH, P. 1941 Rotation in Free Fall of Rectangular Wings of Elongated Shape. *NACA Technical Memo* **1201**, 1–99.
- [11] E, W. & LIU, J.-G. 1996 Essentially Compact Schemes for Unsteady Viscous Incompressible Flows. *J. Comp. Phys.* **126**, 122–138.
- [12] ELLINGTON, C. P. 1984 The aerodynamics of hovering insect flight. I – VI. *Phil. Trans. R. Soc. Lond. B* **305**, 1–181
- [13] FIELD, S. B., KLAUS, M., MOORE, M. G. & NORI, F. 1997 Chaotic dynamics of falling disks. *Nature* **388**, 252–254.
- [14] GASPARD, P. 1990 Measurement of the Instability Rate of a Far-from-Equilibrium Steady State at an Infinite Period Bifurcation. *J. Phys. Chem.* **94**, 1–3.
- [15] GUCKENHEIMER, J. & HOLMES, P. 1983 *Nonlinear Oscillations, Dynamical Systems, and Bifurcations of Vector Fields*. Springer-Verlag, New York.

- [16] KOZLOV, V. V. 1989 Heavy Rigid Body Falling in an Ideal Fluid. *Mech. Solids* **24**, 9–17 (1989).
- [17] JONES, M. A. & SHELLEY, M. J. 2005 Falling cards. *Submitted to J. Fluid Mech.*
- [18] LAMB, H. 1945 *Hydrodynamics*. Dover Publications, New York.
- [19] LUGT, H. J. 1983 Autorotation. *Annu. Rev. Fluid Mech.* **15**, 123–147.
- [20] LUGT, H. J. & HAUSSLING, H. J. 1974 Laminar flow past an abruptly accelerated elliptic cylinder at 45° incidence. *J. Fluid Mech.* **65**, 711–734.
- [21] MAGNAUDET, J. & EAMES, I. 2000 The Motion of High-Reynolds-Number Bubbles in Inhomogeneous Flows. *Annu. Rev. Fluid Mech.* **32**, 659–708.
- [22] MAHADEVAN, L. 1996 Tumbling of a falling card. *C. R. Acad. Sci. Paris t.* **323**, 729–736.
- [23] MAHADEVAN, L., RYU, W. S. & SAMUEL, A. D. T. 1999 Tumbling cards. *Phys. Fluids* **11**, 1–3.
- [24] MAXWELL, J. C. 1854 On a particular case of the descent of a heavy body in a resisting medium. *Cambridge and Dublin Math. J.* **9**, 145–148.
- [25] MCCUTCHEN, C. W. 1977 The Spinning Rotation of Ash and Tulip Tree Samaras. *Science* **197**, 691–692.
- [26] MUNK, M. M. 1925 Note on the Air Forces on a Wing Caused by Pitching. *NACA Technical Notes* **217**, 1–6.
- [27] PESAVENTO, U. & WANG, Z. J. 2004 Falling Paper: Navier-Stokes Solutions, Model of Fluid Forces, and Center of Mass Elevation. *Phys. Rev. Lett.* **93**, 144501.
- [28] PULLIN, D. I. & WANG, Z. J. 2004 Unsteady forces on an accelerating plate and application to hovering insect flight. *J. Fluid Mech.* **509**, 1–21.
- [29] SANE, S. P. 2003 The aerodynamics of insect flight. *J. Exp. Biol.* **206**, 4191–4208.
- [30] SEDOV, L. I. 1965 *Two-Dimensional Problems in Hydrodynamics and Aerodynamics*. Interscience Publishers, New York.
- [31] SKEWS, B. W. 1990 Autorotation of rectangular plates. *J. Fluid Mech.* **217**, 33–40.
- [32] SKEWS, B. W. 1991 Autorotation of many-sided bodies in an airstream. *Nature* **352**, 512–513.

- [33] SMITH, E. H. 1971 Autorotating wings: an experimental investigation. *J. Fluid Mech.* **50**, 513–534.
- [34] TANABE, Y. & KANEKO, K. 1994 Behavior of a Falling Paper. *Phys. Rev. Lett.* **73**, 1372–1375.
- [35] TREFETHEN, L. N. 1986 *Numerical Conformal Mapping*. North-Holland, Amsterdam.
- [36] WAGNER, H. 1925 Über die Entstehung des dynamischen Auftriebes von Tragflügeln. *Z. Angew. Math. Mech.* **5**, 17–35.
- [37] WANG, Z. J. 2000 Vortex shedding and frequency selection in flapping flight. *J. Fluid Mech.* **410**, 323–341.
- [38] WANG, Z. J. 2005 Dissecting Insect Flight. *Annu. Rev. Fluid Mech.* **37**, 183–210.
- [39] WANG, Z. J., BIRCH, J. M. & DICKINSON, M. H. 2004 Unsteady forces and flows in low Reynolds number hovering flight: two-dimensional computations *vs* robotic wing experiments. *J. Exp. Biol.* **207**, 449–460.
- [40] WEIS-FOGH, T. & JENSEN, M. 1956 Biology and Physics of Locust Flight I. Basic Principles in Insect Flight. A Critical Review. *Phil. Trans. R. Soc. Lond. B* **239**, 415–458.
- [41] WILLMARTH, W. W., HAWK, N. E. & HARVEY, R. L. 1964 Steady and Unsteady Motions and Wakes of Freely Falling Disks. *Phys. Fluids* **7**, 197–208.